SAPIENZA

University of Rome

Department of Biology and Biotechnology “Charles Darwin”

Reverse Engineering of Natural Systems by Graph Theory

Daniele Capocefalo

XXXI cycle

PhD PROGRAMME IN LIFE SCIENCES

Supervisor
Marco Tripodi

Tutor
Tommaso Mazza

Coordinator
Marco Tripodi

Director of PhD program:

Prof. Marco Tripodi

Department of Cellular Biotechnology and Hematology,

“Sapienza” University, Rome

Scientific Supervisors:

Prof. Marco Tripodi

Department of Cellular Biotechnology and Hematology,

“Sapienza” University, Rome

Scientific Tutor:

Dr. Tommaso Mazza

Bioinformatics Unit,

IRCCS Casa Sollievo della Sofferenza, San Giovanni Rotondo

To Eva and Amelia. Always Forward.

To Mauro, Tommaso, and the BFX lab. For their unwavering patience.

Table of Contents

Summary

With the advent of *high-throughput* technology, Biological research widened its horizons in terms of biomarkers and mechanisms of action of several diseases and phenotypes. On the other hand, complex diseases, like diabetes, several neurodegenerative pathologies and cancer, are still orphan of a cause and then of a cure. One of the possible reasons is that these are not strictly monogenic diseases since they result from a global interplay between molecular *players* and *master regulators*. In this context, where "the whole is something over and above its parts and not just the sum of them all" (Aristotle 384-322 B.C.), is clear that the Cartesian *reductionism* cannot completely help understand how a disease arises and develops.

Systems Biology comes on the stage here and puts emphasis on whole behavior as being basically indivisible. It sustains the Smuts's *holistic theory* according to which whole systems such as cells, tissues, organisms, and populations were proposed to have unique *emergent properties* and that it was impossible to reassemble the behavior of the whole from the properties of the individual components. Hence, new technologies were necessary to define and understand the behavior of systems.

New mathematical models and computational approaches emerged in the past decades. Thereby taking inspiration from the theory of *graphs*. Aspects of nature that could be explained by the interaction of individual agents were modeled as networks and their properties studied topologically. Speculations on the global structure of biological systems were based on two important assertions: systems have a hierarchical structure,

and the structure is held together by numerous linkages to construct very complex networks.

In this work, we retrace this path by first reconstructing and studying a complex molecular system made by gene and microRNA expression profiles in patients affected by colorectal cancer. We show how the study of topological properties of the system helped identifying a tiny subnetwork of *master-regulator* and *effectors* that, individually, were associated to poor survival rates when extremely expressed. Group-effects were not captured, until the development of Pyntacle, a cross-platform and open source Python suite of high-performance computing algorithms for the discovery of key-players in networks. Pyntacle is introduced and presented in this work and then used proficiently in two other case studies. The former regards ecological food webs and reports on the assessment of their *nestedness* property, which is an indicator of their global robustness and redundancy. The latter is an exploration of the relationships between sex and ageing process in *Drosophila melanogaster*, which developed into two computational steps: definition of co-expressing modules of genes and identification of sex independent key-players molecules in male and female flies.

Introduction

1. Systems Biology

The 19th century focused on two important concepts that originate already in the 17th century. The former is based on the Cartesian notion of *complexity* according to which a system can be reduced to pieces that can be more easily managed individually and, then, reassembled to deduce the whole behavior. The theory of Reductionism was strongly influenced by the Newton's success in mathematically describing planetary movements and characterizing gravity, and resisted till the present days, where, for example, plant biology grounds on the simple assumption that higher levels in a biological hierarchy can easily be understood from the behavior of the lower levels.

Reaction against this reductionist attitude began among a few biologists (Von Bertalanffy, 1950; Smuts and Holst, 1926) in the early part of the 20th century. They spoke a new language of life in which *complexity*, *organization*, *orchestration*, *holism*, *interconnectedness*, and *evolution* became more dominant terms. Their objections to reductionism were twofold. First, it was apparent from simple investigations on the brain and animal development that the structure of an entire system actually constrained the behavior of the component parts. Reductionist mechanistic investigations would miss the vital element of *orchestration*. Second, many scientists were still bound to the much older Aristotelian view of the natural phenomena, according to which "the whole is something over and above its parts and not just the sum of them all" (Aristotle 384-322 B.C.). This theory dominated science up to the 17th century. It was then abandoned with the development of experimental physics and later biology, before coming up again with Jan

Smuts (1870–1950), naturalist, philosopher and twice Prime Minister of South Africa. He coined the commonly used term *holism*. Whole systems such as cells, tissues, organisms, and populations were proposed to have unique emergent properties (Trewavas, 2006) and it was impossible to reassemble the behavior of the whole from the properties of the individual components. New technologies were hence required to define and understand the biological systems.

The technological response did not take long to arrive. The new microarray chips and *high-throughput* sequencing platforms were used to massively profile the Human Genome in the early 2000s (Venter et al., 2001), and hundreds of thousands of other genomes in the coming years by means of increasingly more efficient Next-Generation Sequencing (NGS) platforms. These new laboratory techniques allowed to dissect and study the individual "components" of cells, tissues, and organisms with high resolution and specificity, thereby opening new scientific horizons on all the *omics layers* (Levy and Myers, 2016).

The term 'omics' refers to any technique that enables the massive analysis of entire catalogues of molecular reservoirs, such as, for example, the whole genome sequencing (*genomics*), the overall expression levels of the mRNA species (*transcriptomics*), or the quantification of the abundance of mature protein products within a cell (*proteomics*). Probably the most famous example of use of NGS techniques on multi-omics layers is *The Cancer Genome Atlas* (TCGA) (Tomczak et al., 2015). This project, started in 2006 as a joint initiative by the National Cancer Institute (NCI) and the National Human Genome Research Institute (NHGRI) and was the first global attempt to characterize and unravel the genomic and molecular landscapes of a few cancers. It later expanded on

many other cancer types and included several other institutions that, together, collaborated to produce genomic data for more than 11,000 patients across 33 tumor types. For each tumor type, information on single nucleotide variations (SNV), copy number variations (CNV), gene and microRNA expression profiles, and methylation profiles were made available together with clinical, treatment and follow-up information for most subjects.

While the TCGA is a clear example of Reductionism, the consequent Pan-Cancer Atlas, which issued from the TCGA, is a notable example of *holism*. The Pan-Cancer Atlas provides, in fact, a uniquely comprehensive, in-depth, and interconnected understanding of how, where, and why tumors arise in humans (Hoadley et al., 2018). This is a contingent example of how reductionism and holism can be reconciled, although being often posed in opposition to each other. There is a need to understand how organisms are put together (reductionism) just as in turn there is a need to understand why they are put together in the way that they are (systems; holism). Systems Biology is an attempt to explain this embedded complexity.

Although Systems Biology did not stem from Molecular Biology, but originated from the convergence of thermodynamics and chemical kinetics (Westerhoff and Palsson, 2004), it is widely recognized that the *omics* revolution widely contributed to its spreading and popularity. Being Systems Biology an interdisciplinary field that has its roots in the theorization of a mathematical model behind observational data to infer the properties of the system, its knowledge base can be applied to a plethora of disciplines, from Ecology (Purdy et al., 2010) to drug design (Cho et al., 2006). Its widespread use and the variety of its forms make difficult, even for researchers in the field, to give a unanimous

definition of Systems Biology. However, besides all point of views, being them methodological (Breitling, 2010), technical (Kitano, 2002; Potters, 2010) or philosophical (Boogerd et al., 2007), all agree on the fundamental concept that Systems Biology is not a mere collection of biological entities and their measurements, but of the relationships among them, that, if known, can be used to build a computational model of the system of interest. Such structure is generally named *network*.

A network, often referred to as *graph*, is a mathematical system made by *nodes*, the entities that populates the system, and *edges*, the interactions that occur between nodes. The level of abstraction used with real world systems makes networks the model of choice in a variety of fields other than Biology, from Information Theory to Social Sciences. For example, a network might be made by all the web pages of the World Wide Web (WWW), the nodes being pages and the edges being hyperlinks among them. A kind of network like this is used by the Google search engine to traverse all web pages of the WWW and to rank and identify the ones that are important in terms of the number of hyperlinks that points to them (Page et al., 1998). Recently, studies on the dynamics of social networks became popular because they attempted to explain complex social events and to capture the spreading of information across communities of people united by common beliefs. These communities, known as *tribes* or *echo chambers* (Del Vicario et al., 2016) spread news about their topics of interest much faster than people who do not belong to them can do, and often reinforce their convictions, turning people with moderate beliefs into one with more extreme views on the subject, a phenomenon often called *polarization* (Del Vicario et al., 2017).

Nowadays, networks are used ubiquitously in Systems Biology. They mainly differ for assortment and completeness of information. In fact, most biological networks focus on and depict only a portion of a natural phenomenon. This is the main reason why several kinds of biological networks exist: protein–protein interaction (PPI) networks, gene regulatory networks (DNA–protein interaction networks), signaling networks, gene co-expression networks (transcript–transcript association networks), metabolic networks, neuronal networks, food webs, between-species interaction networks and within-species interaction networks. The p53 transcription factor of *Homo sapiens* is an example of PPI network (Figure 1A) that particularly focuses only on the proteins that physically interact with the human p53 transcription factor. All these kinds of networks may also be composed by heterogeneous nodes, namely by nodes representing different kinds of molecules (e.g., enzymes, genes, miRNAs). Signaling networks, also known as *pathways*, are notoriously heterogeneous networks, since they represent not only the different types of interactions among protein products, but the whole cellular signaling cascades and their actors, which enable them to function. The p53 pathway (available from the KEGG database (Kanehisa and Goto, 2000), Figure 1B) adds to its PPI interaction network available from the STRING web service (Szklarczyk et al., 2015) information on the nature of the interactions among protein products, feedbacks loops of activation and inhibition, types of molecules represented by nodes (i.e., genes, enzymes, substrates) and on the processes that are activated downstream.

Irrespective of the inner semantics of networks, Systems Biology developed a big area of research aimed at characterizing the architectural structure of networks, irrespective of whether they were molecular or social. Several evidences support indeed the existence of a global hierarchy and, then, that the network organization is not the fruit of chance, but

of the emergent need to protect important properties of networks, like the *robustness*, which hold when the *topology* of their nodes and edges is preserved. A system is robust when it resists to any kind of interference in the structures of nodes and edges, thus still retaining most of its key functions (Csete and Doyle, 2002). The bacterial chemotaxis process is a notable example. *E. coli* has been proven to exhibit strong variations in enzymes concentration and time to adapt in response to chemotaxis stimuli (Alon et al., 1999), still responding precisely to exogenous stimuli. This area of research is named *Network Biology*.

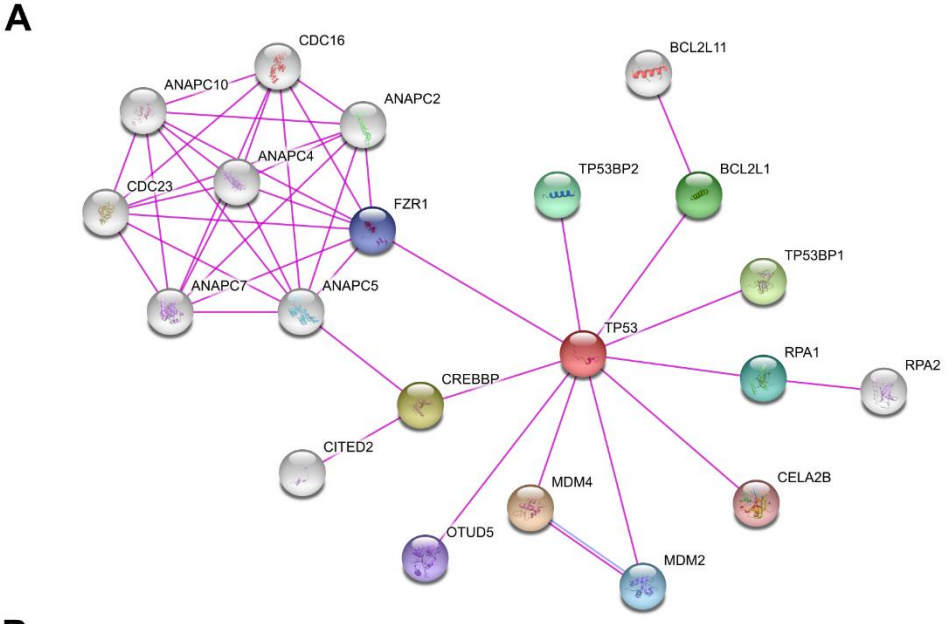
A
CDC16
ANAPC10
ANAPC2
ANAPC4
CDC23
FZR1
ANAPC7
ANAPC5
BCL2L11
TP53BP2
BCL2L1
TP53BP1
TP53
RPA1
RPA2
CREBBP
CITED2
MDM4
CELA2B
OTUD5
MDM2

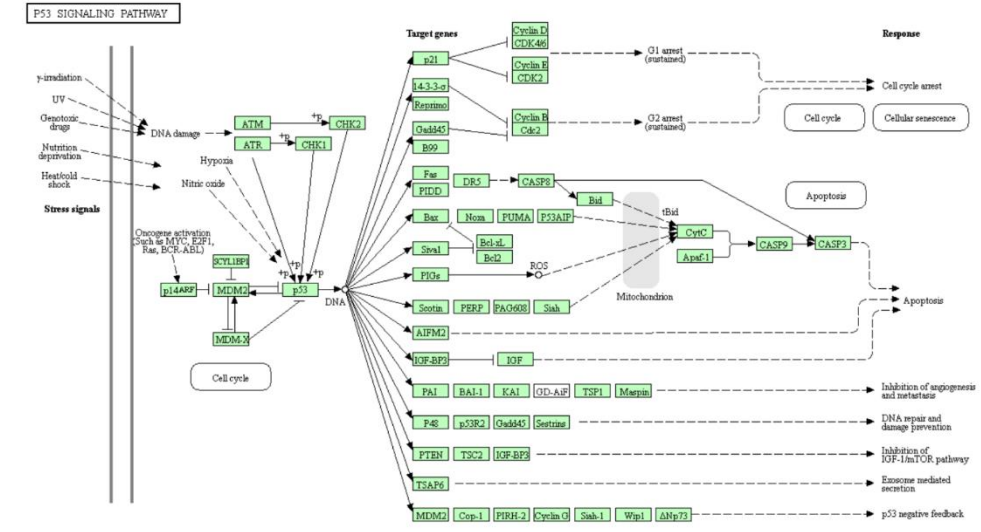
B
P53 SIGNALING PATHWAY
Stress signals
γ-irradiation
UV
Genotoxic drugs
Nutrition deprivation
Heat/cold shock
DNA damage
ATM
ATR
CHK2
CHK1
Hypoxia
Nitric oxide
Oncogene activation (Such as MYC, E2F1, Ras, BCR-ABL)
SCYL1BP1
p14ARF
MDM2
p53
MDM-X
DNA
Cell cycle
Target genes
p21
14-3-3-σ
Reprimo
Gadd45
B99
Fas
PIDD
DR5
CASP8
Bid
Bax
Noxa
PUMA
P53AIP
Bcl-xL
Bcl2
Survi
PIGs
Scotin
PERP
PAG608
Siah
AIFM2
IGF-BP3
IGF
PAI
BAI-1
KAI
GD-AIF
TSP1
Maspin
P48
p53R2
Gadd45
Sestrins
PTEN
TSC2
IGF-BP3
TSAP6
MDM2
Cop-1
PIRH-2
Cyclin G
Siah-1
Wip1
ΔNp73
Cyclin D
CDK4/6
Cyclin E
CDK2
Cyclin B
Cdc2
G1 arrest (sustained)
G2 arrest (sustained)
Response
Cell cycle arrest
Cell cycle
Cellular senescence
Apoptosis
tBid
CytC
Apaf-1
CASP9
CASP3
ROS
Mitochondrion
Apoptosis
Inhibition of angiogenesis and metastasis
DNA repair and damage prevention
Inhibition of IGF-1/mTOR pathway
Exosome mediated secretion
p53 negative feedback

Figure 1: A) the interaction network of the TP53 human transcription factor and its closest neighbors as reported by the latest version of the STRING database (accessed Sept. 2018). B) the pathway of TP53 as reported by KEGG is itself a direct network in which coding genes, protein product and transcription factors are linked not only on the base of interactions, but by activation, inhibition, phosphorylation and other stimuli. A pathway is indeed a network, and each link may correspond to a class of edges that compose it.

2. Network Biology

Understanding the topology of networks is the main purpose of Network Biology. Mathematically speaking, networks are actually *graphs*, which collect points and lines connecting some (possibly all) nodes. The points of a graph are most commonly known as graph vertices, but they may also be called "nodes" or "points". Similarly, the lines are most commonly known as edges, even if they may also be called "arcs" or "lines". The vertices belonging to an edge are called the ends or end vertices of the edge. The edges may either connect one vertex to another or a vertex to itself. In the second case, they form self-loops. It is then possible that a vertex is not connected with any other vertex. In this case it is called *isolated* node.

Different kinds of graphs exist. When the orientation of the edges matters, the graph is called *directed*. In the opposite case, it is called *undirected.* One important class of graphs consists of those that do not have self-loops or parallel edges. Such graphs are called *simple*. In a simple graph, no two edges share the same ends, then the specification of two ends is sufficient to identify an edge. A simple graph G can be defined as the ensemble of (V, E), where V is a set of vertices and E is a set of edges. Hence, $E = \{(i, j)$

$| i, j \in V\}$ and (i, j) is equals to (j, i) in undirected graphs. If two vertices are adjacent to each other, namely they are linked by one edge, they are called *neighbors*. When instead multiple edges join the same pair of nodes, the graph is said *multigraph*. In such case, each connection indicates a different type of information. This is an important feature since there are networks such as PPI networks in which two proteins might be evolutionary related, co-occur in the literature or co-express in some experiments, resulting by this way in three different connections, each one with a different meaning and representing a different layer of information. If a graph contains multiple edges and self-loops it is called *pseudograph*.

Molecular pathways are notable examples of directed graphs (Figure 1B) since their edges describe the subjects and the objects of the interactions. Undirected graphs were extensively used to represent many other natural systems, from ecological, to population dynamics and molecular systems. In particular, PPI networks are actually undirected graphs (or multigraphs), since edges often represent a kind of relationship of which both the connected nodes are equally subjects and objects. Irrespective of the direction of edges, a graph can be *weighted* or *unweighted*, depending on the availability of numerical attributes of edges (Figure 2).

A graph may be comprised of several connected components and isolates. In this case, the graph is a *supergraph* made by two or more *subgraphs*. The bigger subgraph is the *largest connected component*.

As the only relevant factor that shapes a Graph is represented by the links among nodes, the aesthetics of the graph does not matter as long as the links are not rewired. For example, it does not matter whether the edges drawn are straight or curved. Edges

(sometimes referred to as links) can connect nodes in any way possible or curved, or whether one node is to the left or right of another.

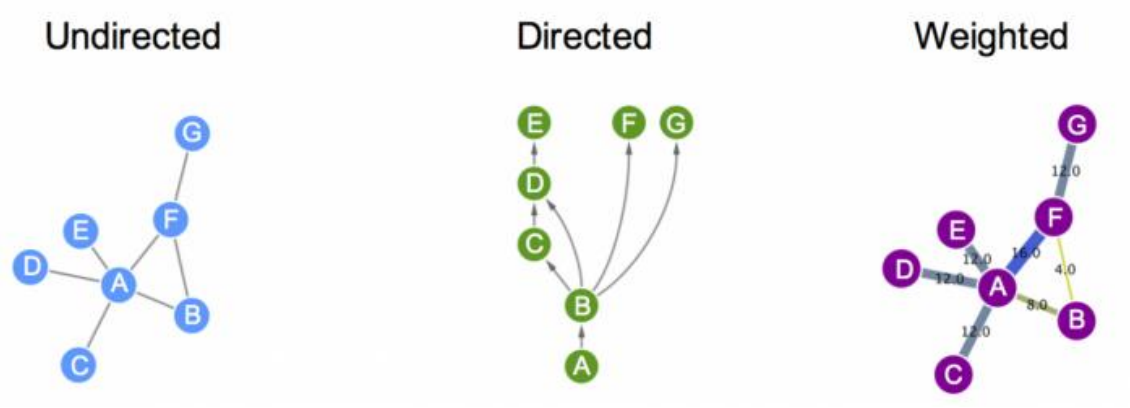

Figure 2: Different types of graphs. (Left) undirected graphs, where no orientation of edges is specified; (center) directed graphs, where edges have directions; (right) weighted graphs, where links are accompanied by numerical values indicating a sort of strength factor.

3. Network inference methods

Several methods exist to build biological networks. These are mainly divided into two classes according to whether they take information from literature or public databases (*literature-based* methods) or straight from experimental data (*experimental-based* methods).

The former class makes use of highly curated sources of molecular interactions, like for example STRING and BioGRID. STRING is a database of known and predicted protein-protein interactions that contains 9.643.763 proteins from 2.031 organisms (Szklarczyk et al., 2015). The interactions include direct (physical) and indirect (functional) associations; they stem from computational prediction, from knowledge transfer between organisms, and from interactions aggregated from other (primary) databases. Interactions are derived from five main sources: genomic context predictions; high-throughput lab experiments, (conserved) co-expression, automated text-mining and previous knowledge in databases. Similarly, the Biological General Repository for Interaction Datasets (BioGRID) is a public database that archives genetic and protein interaction data from model organisms and humans (Chatr-aryamontri et al., 2017). It currently holds over 1,400,000 interactions curated from both high-throughput datasets and individual focused studies, as derived from over 57,000 publications in the primary literature. Current curation drives are focused on particular areas of biology to enable insights into conserved networks and pathways that are relevant to human health. A known tool using these and other similar databases is, for example, GeneMANIA (Mostafavi et al., 2008). It finds other genes that are related to a set of input genes, using a very large set of functional association data. Association data include protein and genetic interactions,

pathways, co-expression, co-localization and protein domain similarity. The resulting network will be a multigraph made by as many nodes as the input genes plus the number of found interacting genes, and as many edges as the total number of literature hits. We still miss, however, detailed database that store interaction among non-coding genes, or non-coding-coding relationships, such as the relationships among small non-coding RNAs, such as miRNA and their target genes. In this regulatory network, links are drawn if a miRNA has a direct effect on a gene ectopic expression. Although these networks proved useful in the characterization of the regulatory network of several diseases (Jiang et al., 2012; Yang et al., 2017; Ye et al., 2018), and some tools were developed to use network analysis techniques to provide insights on the role of non-coding-RNAs and their coding counterparts (da Silveira et al., 2018), there is plenty of room for improvement.

The latter class is made by slightly more complex methods that infer interactions from experimental data. Gene expression data are used to deduce gene *co-expression.* Co-expressing genes are linked by edges in a network which, in turn, are eventually weighted by the statistics used to assess the co-expression. Researchers trained in statistics often measure gene co-expression by the correlation coefficient. Computer scientists, trained in information theory, tend to use a mutual information (MI) based measure. Thus far, the majority of published articles use the correlation coefficient as co-expression measure (Zhang and Horvath, 2005; Zhou et al., 2002), but hundreds of articles have used the mutual information (MI) measure with notable results, showing that the contribution of

these two means to assess gene-to-gene relationships are equivalent (Daub et al., 2004; Priness et al., 2007; Song et al., 2012). Several articles have used simulations and real data to compare the two co-expression measures when clustering gene expression data. Allen et al. have found that correlation based network inference method WGCNA (Langfelder and Horvath, 2008) and mutual information based method ARACNE (Margolin et al., 2006) both perform well in constructing global network structure (Allen et al., 2012). Steuer et al. show that mutual information and the Pearson correlation have an almost one-to-one correspondence when measuring gene pairwise relationships within their investigated data set, justifying the application of Pearson correlation as a measure of similarity for gene-expression measurements (Steuer et al., 2002). In simulations, no evidence could be found that mutual information performs better than correlation for constructing co-expression networks (Lindlöf and Lubovac, 2005). However, MI continues to be used in recent publications. Some authors have argued that MI is more robust than Pearson correlation in terms of distinguishing various clustering solutions (Priness et al., 2007). On the other hand, although MI is well defined for discrete or categorical variables, it is non-trivial to estimate the mutual information between quantitative variables, and corresponding permutation tests can be computationally intensive. In contrast, the correlation coefficient and other model-based association measures are ideally suited for relating quantitative variables. At last, it must be noted that the majority of network inference methods was built using microarray as main source of expression and questions. Co-expression analysis based on RNA-Seq data is still in its primes and thus many of these techniques are forwarded from one experimental setting

to another. This may lead to incorrect results, as the two techniques are overlapping, but have different source of noise that, if not addressed carefully, may undermine the connections in a co-expression of MI network. Appropriate evaluations of the factors that may affect functional connectivity and topology in co-expression network is thus a main concern within the network biology community. For this purpose, a detailed evaluation of all the methods used in co-expression analysis was performed and revealed that the simpler the measure of distance, the highest is the reliability of co-expression network (Ballouz et al., 2015). On this regard, the size and the depth of the samples are more important than the normalizing procedures each method apply for noise reduction.

Results

Aim of the Work

The use of network models in Systems Biology is not just a nuance within the broad landscape of bioinformatics approaches, but it is the backbone, which they rely on, to uncover system-wide relationships among molecules. Network-based methods exploit solid mathematical tools to identify molecules that play critical roles in pathophysiological cellular processes, to unravel the complexity of natural systems, their structure, i,e. their topology, and to reveal the presence and the interplay of subgroups of nodes (communities). This work aims at presenting and using a broad set of graph-based algorithms and tools in several contexts, proving the usefulness of biological network analysis as a framework on which to rephrase biological questions.

First, we reviewed and used the standard methods used in the Network Biology community to describe the architecture of the colorectal cancer molecular network formed by coding and non-coding genes. We studied and assessed the role of some small non-coding RNAs, the microRNAs, on the protein-protein interaction network made by the deregulated genes in colorectal cancer and found the communities of miRNAs that, together, contributed to the carcinogenesis. Moreover, by studying the indirect and long-range relationships among molecules, we assessed the role of miR-145 as a master regulator of the population of all miRNAs. This showed that the miRNAs network is hierarchically organized.

Second, we applied the same topological indices to a set of ecological networks plus some new metrics that accounted not only for the centrality of individual molecules but also

for that of groups of nodes. Group centrality metrics were developed in other scientific contexts and were extensively used in Ecology to search and find the species that, together, are responsible for an ecosystem development and maintenance. These group centrality metrics are almost unknown in the Network Ecology community. In fact, the existing software tools in this area of research still lack the ability to determine the *team-play* effects in networks.

For this reason, using Python dynamic programming, we developed Pyntacle, a swiss knife tool for network analysis that exploits many of the current standard analysis methods to find key-players. Key-players are groups of nodes that appear to be determinant for the fragmentation or the reachability of the network boundaries. We compared Pyntacle to the only other existing software tool that performs group centrality analysis and found that it outperforms the competitor R package by several orders of magnitude, with a gap in performance that increases with the network sizes.

We thus tested Pyntacle with real ecological networks. In particular, we have characterized the topological structures of 27 food-webs, belonging to terrestrial ecosystems, and identified a nested structure within them. Then, we resorted to Molecular Biology and used Pyntacle to identify critical groups of molecules that, together, may contribute to the sex-specific aging phenotype in *Drosophila melanogaster*.

1. Network analysis reveals RNA-RNA crosstalk and highlights the role of microRNA-societies in human colorectal cancer

1. Background

Network analysis has particularly impacted on Biology in the understanding of the mechanisms that underlie the onset and progression of cancer whenever it dealt with *high-throughput* data. Cancer is a multifaceted disease that causes a dramatic reshaping of the cellular molecular processes. This phenomenon is specific for each cancer type and individuals, although molecular hallmarks can be largely found in the literature (Fouad and Aanei, 2017; Hanahan and Weinberg, 2000). The reason why many cancer subtypes exhibit a low survival, coupled with the difficulty of treating two tumors of the very same nature can be ascribed, at least in part, in its irregular cellular heterogeneity, which makes diverse subpopulations of tumor cells in every individual with distinct characters (*molecular signatures*). The obvious consequence is that it is quite complicated to trace-back the time and the causative event (the point of origin or the cellular Big Bang (Sottoriva et al., 2015)) which the tumor originated from. What makes things worse is that cellular heterogeneity impacts significantly also in the efficacy of the response to therapies (Fisher et al., 2014), since cells may be less susceptible to some drugs than others (Dagogo-Jack and Shaw, 2017). These points have encouraged the development of a new area of research: *precision medicine* (Drew, 2016; Hodson, 2016). The underlying concept of precision medicine is that health care is individually tailored on the basis of a person's genes, lifestyle and environment. Although this concept was not new, advances in genetics, the growing availability of health data and progress in the

omics, is now presenting an opportunity to make precise personalized patient care a clinical reality.

Network Biology is a keystone of personalized medicine techniques, since it bridges all the *omics* and their data and helps to determine the so-called "master regulators" (Kin Chan, 2013). Master regulators are pivotal molecules, which are not necessarily tightly connected with other molecules, but which plays critical roles in sustaining cancer and its deadly mechanisms. Since they are supposed to be the closest molecules to the *point of origin* of a tumor, several attempts were made to discover them in different cancers.

Colorectal cancer (CRC), also known as bowel cancer and colon cancer, is the development of cancer from the colon or rectum (parts of the large intestine). CRC that are confined within the wall of the colon may be curable with surgery, while cancer that has spread widely are usually not curable, with management being directed towards improving quality of life and symptoms. According to the 2014 World Cancer Report, the five-year survival rate in the United States is around 65%. The individual likelihood of survival depends on how advanced the cancer is, whether or not all the cancer can be removed with surgery and the person's overall health. Globally, colorectal cancer is the third most common type of cancer, making up about 10% of all cases. In 2012, there were 1.4 million new cases and 694,000 deaths from the disease. It is more common in developed countries, where more than 65% of cases are found (Stewart and Wild, 2014). It is less common in women than men.

In the context of CRC, we studied the transcriptomic regulation of messenger RNA mediated by micro-RNAs (miRNAs), a class of a small non-coding RNA molecules that are involved in the post-transcriptional regulation of RNA transcripts, by base-pairing to

partially complementary sites on the target messenger RNAs (mRNAs), usually in the 3-untranslated region (3 UTR). Each miRNA has the potential to target many genes, with many miRNAs able to synergistically regulate the same mRNA transcript (Huntzinger and Izaurralde, 2011; Kim and Nam, 2006). The alterations in the population of non-coding transcripts may play important roles in cancer pathogenesis. Numerous miRNA encoding genes are frequently located at fragile genomic sites or within regions frequently deleted or amplified in neoplastic diseases (Calin et al., 2004). The accumulation of alteration in the miRNA population, with processes such as deletion, mutation or methylation of miRNA-encoding genes may cause deregulated expression of critical miRNAs, which can then act as oncomiRs or tumor suppressors (Calore et al., 2013).

In colorectal cancer, the main hallmark of carcinogenesis is the accumulation of genetic alterations in oncogenes and tumor suppressor genes, which control crucial cellular processes such as proliferation, differentiation and apoptosis in the colorectal epithelium (Markowitz and Bertagnolli, 2009). The first group of genetic alterations includes inducers of chromosomal instability, which is driven by amplifications/deletions of whole or subsections of chromosomes that can underlie both the progressive inactivation of tumor suppressor genes, such as adenomatous polyposis coli (*APC*), deleted in colorectal cancer *SMAD4* and *TP53*, and the activation of oncogenes such as *KRAS* (Cunningham et al., 2010; Tarafa et al., 2000). The second group of genetic alterations induces microsatellite instability (MSI), which is associated with mutations in genes containing simple repeats, such as those encoding the epidermal growth factor receptor (*EGFR*), the apoptotic factor BCL2-associated X protein (*BAX*) and the transforming growth factor β receptor II (*TGFBR2*). MSI results in the inactivation of genes belonging to the DNA

mismatch repair family (Jensen et al., 2009; Wright et al., 2005). These two genetic alterations rarely occur together in the same colorectal cancer specimen (Gervaz et al., 2002)and have a different impact on survival, with MSI showing an improved prognosis compared to chromosomal instability (Boland and Goel, 2010a; Saridaki et al., 2014). The third group of genetic alterations includes epigenetic alterations, which together make the so said CpG island methylator phenotype (CIMP). CIMP is characterized by epigenetic instability and by high methylation levels of the promoters of some tumor suppressor genes, such as the Cyclin-Dependent Kinase Inhibitor 2A (*CDKN2/p16*), insulin-like growth factor 2 (*IGF2*) and MLH1 (Pritchard and Grady, 2011).

All these events impact several key-signalling pathways that are commonly deregulated in carcinogenesis, including WNT-β-catenin, EGFR, mitogen-activated protein kinase(MAPK), TGF- β and phosphatidylinositol 3-kinase (*PI3K*). Alterations in the WNT-β-catenin pathway are responsible for many epithelial tumors, being involved in approximately 30–70% of human sporadic colorectal cancers (CRCs). Mutations in the APC gene, affecting the carboxy-terminal region, are implicated in β-Catenin and axin binding, leading to the deregulated nuclear translocation of the β-catenin transcription factor from the cytoplasm (Polakis, 2000). This induces the genesis of a tumor phenotype by enhancing the transcription of several oncogenes and target genes, such as *MYC* and *CCND1* (Kobayashi et al., 2000). Sporadic CRCs, negative for *APC* or *CTNNB1* gene mutations, are characterized by activation of the WNT signaling pathway via *APC* inhibition by miR-135, which, in turn, is upregulated in CRC, or by direct modulation of β-catenin by miR-200a, which alternatively interacts with the 3' UTR of *CTNNB1* or drives the down-regulation of the ZEB1/2 gene (Huang et al., 2010). EGFR is an important player in colorectal carcinogenesis, being a modulator of critical cellular

processes such as proliferation, adhesion and migration. The EGFR intracellular signal transduction pathways include components of the MAPK, PI3K, signal transducer and activator of transcription, protein kinase C and phospholipase D pathways. In particular, the MAPK pathway modulates numerous key kinases, which, in turn, control cell growth, differentiation, proliferation, apoptosis and migration through a series of intermediate proteins, including *RAF*, *MEK* and *RAS* (Dhillon et al., 2007). The latter is a critical gene since it can unleash its signalling cascade either by PI3K, thereby inhibiting apoptosis, or by *RAF*, thereby stimulating cellular proliferation. The anomalous activation of the receptor tyrosine kinases or the gain-of-function mutations occurring in the *RAS* or *RAF* genes are reported to cause the deregulation of the RAS-RAF-MEK-ERK-MAPK axis, which, in turn, is a frequent therapeutic target (Phipps et al., 2013; Roberts and Der, 2007; Santarpia et al., 2012). Interestingly, the down-regulation of miR143 was shown to contribute to *ERK/MAPK* activation, as well as to *KRAS* and *ERK5* repression (Akao et al., 2007).

The onset and progression of colorectal cancer are linked to a combination of causal perturbations occurring at any omics layer (Muzny et al., 2012) and relevant studies have brought out the anomalous interactions between gene transcripts and miRNA molecules as crucial causes of carcinogenesis (Caldas and Brenton, 2005; Hecker et al., 2013; Mezlini et al., 2013; Piepoli et al., 2012). Bearing these findings, we sought to define the mRNA–miRNA cross-talks in search of mutual and combined effects on the colorectal carcinogenesis process by means of computational and analytical methods from Systems Biology, in particular using network analysis techniques, to inspect both transcriptome layers and their interactions, and to look for socially central (groups of) molecules. We

addressed this issue by a multifaceted analysis strategy, encompassing a series of functional enrichment, topological and clustering analyses, which were conducted on genome-wide mRNA and miRNA expression profiles of matched pairs of tumor and adjacent non-tumorous mucosa samples obtained from CRC patients. *In-silico* analyses highlighted the prominent topological position of miRNA-145 and its mechanistic role in maintaining cohesiveness and functional cooperation among groups of key miRNAs and genes. Given the critical tumor suppressive role of miR145, its action, combined with several other miRs, was deemed responsible for a coordinated program of patterned gene regulation, whose master regulator was miR-145. The discovery of its partners and of the unexplored effects of their interactions in colorectal carcinogenesis was, therefore, a further objective of this work. This was achieved by first identifying *in- silico* the co-expressing partners of miR-145, and then, by perturbing them in vitro in four CRC cell lines. We verified that the ectopic expression of miR-145 impacts the whole miRNA network and that, downstream, this perturbs the MAPK signalling cascade.

2. Inferring Gene-Regulatory networks from enriched biological processes

Differential expression analysis of CRC stage IV tumor tissues at versus their matched adjacent non-tumorous tissues defined a total of 4.441 genes significantly deregulated between matched tumor and (2.549 up-regulated and 1.892 down-regulated in the CRC specimens), of which 1.645 and 878, respectively, maintained the same expression direction in at least five experiments deposited in the EBI Gene Expression ATLAS (Kapushesky et al., 2012). To confirm these findings, we verified that the CRC pathway (hsa05210 KEGG pathway, in Figure 3) was significantly impacted. Twenty-eight out of 45 genes of this pathway were deregulated in a statistically significant way ($p = 1.32e^{-10}$). These genes are known to functionally participate in four macro biological processes (BPs): *proliferation*, (anti)-*apoptosis*, *growth* and *cell cycle control*.

This list of genes was used to perform the gene enrichment functional analysis. 2091 genes, 83% of the whole gene pool was found to be significantly associated to these BPs with respect to the 9089 genes, that accounted for 52.1% of the background set of genes, known to carry out these processes ($p < 0.0001$). By confronting the log-Odds ratios, the classes of BPs were classified as *cancer-favourable* (adjusted $p = 0.016$) and *cancer-protection.* This classification was done on their positive or negative association to colorectal carcinogenesis and in general to *cancer-related* processes (adjusted $p < 0.001$). Specifically, *cancer-favourable* processes included 48 genes hampering apoptosis, 23 genes promoting cell cycle progression, 92 genes increasing proliferation and 9 genes promoting cell growth. *Cancer-protection* genes encompassed 106 apoptosis-favourable genes, 53 genes promoting cell cycle control, 95 genes hindering proliferation and 24

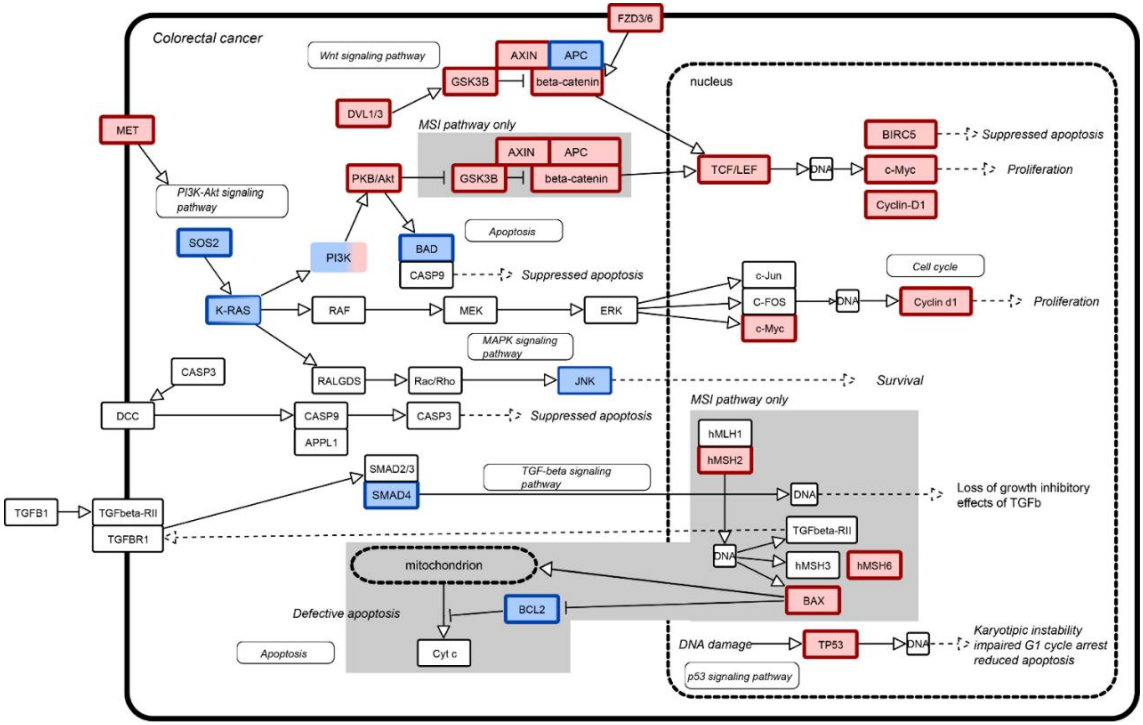

Figure 3: The landscape of the genes involved in CRC onset. Up-regulated genes (in red) and down-regulated genes (in blue) of the CRC pathway (KEGG id: hsa05210). TFC7 and LEF1 symbols are encompassed in TCF/LEF, while PI3K includes PIK3R2, PIK3CG PIK3C.

genes decreasing cell growth. The remaining genes fell in the cancer-related set of BPs, 158 of which were apoptosis-associated, 105 involved in cell cycle regulation, 199 were proliferation modulators and 42 were related to cell growth. 391 genes were selected on the bases of these findings and were submitted to the GeneMania (Mostafavi et al., 2008) Cytoscape plugin, to reconstruct the interaction map among these genes. Genes were connected among them if at least one verified experimental interaction was stored in the

GeneMania database. As GeneMania also stores information from other sources, the resulting link in the interaction network were enriched by means of relationships of co-expression (52.65% of the total number of relationships), co-localization (14.85%), physical interactions (13.52%), shared pathways (9.06%), shared predicted interactions (8.44%), shared genetic interactions (1.23%) and shared protein domains (0.26%). The network is hence a multigraph since it allows more than one edge connecting two nodes. As the information in this multigraph was redundant, and in order to process the network for further analysis, the network was reduced to a simple graph, as described in the Materials and Methods chapter, section 1.5.

The resulting network is made of one connected component with relative complexity. The global properties of this component, when measured, yielded clustering coefficient = 0.257, diameter = 4 and network density = 0.095. Network density ranges from 0 to 1, and measures how densely a network is populated with edges (so the ratio between the total number of edges in a network and the number of nodes in the network). A network with no edges and solely isolated nodes has a density equal to 0. This network was divided using the clusterONE algorithm (Nepusz et al., 2012), with default parameters. The tool performs modular decomposition searching for communities (i.e., groups of nodes) in the network, identifying 11 distinct communities in the overall interaction network (Figure 4). This procedure identified 11 modules, classified and divided into two *cancer-protection* and nine *cancer-favourable* modules, according to the BPs of the genes that populate them, and as to whether their genes are up-regulated or down-regulated. Among the most central genes, also known as intramodular hubs *TP53* (module 6), *MYC* (module 10), *CDK4* (module 2), *CTNNB1* (module 4), *CHEK1* and *CDK2* (module 1) were found to be the top six genes, in terms of centrality measures, for at least three out

of the four centrality metrics (degree, closeness, betweenness, clustering coefficient), hence confirming their central role in the network. Intramodular hubs link to several proteins that are highly self-connected and that are, therefore, more likely to perform any biological task in cooperation (Liang and Li, 2007). Such hubs are almost never pleiotropic, meaning they do not take part in other functions other than the ones reported for each one.

3. Functional modules in literature-based and experimental miRNA networks

To uncover the miRNAs regulatory network for the genes responsible for the CRC development for the transcriptional regulation of genes responsible for the CRC, the 391 genes were screened against the Human Molecular Disease Database (Li et al., 2014) and only those known to be associated to CRC were selected. The miRNAs that directly target these genes were retrieved through to the miRSystem online resource (Lu et al., 2012). The miRNA-target list is reported in Table 1. Selected miRNAs are given in input to the Ingenuity Pathway Analysis Software (IPA) to recreate a *literature-based network* for 19 of these miRNAs, altogether with the genes controlled by them (Figure 5A). Links were drawn if the physical interaction between miRNAs and genes were found to be experimentally validated or there was concrete evidence of the participation of the same *cancer-related* biological functions.

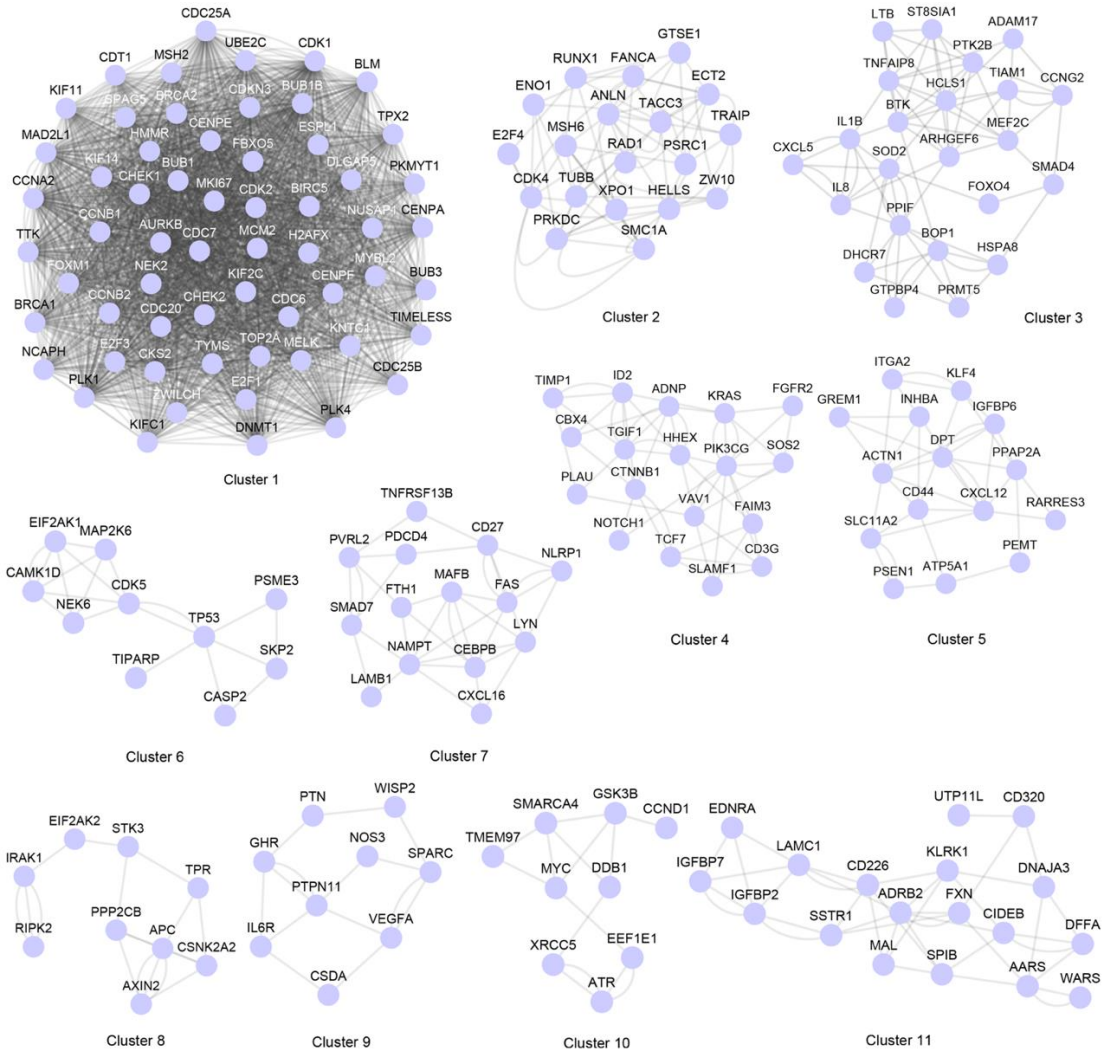

Figure 4: Modules identified by network clustering using the ClusterONE algorithm. Nodes are genes that are connected by undirect relationships (edges). An edge between a pair of genes when at least one experimental evidence of interaction is present between the genes.

Gene	Module	Expression level in CRC	Targeting miRNAs
BCL2		down	miR-17, miR-20a, miR-18a
CCNA2	**module 1**	**up**	**miR-145**
CCND1	module 10	up	miR-17, miR-195, miR-20a, miR-19a, miR-99a
CDC25A		up	miR-21
CDK6		up	miR-185, miR-195, miR-21, miR-29a
CXCL12	module 5	down	miR-23a-3p
E2F1	**module 1**	**up**	**miR-17, miR-20a, miR-21, miR-93, miR-18a**
E2F3	module 1	up	miR-195
FAS	module 7	down	miR-21
FOXO1		down	miR-183, miR-27a
HEXIM1		down	miR-17
HSPA8	**module 3**	**up**	**miR-106a, miR-17, miR-20a, miR-26b, miR-93**
IL6R	module 9	down	miR-21
IL8	module 3	up	miR-17, miR-20a
LRP5	**module 8**	**up**	**miR-23a-3p, miR-23b, miR-27a, miR-375**
KLF4	module 5	down	miR-10b

KRAS	module 4	down	miR-143, miR-18a
MYC	**module 10**	**up**	**miR-145, miR99a, miR-18a**
NOTCH1	module 4	up	miR-23b
PDCD4	module 7	down	miR-21
PPIF	module 3	up	miR-21
RM1		up	miR-106a
RUNX1	module 2	up	miR-106a, miR-17, miR-20a, miR-27a, miR-18a
SMC1A	module 2	up	let-7e
SPARC	module 9	up	miR-29a
VEGFA	module 9	up	miR-106a, miR-17, miR-20a, miR-19a, miR-18a

Table 1: MiRNAs targeting de-regulated genes n CRC tumor samples when compared to matched-normal tissues. Cells with text in bold identify the five genes with the best scores in terms of observed identification probability (*O*) and expected probability (*E*) ratios.

An *experimental network* was derived from the 41 above-mentioned miRNAs. A miRNA was selected to populate this network only if it was differentially expressed between tumor and adjacent non-tumorous tissues and significantly correlated with at least a miRNA within the network. The sign of correlation was not kept into account, as we focused only on miRNA-gene relationships rather than their regulation pattern. Thirty-nine out of 41 miRNAs resulted to be linked by 148 edges (Figure 5B). The experimental network almost included the literature-based network. MiRNAs with no links with other miRNAs were discarded. Moreover, the experimental network contained miRNAs not present in the literature-based network, such as miR-335.

The two networks were compared in search of similarity and differences. Edges were compared using the assumption that if two miRNAs are connected to the same target gene, they are connected the same way. This analysis showed that the two networks presented distinct topological features. This may imply that the literature network is incomplete and misses unknown functional relationships between miRNAs involved in CRC development.

Topological analysis based on several key centrality metrics such as degree, closeness, betweenness clustering coefficient and radiality of the experimental network indicated two significant clusters: a triangle made of miR-708, miR-18b and miR-17 and a clique made of miR-144, miR-1246, miR-1275 and miR-99a. Both modules were made of nodes not present in the literature-based network, except for miR-17. MiR-17 and miR-1246 or miR-99a were used as seeding nodes by Cluster ONE for the detection of the modules. Among these, miR-708, miR-18a, miR-18b and miR-17, together with miR-92b, miR-10b and let-7e were the most important miRNAs of the network, from a positional

perspective (Table 2). These miRNAs control four of six intramodular hubs, namely TP53, MYC, CDK4 and CDK2 which, in this context, can be considered as intermodular hubs, as they connect the two modules (as depicted in Figure 6). This intermodular hubs are for the most part pleiotropic and are directly linked to different biological modules, interacting with different partners at different moments and/or within different cellular compartments. These miRNAs also control the top five genes in terms of *O/E* scores (see Material and Methods, section 1.4 for a detailed explanation of the O/E scoring criterion): CCNA2 (module 1), MYC (module 10), LRP5 (module 8), E2F1 (module 1), HSPA8 (module 3), from the initial list of 391 genes.

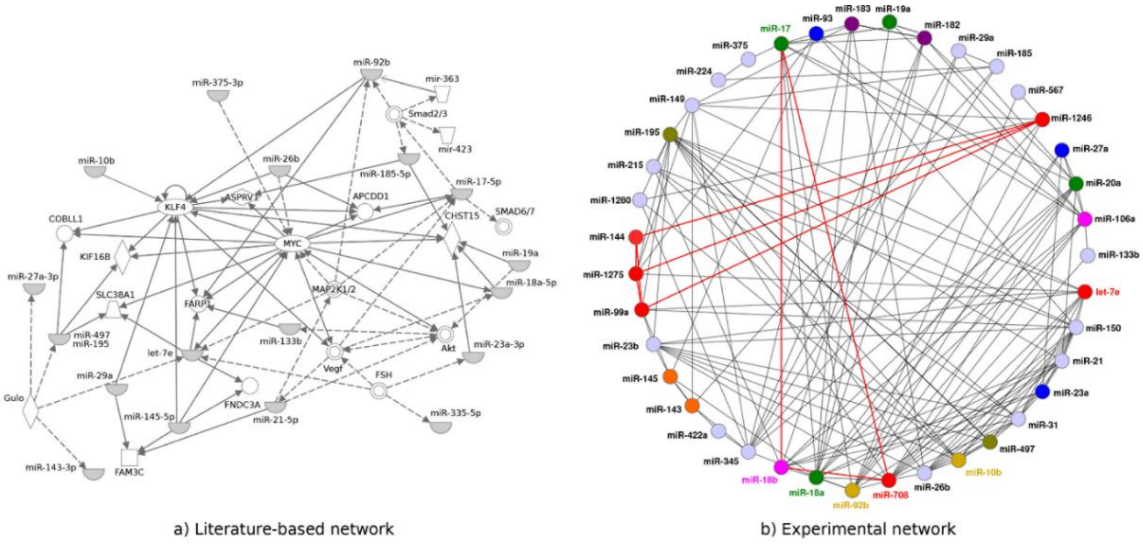

Figure 5: Literature-based and experimental networks of miRNA interactions. (A) Literature-based network: two miRNAs are connected if there is any evidence of physical or (cancer-related) functional interactions. (B) Experimental network: it connects any two miRNAs if they are differentially expressed between matched pairs of tumor and adjacent, non-tumoral mucosa samples and their expression values correlates significantly. Colors represent miRNA clusters. Labels are colored according to the topological importance of the miRNA in the network by means of classical centrality metrics: degree, clustering coefficient, closeness, betweenness. Edges in red emphasize if the miRNA makes a closed triangle or a clique.

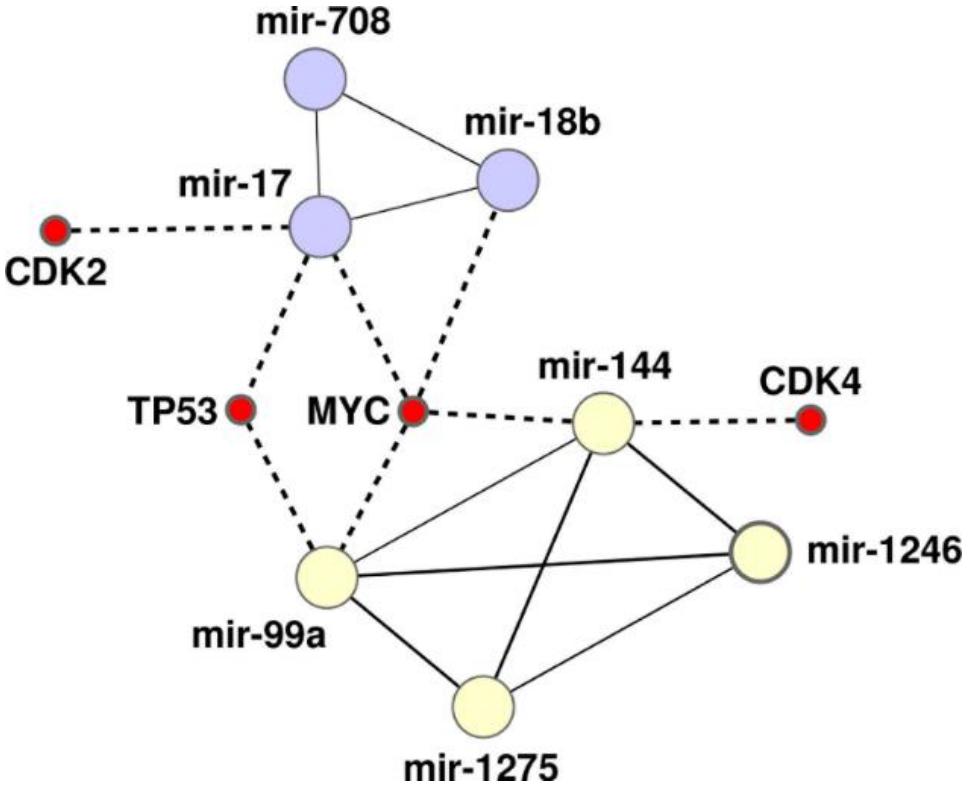

Figure 6: The heterogeneous network of MiRNAs–mRNAs intermodular hubs. The triangle made of miR-708, miR-18b, miR-17 and the clique made of miR-144, miR-1246, miR-1275, miR-99 interacts with four intermodular hub coding genes: TP53, CDK4 and MYC, while the triangle formed by miR-708, miR-18b, miR-17 controls CDK2.

ID	Degree	Betweenness	Closeness	Radiality	Clustering Coefficient	rank
hsa-mir-17	7	0.12114046	0.48611111	0.82380952	0.52380952	4
hsa-mir-18a	9	0.13434641	0.51470588	0.84285714	0.30555556	4
hsa-mir-92b	10	0.16535814	0.51470588	0.84285714	0.24444444	4
hsa-mir-708	14	0.32231693	0.55555556	0.86666667	0.14285714	4
hsa-mir-106a	8	0.0688362	0.49295775	0.82857143	0.32142857	3
hsa-mir-18b	10	0.10160731	0.47945205	0.81904762	0.31111111	3
hsa-mir-10b	8	0.17204106	0.44444444	0.75	0.28571429	2
hsa-mir-31	2	0	0.38043478	0.72857143	1	1
hsa-mir-149	2	0	0.31818182	0.64285714	1	1
hsa-mir-19a	3	2.40E-01	0.37634409	0.72380952	0.66666667	1
hsa-mir-567	2	0	0.36082474	0.7047619	1	1
hsa-mir-144	3	0	0.33333333	0.66666667	1	1
hsa-mir-21	4	0.00640056	0.41666667	0.76666667	0.5	1
hsa-mir-1280	3	0.15368357	0.45283019	0.75833333	0.33333333	1
hsa-mir-27a	5	0.00584634	0.40697674	0.75714286	0.4	1
hsa-mir-20a	5	0.01515806	0.43209877	0.78095238	0.4	1
hsa-mir-182	8	0.09012205	0.42682927	0.77619048	0.28571429	1
hsa-mir-1246	5	0.05109044	0.41666667	0.76666667	0.4	1
hsa-mir-1275	7	0.03921769	0.38888889	0.73809524	0.28571429	1
hsa-mir-99a	8	0.0829972	0.41176471	0.76190476	0.17857143	1
hsa-mir-23b	2	0.00487995	0.39772727	0.74761905	0	0
hsa-mir-26b	2	0.0096732	0.36842105	0.71428571	0	0
hsa-mir-375	2	0.05714286	0.33653846	0.67142857	0	0
hsa-mir-422a	2	0.01171669	0.30434783	0.61904762	0	0
hsa-mir-497	3	0.00642857	0.32407407	0.65238095	0	0
hsa-let-7e	3	0.01291116	0.41176471	0.76190476	0.33333333	0
hsa-mir-345	3	0.0507403	0.39325843	0.74285714	0	0

hsa-mir-23a	5	0.01582166	0.40697674	0.75714286	0.3	0
hsa-mir-143	3	0.07103641	0.32407407	0.65238095	0	0
hsa-mir-150	5	0.049175	0.43209877	0.78095238	0	0
hsa-mir-195	5	0.06793451	0.42682927	0.77619048	0.2	0
hsa-mir-93	4	0.03502268	0.43209877	0.78095238	0	0
hsa-mir-145	4	0.12216687	0.4375	0.78571429	0	0
hsa-mir-133b	1	0	0.36082474	0.7047619	0	0
hsa-mir-215	1	0	0.3271028	0.65714286	0	0
hsa-mir-183	1	0	0.30172414	0.61428571	0	0
hsa-mir-29a	1	0	0.33802817	0.60833333	0	0
hsa-mir-224	1	0	0.25362319	0.50952381	0	0
hsa-mir-185	1	0	0.24647887	0.49047619	0	0

Table 2: Topological centralities for the miRNAs targeting CRC genes in the co-expression and interaction network. Yellow labeled miRNAs identify the closed triangles and the clique identified in the network.

4. The leading topological position of miRNA-145 is fundamental for the upholding of cohesiveness and functional cooperation among modules

Upstream analysis of intra/intermodular hub genes revealed a noticeable mechanistic and topological position of miR-145 (z-score = 2.35), miR-9 (z-score 2.11) and miR-137 (z-score = 2.07). Among these, only mir-145 was found to be differentially expressed in CRC samples.

The hypothesis that miR-145 could be identified as a master regulator of the CRC network was sustained both statistically, by the *experimental* network and functionally by the *literature-based* network. MiR-145 was strongly correlated with the miRNAs in Figure 5B. To verify the importance of miR-145 in the upstream regulation of these miRNAs, the expression profiling was compared in the TCGA database by downloading CRC profile expressions. This analysis not only confirmed that the expression of miR-145 correlates with that of miR-17, miR-23b and miR-99a (one of the seeding nodes) but also that these were likely to be causally dependent on miR-145 ($P < 0.0001$). Besides, let-7e and miR-92b positively correlate with miR-145 (Figures 7A and 7C) and high expression values of let-7e and miR-92b resulted in moderate risk factors, if coupled with high expression values of miR-145 (Figures 7B and 7D). Similarly, low profiles of let-7e and miR-92b conferred a worse prognosis, if coupled with low expression values of miR-145. High values of miR-10b and miR-143, instead, were risk factors if concomitant with low values of miR-145 (data not shown).

More generally, miR-145 resulted to be directly connected with several components of important clusters of miRNAs, which in turn targeted relevant intra/inter-modular hub genes, as reported in Supplementary Table S3. Topologically, miR-145 was linked through miR-93 to the triangle made of miR-708, miR-18b and miR-17 and to the clique made of miR-144, miR-1246, miR-1275 and miR-99a, thereby controlling, even indirectly, four intramodular hubs, specifically *TP53*, *MYC*, *CDK4* and *CDK2*.

We will not discuss the importance here of miR-145 deregulation in colorectal carcinogenesis, well aware that molecular competition represents a universal and frequent form of gene regulation that operates also in RNA regulatory networks. Instead, we will focus here on the short-range interactions of miR-145 with the aim to highlight its apical regulative role on key genes and biological functions related to CRC development.

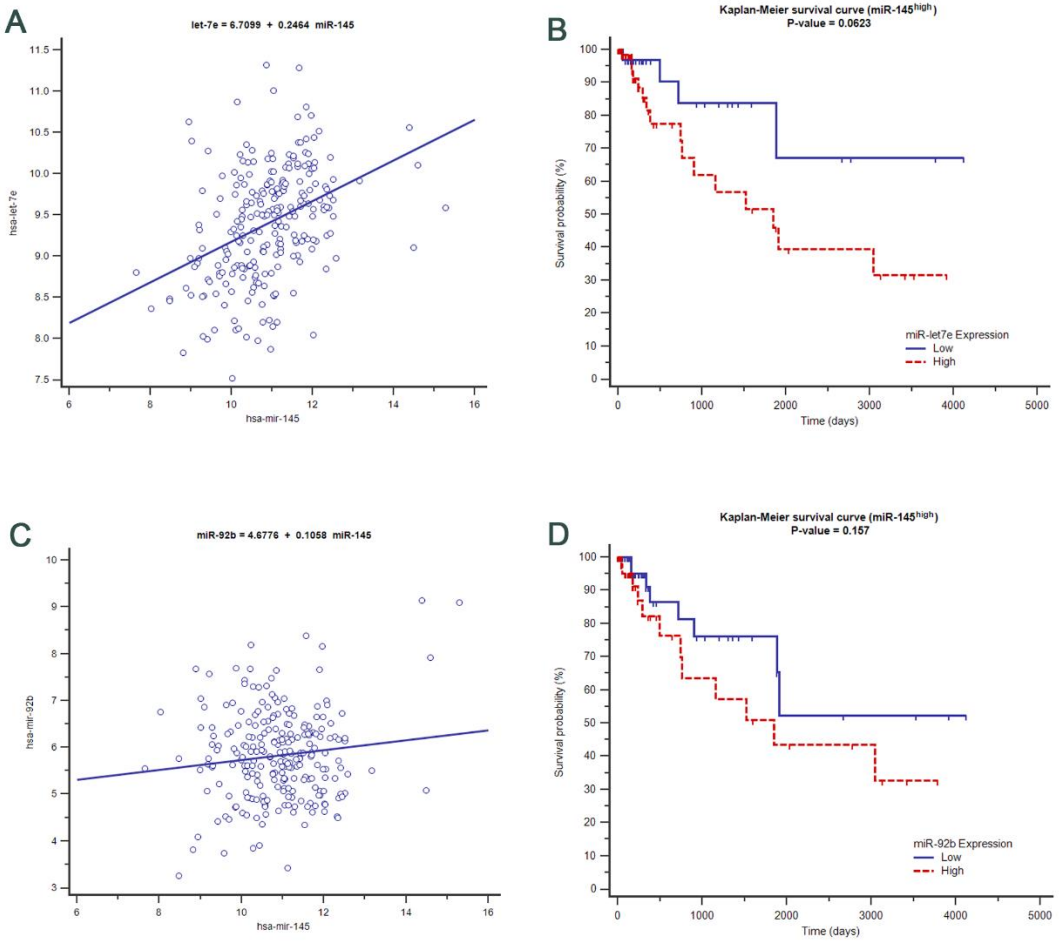

Figure 7: miR-145 associations with important deregulated miRNAs in CRC using TCGA expression level profiles A) correlation between miR-145 expression values and let-7e B) Kaplan-Meier curve of low (below median) and high (above median) expression values of let-7e compared with miR-145 C) correlation between miR-92b and miR-145 D) Kaplan-Meier curve of miR-92b when expression is low (below median) and high (above median) compared to miR-145 expression profiles.

5. Measuring the effect of the induced expression of miR-145 in CRC cell lines

To test the importance of the deregulation of miR-145 and its specific effect on its miRNA partners, we assessed whole miRNA expression *in vitro* in four human colorectal cancer cell lines after miRNA-145 induction (Material and Methods section 1.7). Only miRNAs showing statistically significant differential expression ($P < 0.05$, $\log_2FC \geq 1.5$, $\log_2FC \leq -1.5$) after miR-145 ectopic expression were considered. Several miRNAs were differentially expressed in the four tested cell lines: 82 miRNAs in the CaCo2 cell line (32 up-regulated and 50 down-regulated), 120 miRNAs in HT-29 cells (58 up-regulated and 62 down-regulated), 90 miRNAs in HCT116 cells (49 up-regulated and 41 down-regulated) and 95 miRNAs in the SW480 cell line (58 up-regulated and 37 down-regulated). Among these, three direct partners of miR-145 were modulated in three of four cell lines. In particular, miR-99a was highly down-regulated in CaCo2 cells (p = 0.036, log2 FC = −4.36), miR-23b was mildly down-regulated in the HT29 cell line (p = 0.004, log2 FC = −1.81), and miR-143 was up-regulated in SW480 cells (p = 0.046, log2 FC =1.52). Furthermore, among the deregulated miRNAs, we found at least one miRNA, for each cell line, that was indirectly connected to the miR-145: miR-23a (p =0.004, log2 FC = −5.14) in CaCo2 cells; miR-23a (p =0.008, log2 FC = −1.84) and miR-27a (p =0.039, log2 FC = −2.5) in HT29 cell, with both included in miR23a∼miR27a∼miR24-2 cluster, and being down-regulated; miR-18a* (p = 0.002, log2 FC = 2.32), included in the miR17∼miR92a cluster, and miR-24-1* (P < 0.001, log2 FC = 2.4), included in miR23b∼miR27b∼miR3074 cluster, were up-regulated in SW480 cells. MiR-1246 was also up-regulated in HCT-116 cells (p = 0.041, log2 FC = 3.47) and mildly in HT29 cells (p = 0.038, log2 FC = 1.32).

The enrichment of the direct and indirect targets of miR-145 that resulted from our *in-silico* analysis, other than providing enrichment with several expected cell-cycle related processes, did significantly enrich two important pathways: the PI3K pathway through FGF3, FRAP1 and RPTOR ($p = 0.000049$), the WNT signaling pathway through FZD5, FZD8 and PPP3CA ($p = 0.00039$), and the MAPK signaling pathway through CRK, FAS, MAP3K5, MAP3K8, MAPK14, RAPGEF2, RPS6KA5, TGFBR2, CHUK, DUSP5, MAP4K3, PDGFA, RRAS2, DUSP8, FGF4, HSPA8, FGFR3, FRAP1 and PPP3CA genes ($p = 0.0289$).

6. MAPK signaling pathway is modulated by miR-145 ectopic expression in CRC cell lines

The main impact of miR-145 over-expression induced the expression of several genes participating in the MAPK signalling pathway. Their expression profiles were compared with those measured in cells without miR-145 overexpression, as well as in matched tumorous and adjacent non-tumorous colon tissues obtained from CRC patients (Figure 8A).

Looking in depth at the genes responsible for the CRC development, *CDKN2C* greatly increased its expression both in CaCo2 and in HT-29 cells ($\log_2$ FC = 3.43 and 4.46, respectively), while this differential expression was not observed in the genome-wide profiling study. On the other hand, *MAP2K4* slightly increased its expression in both HCT116 and HT-29 cells ($\log_2$ FC =1.69 and 1.37, respectively), whereas it was significantly down-regulated in the tumor tissues ($\log_2$ FC = -2.87). A similar trend was

observed in HT29 cells for the following genes: *CDKN1A*, *CDKN2B*, *KRAS*, *PRDX6* and *SMAD4*. *KRAS* and *SMAD4* that were up-regulated after transfection (log_2 FC =1.53 and 2.74, respectively), but were down-regulated in our CRC specimens (log_2 FC = −2.63 and −3.1, respectively). Finally, *ELK1* and *CDK2*, which exhibited elevate closeness and degree centrality scores, were both up-regulated in our CRC specimens (log_2 FC = 4.56 and 4.34, respectively). In contrast, *ELK1* was down-regulated in HCT116 cells (log_2 FC = −4.64) and up-regulated in HT-29 cells (log_2 FC = 1.93), while *CDK2* was imperceptibly down-regulated in SW480 cells (log_2 FC = −1.17) and up-regulated in HT-29 cells (log_2 FC = 2.27), after miR-145 transfection (Figure 7B). Interestingly, HT29 cells showed up-regulation of most of the MAPK pathway genes, except for *CDKN1C*, *LAMTOR3* and *RLPO*.

These genes are not direct targets of miR-145, but of miR23a, miR-23b, miR-26b, miR-99a and miR-18a, which in turn, were deregulated in the four cell lines, as an effect of the ectopic expression of 7. miR-145. In fact, we found alterations of both miR-23a and miR-23b in HT-29 cells. Being highly similar in their mature sequences, they are expected to control the same transcripts, which are known to mostly belong to the KRAS and TGFβ signalling pathways, and which, in our study, are those of the *K-RAS*, *cMYC* and *E2F1* genes, as reported in Figure 8B.

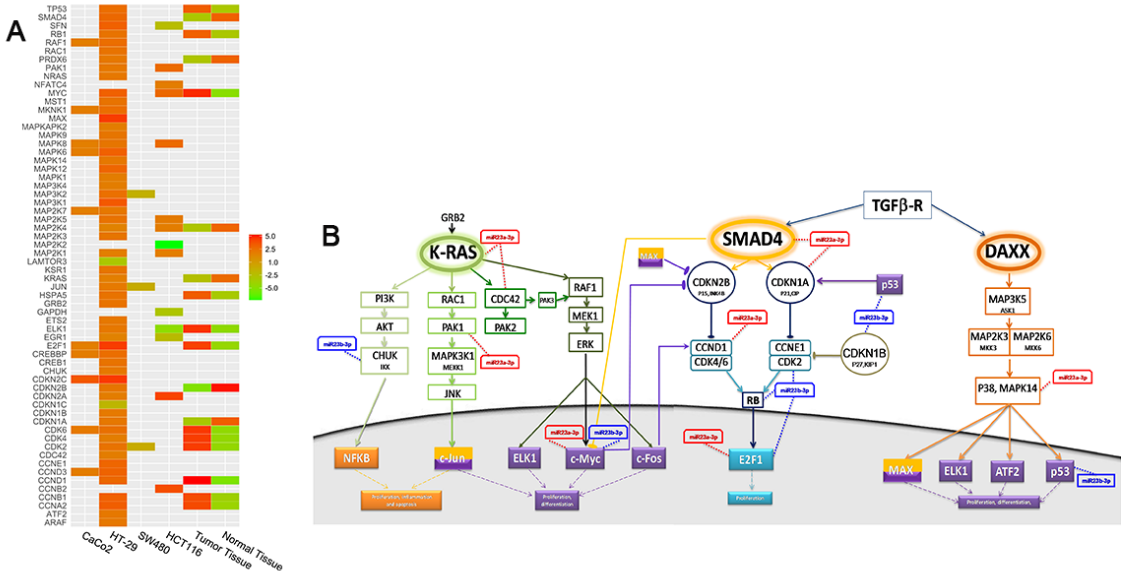

Figure 8: A) Heatmap of the expression levels of the genes composing the MAPK signaling pathway in four CRC cell lines after miR-145 ectopic expression. For comparative purposes, gene expression values of matched pairs of tumor and adjacent non-tumorous mucosa samples are also reported. B) The downstream effects of miR-145 ectopic expression: Pathway map representing the downstream effects of the miR-145 ectopic expression in the HT-29 cell line.

7. Conclusions

The integrative analysis of mRNA–miRNA and miRNA–miRNA interactions identified two *cancer-protection* and nine *cancer-favourable* modules of genes and provided interesting evidence on mRNA–miRNA crosstalk in CRC. Several genes emerged that demonstrated a relevant dual role, both being *intramodular* and *intermodular* hubs in the interaction network built from experimental interaction evidences. A strongly connected sub-network was made up, in fact, by *TP53*, *MYC*, *CDK4*, *CTNNB1*, *CHEK1* and *CDK2*, which were the most central genes (some of the *intramodular hubs*). *CDK4*, *CDK2* and especially *TP53* and *MYC* also acted as *intermodular hubs* because they connected two cohesive clusters, the one made of miR-99a, miR-144 and miR-1275, for which miR-1246 worked as seeding node, and the triangle made up of miR-18b, miR-708 and miR-17, the latter being the seeding node.

The expression level of miR-145 was highly correlated with the above-mentioned clique and triangle and, directly or indirectly, with miR-93, miR-143, miR-18a, miR-23a and miR-23b, miR-31, miR-345, miR26b, miR-185 and miR-20a, thus acting as potent modulator of four *intramodular hubs*, namely *TP53*, *MYC*, *CDK4* and *CDK2I*, and as the genuine actuator of a number of important biological functions and pathways (Mogilyansky and Rigoutsos, 2013; Olive et al., 2010; Sylvestre et al., 2007).

First, miR-145 demonstrated to exert a certain control on the cell cycle process through a series of partners: *BCL2*, *FAS*, *PPIF*, *MYC* and *E2F1*. The control of mir-145 over *MYC* is of particular importance, as it promotes the transcription of the polycistronic cluster miR-17∼92 (also known as oncomiR-1) one of the most potent oncogenic

clusters, participating to cell proliferation and apoptosis control (Woods et al., 2007). The regulation of miR-145 to *E2F1* is also crucial because it binds to the promoter region of the miR-17~92. In particular, miR-145 evidenced a significantly negative causal influence on two of the six members of this cluster, miR-17 and miR-18a. The concomitant lower expression values of miR-145 and miR-18a are prognostic evidence of poor survival as emerged from analysis of TCGA data. In a network perspective, we notice that *E2F1* exhibits the highest clustering coefficient score, confirming its high connectedness in the whole network and of their tight relationships with its interacting neighbourhood. Most of the components of this cluster are directly linked to miR-145 (Figure 3B). The control on cell cycle-related processes by miR-145 is strengthened by its indirect modulation of the expression of miR-21 (Figure 3B) and by the direct control of *CDC25A* and *CDK6* genes (the *CDK6* gene, in particular, was the 10th gene in descending order for closeness centrality).

Second, miR-145 ectopic expression in CRC cell lines triggered the downstream deregulation of critical genes, a significantly high number of which are closely related to the MAPK signaling pathway. *MYC* is activated by various mitogenic signals, such as WNT, SHH and EGF, via the MAPK/ERK signaling pathway, and was found to be aberrantly expressed in our dataset. Equally, ELK1, which is known to induce the *c-fos* proto-oncogene upon phosphorylation by MAPKs (Hipskind et al., 1991), was deregulated in our cell lines, being under the control of miR-143, which in turn correlates with miR-145. *CDK2* regulates G1/S transition and S phase progression in association with cyclin E and A. Its activation is dependent on its localization in the nucleus, which can happen upon the formation of *CDK2/MAP* Kinase complexes (Blanchard et al., 2000). MiR-145 has a double indirect influence on this gene, via the MAPK signaling

pathway and because of its negative correlation with miR-18a, of which *CDK2* is a theoretical target. MAPKs are also known to modulate the outcome of SMAD activation by TGF-β. Cross-signalling mechanisms between the SMAD and MAPK pathways take place and affect cell fate in the context of carcinogenesis (Javelaud and Mauviel, 2005). MiR-145 exerts a double control even on *SMAD4* (module 3), modulating the MAPKs and directly targeting *SMAD4*.

Third, miR-145 was tightly connected with miR-143, in line with the literature. They share numerous target genes involved in various cancer-related events, with both influencing phenotypic patterns, as evidenced by experiments entailing the concomitant ectopic expression of the miR-143~miR-145 polycistronic cluster in the HT-29, HCT116 and SW480 cell lines, and showing significant decrease in *proliferation*, *migration*, *anchorage-independent growth* and *chemoresistance*; these miRNAs can work independently or synergistically, with an effect on the colon cancer transcriptome and proteome being characterized by distinct and shared functional effects (Akao et al., 2006; Bauer and Hummon, 2012; Pagliuca et al., 2013). The miR-143~miR-145 polycistronic cluster targets the RAS-responsive element-binding protein (RREB1) and KRAS (Chen et al., 2009b), which, in turn, induce down-regulation of the cluster, thereby sustaining a feed-forward mechanism (Kent et al., 2010) that could explain the concurrent down-regulation of KRAS and miR-143~miR-145 cluster in our CRC cohort. From this study, it emerges that it is likely that miR-143 is an effector of miR-145, rather than being equal cooperators. By the analysis of TCGA data it comes out that the expression of miR-143 is linearly dependent on the expression of miR-145 and that the prognosis of the patients with low levels of miR-145 and high levels of miR-143 is dismal.

In conclusion, the simultaneous evaluation of the transcriptome and miRNAome of matched pairs of tumor and adjacent non-tumorous mucosa samples of CRC patients helped to identify several modules of genes and miRNAs. A multifaceted enrichment analysis through network construction revealed that these modules can cooperate, rather compete, as micro-societies, in the fulfilment of pathophysiological mechanisms underlying the onset and development of CRC. Although several, if not all, members of these clusters could potentially be considered good prognostic and therapeutic targets, many of them, alone, proved to be globally ineffective in the treatment of the disease. For this reason, the hunt for biomarkers shifts attention towards the master-regulators, i.e. the molecules that, when pharmaceutically targeted, can plausibly result in a maximal derangement and destabilization of the core tumor machinery. We focused on miR-145, which, following *in silico* and *in vitro* analysis, demonstrated a high potential in this direction and could be reliably targeted for diagnostic and prognostic purposes, and, indirectly, to provide new therapeutic targets for coding genes using known and novel gene-to-miRNA relationships.

2. Pyntacle: a tool for the assessment of critical properties of networks

1. Background

The plasticity of the relationships among cellular functions was well explained using network models for several model organisms such as for example, the *Saccharomyces cerevisiae*. The study of the geometrical organization (topology) of its PPI network allowed the identification of a group of key proteins that are more tightly connected than the rest of the proteins in the *interactome* network (Figure 9), a typical feature that characterizes the so called *scale-free* networks (Barabási and Albert, 1999). This result supported several other studies to establish a direct relationship between the connectivity of proteins and their importance in a network. Another important feature of PPI networks, which arose after this first result, was that the removal of single genes in a PPI network does not alter dramatically the phenotype of an organism, as the removal of hub proteins does. Hence, PPI networks were reported to be scale-free, although statistical analysis has refuted many of these claims and seriously questioned others (Clauset et al., 2009), and that their architectural configuration was an immediate proxy for the functional activity of the organism that network was abstracted from. The echoes of these achievements were sensed by Medicine as well. Graph models were used to attempt to figure out disease mechanisms of onset and development. The key point of view was that a disease phenotype is rarely the consequence of the malfunctioning of an individual effector molecule, rather it summarizes various pathophysiological processes that result from several components of the network.

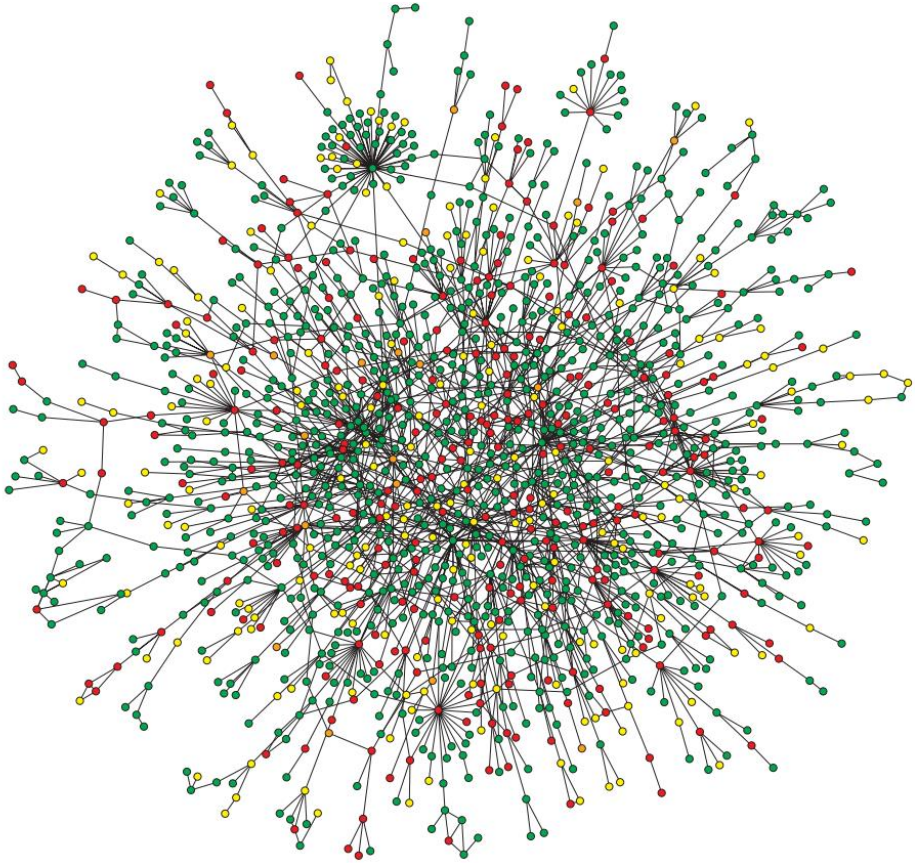

Figure 9: The largest component of the S. cerevisiae PPI network taken from (Jeong et al., 2001). Protein (nodes) are colored according to their phenotypic effect when deleted: red = lethal, green = non-lethal, orange = slow growth, yellow=unknown.

Network medicine (Barabasi et al., 2011) exploits graph theory to thoroughly understand the architecture of the human *diseasome* (Goh et al., 2007; Wysocki and Ritter, 2011), a

graph in which nodes are cellular components linked if they contribute to the disease phenotype.

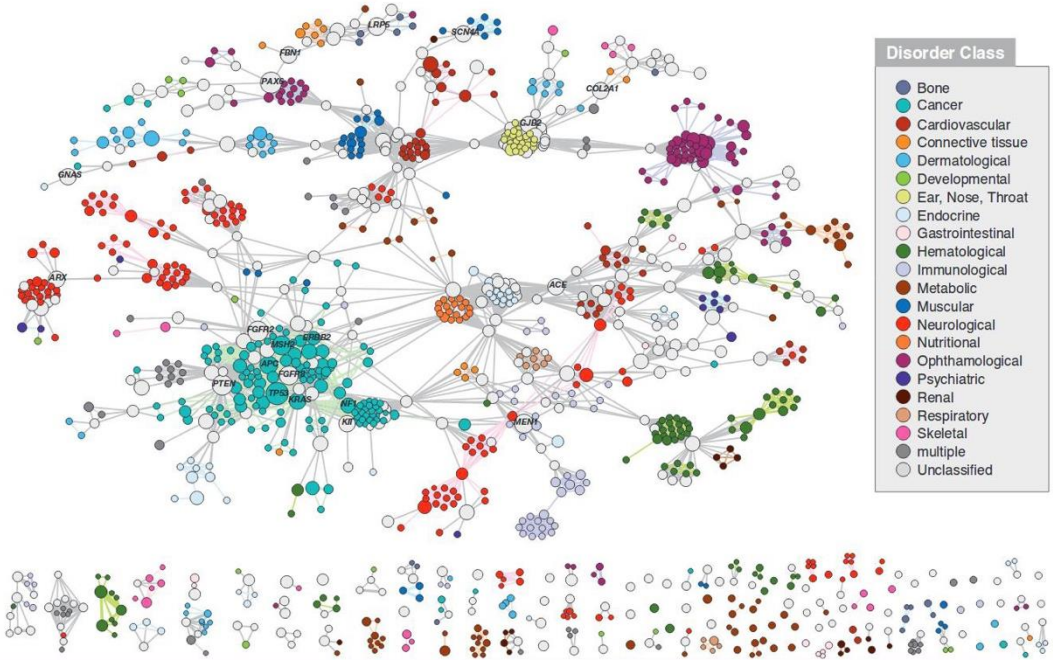

Figure 10: The Disease Gene Network (DGN) of *Homo sapiens* taken from (Goh et al., 2007). Each node is a gene, and they are connected if they are implicated in the same disorder. The width of the node is proportional to the number of disorders the gene is found to be implicated in. Colored nodes mark genes that are implicated into a single disease family, dark grey genes mark genes that are associated with multiple diseases class and light grey genes are unclassified.

This theoretical approach is particularly beneficial when dealing with polygenic disorders or complex traits, where the abnormality in a single effector gene product fails to explain the pathogenesis of a disease. These models, like the one depicted in Figure 10, enabled to study the interplay among biomarkers of distinct phenotypes and to find and acknowledge the common molecules among several diseases. Graph theory provides a number of tools to identify the most central nodes within a network. Here the concept of centrality is synonymous of importance. A topologically important node may be that with many relationships with other nodes or the one that lies in many pathways or again that is closer to most other nodes (Pavlopoulos et al., 2011). In this context, importance matters and is secondary to the topological structure of a network. A basic assumption is in fact that biological systems are nonrandom in nature, but that are tightly organized in structures that underlie hierarchical structures (Ravasz et al., 2002). Besides, the study of local and global properties of individual nodes and networks partially explained the mechanics of complex systems, leaving the team play effect of nodes on the whole systems largely unexplored. In fact, although much explicative, global and local centrality metrics such those described in Materials and Methods, Section 2.4) do not capture the combined effects of groups of nodes, their systemic interplay and the role they exert on a network. The majority of cellular functions are in fact fulfilled by groups of genes, each playing a peculiar role in the cell functioning. Programmed Cell Death, for example, is a multifaceted, intracellular process that requires the cooperative effects of many genes to occur, as there is no upstream gene that can initiate the apoptotic cascade alone (Xu et al., 2009). Moreover, these genes often do not directly interact with each other, rather they target overlapping sets of genes and transcription factors to exert their

functions. For this reason, new topological metrics able to measure the centrality of groups of nodes are needed. Pyntacle attempts to answer this need.

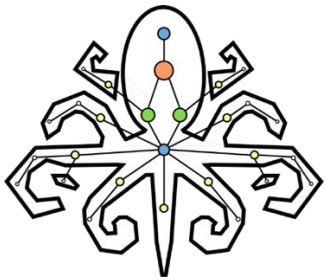

Figure 11: The Pyntacle Official Logo.

2. Pyntacle functionalities

Pyntacle is both an open-source command line tool and a Python 3 package. Its dual nature allows its use as both a command line and as a standalone tool for network analysis. Pyntacle faces the problem of identifying *key-player* nodes that, together, optimally diffuse something through a network or that maximally disrupt or fragment a network when removed. These problems can be solved optimally, by the greedy heuristics presented in (Borgatti, 2006), or exactly by a brute-force combinatorial optimization strategy. The latter yields all tied groups of nodes that exhibit the best solutions for both problems. It is implemented to fits snugly into the memory of a PC and to mitigate the combinatorial explosion phenomenon of huge networks when using HPC

clusters equipped with many computing cores. Table 3 pinpoints the main Pyntacle functions.

The possibility to choose between an exact, but slow optimization method rather than a suboptimal, but fast method ensures flexibility to researchers: the greedily optimized search of groups of key-players is recommended when dealing with big networks (over 1,000 nodes). On the other hand, brute-force search reports all the best solutions, at the cost of increasing running times. It is thus recommended with small networks. More details regarding the key-player metrics implemented in Pyntacle can be found in Material and Methods, section 2.5. Although real-world problems are typically sparse and can be solved by algorithms that work best with graphs that have few edges, many of the algorithms in Pyntacle are optimized to work with increasingly complex networks. Along with key-players concepts, we have implemented indices to quantify the sparseness of graphs (Mazza et al., 2010; Randic, 1997), including the compactness and completeness indices, which Pyntacle takes as reference metrics to assess the global complexity of graphs. Additionally, Pyntacle implements the *radiality* topological index. Radiality is a node centrality measure that is commonly used to assess node centrality in combination with closeness and eigenvector centrality. In a PPI network, radiality can be interpreted as the *probability* of a protein to be functionally relevant for several other proteins, but with the possibility to be irrelevant for a few other proteins. Thus, a protein

Command	Modules	Brief Description
keyplayer	kp-finder	Find the set of length X for each KP metric
	kp-info	Find KP metrics for a specific set of nodes
metrics	global	Compute Global Metrics for the whole graph
	local	Compute local metrics for each node, or a subset of nodes
set	union	Merge two graphs
	intersection	Intersect Two graphs
	difference	Find the exclusive edge set in two graphs
convert		Convert one network file into another one
communities	fastgreedy	Divide your sugraph into modules (A Clauset, MEJ Newman and C Moore: Finding community structure in very large networks)
	leading-eigenvector	Divide your sugraph into modules (Newman: Finding community structure in networks using the eigenvectors of matrices)
	community-walktrap	Divide your sugraph into modules using random walks (Pascal Pons, Matthieu Latapy: Computing communities in large networks using random walks)
	infomap	Divide your sugraph into modules (M. Rosvall and C. T. Bergstrom: Maps of information flow reveal community structure in complex networks)
generate		Generate Random networks based on several topologies and criteria (for simulation purposes)

Table 3: Pyntacle command line main commands and subcommands, when available.

with high radiality, compared to the average radiality of the network, will be easily central to the regulation of other proteins but with some proteins not influenced by its activity. Thus, a network with a very high average radiality is more likely to be organized in functional modules, whereas a network with very low average radiality will behave more likely as an open cluster of proteins connecting different regulatory modules. All these interpretations are often accompanied with the contemporary evaluation of eccentricity and closeness. Since radiality suffers for networks with one giant component and many small components, we implemented the *radiality-reach* metrics, which simply applies to each component, independently. A detailed description of all the implemented metrics in Pyntacle is given in the Materials and Methods chapter, section 2.4.

Analysis of signaling pathways and their cross-talks is a cornerstone of Systems Biology. A number of developmental processes rely on cross-talk, and their aberrant regulation was associated to inflammatory response defects as well as to cancer and neurodegeneration (Espinoza and Miele, 2013; Mazzoccoli et al., 2014; Yu and Kang, 2013). Studying the cross-talks among interacting pathways is challenging, also because it depends on the organism, tissue, environment, and the experimental settings. Looking at pathways as individual networks, Pyntacle eases the exploration of their cross-talks by means of logical set operations: *union*, *intersection*, and *difference*. Isolated pathways can thus be compared or merged and then studied topologically using the set of operations available in Pyntacle.

Biological organization of real systems has been proven to be modular, also at a molecular level (Hartwell et al., 1999). Molecular systems often exert their activity by organizing the genome into regulatory modules, which are sets of co-regulated genes that

share a common function (Segal et al., 2003). These modules undergo aberrant reshaping when molecular functions are altered, such as in cancer (Thiagalingam, 2006; Wu and Stein, 2012). Hence, the identification of modules in networks is a compelling task in Network Biology. The literature is wide on this regard, and the quest for optimally defining communities is still open, with many algorithms proposed in as many contexts (Habib and Paul, 2010). A carefully selected subset of them where wrapped and added to Pyntacle, which include: the well-known community *fastgreedy* algorithm (Clauset et al., 2004), especially designed for large networks (over 1,000 nodes); the *eigenvector* method (Newman, 2006), which defines a measure of modularity between groups of nodes and tries to maximize it by iterative node swapping; two methods based on random walks, namely the community *infomap* (Rosvall and Bergstrom, 2007) and the community *walktrap* algorithm (Pons and Latapy, 2006). (For details please jump to the Materials and Methods chapter, section 2.7). These algorithms can partially be tuned by passing specific command line parameters. In addition, modules can be filtered according to specific criteria (e.g., minimum or maximum number of nodes, number of components, etc.).

Networks can be represented in a variety of data formats. This is a crucial issue, as these data formats vary greatly in size, structure, and metadata attached to nodes and edges. When designing Pyntacle, we committed to the task of relieving the user from the burden of creating Pyntacle-compliant input files. Pyntacle can load and write adjacency matrices, edge lists and DOT files as textual files or Python pickles as binary files in order to be compatible with the major network analysis and visualization tools, like Gephi (Bastian et al., 2009) and UCINET (Borgatti et al., 2002). Moreover, it is fully compatible with Cytoscape (Shannon et al., 2003) through the SIF and DOT languages. Additional

information, namely properties and attributes of graphs, nodes or edges can be imported both via command line and through the Pyntacle library. These file formats are thoroughly addressed in the Material and Methods, chapter, section 2.8. Furthermore, thanks to the Pyntacle convertion tool, it is possible to quickly convert one file format into another.

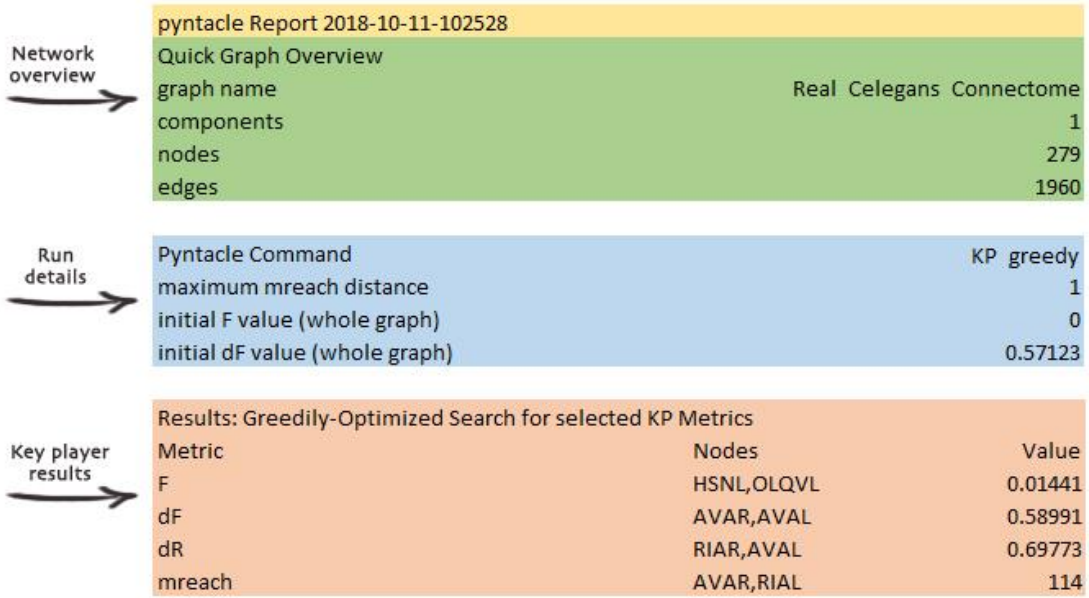

Figure 12: Pyntacle example report of the results obtained using the greedy optimization method on the *Caenorhabditis elegans* connectome.

When studying real-world networks, it is common practice to compare any finding obtained with them with those obtained with simulated, theoretical, networks. The

Connectome of *Caenorhabditis elegans* (White et al., 1986), which is the first complete map of all the connections among the neurons of the small nematode, for example, has been long since thought to have a scale-free topology, whereas several studies proved that the assortment of its links and the node degree distribution approximate its topology to a small-world network (Amaral et al., 2000; Towlson et al., 2013). This incongruence has, of course, an important impact on any topological interpretation one might conclude on this network. For this reason, we equipped Pyntacle with a series of *in-silico* network generators. They can create Erdos-Renyi models (Erdős and Rényi, 1959), Watts-Strogatz small-world networks (Watts and Strogatz, 1998), Barabasi-Albert scale-free graphs (Barabási and Albert, 1999) and hierarchical tree networks (Bradley, 2001).

Pyntacle reports the results of its analyses in textual, Excel or binary files. One example report is shown in Figure 12. In particular, the binary file is actually a pickle binary file that can be easily imported in other Python programs and that significantly compresses the size of the embedded network. Visualization is also a key-feature of Pyntacle. It produces ready-to-publish graph images using the *cairo* package (https://cairographics.org/), a cross-platform graphic library with portings for several interpreters, from C to Python. Plots are produced, by default, for small networks (less than 1000 nodes), although the user can choose not to plot the graph at all. Images can be saved in several file formats, like *svg*, *pdf* and *png*. Nodes in graphs can be arranged by means of known layout algorithms as, for example, the *Fruchterman-Reingold* layout (Fruchterman and Reingold, 1991), the *force-directed* layout, which is best suited for graphs that exhibit scale free topologies, the *Reingold-Tilford* layout (Reingold and Tilford, 1981), which is best suited for trees and networks with hierarchies, such as transcriptional cascades. Plots features are customized according to the type of analysis.

For key-player analysis, for example (Figure 13A), key-player nodes are greater in radius than the other nodes and are colored differently, according to the key-player metric. When measuring the global properties of a network, the user can choose to remove a subset of nodes and then compare how global properties change with and without the removed nodes. In this case, we provide two plots, one before and one after the node removal, marking the nodes that have been removed with different colors and sizes (Figure 13B and Figure 13C) When detecting communities, we plot all the communities found in a network in separate files using custom color-codes option, as shown in Figure 13D and Figure 13E.

Many of the Pyntacle functionalities are prone for High-Performance Computing (HPC) devices, thereby allowing the user to speed up the code execution. Pyntacle is in fact able to use both CPU multi-threading and GPU acceleration by resorting to Numba, a Python library that translates a subset of Python and NumPy instructions into machine code using Just-In-Time (JIT) compilation. The core of Pyntacle is built around the *igraph* package (Csárdi and Nepusz, 2006), an open source portable Python library capable of handling huge graphs with millions of vertices and edges. We choose to resort to *igraph* not only for its capability of storing networks of considerable sizes but also because its graph object can encase several layers of information and allows fast computation of a wide variety of network types. While, currently, Pyntacle supports only unweighted, undirected graphs with binary relationships, the use of the *igraph* library allows further extensions to other network types, such as directed, weighted, signed and bipartite networks. Finally, *igraph* is widely used in the network biology community: several tools were designed around it (Cowley et al., 2012; Revell; Türei et al., 2016) and its use was

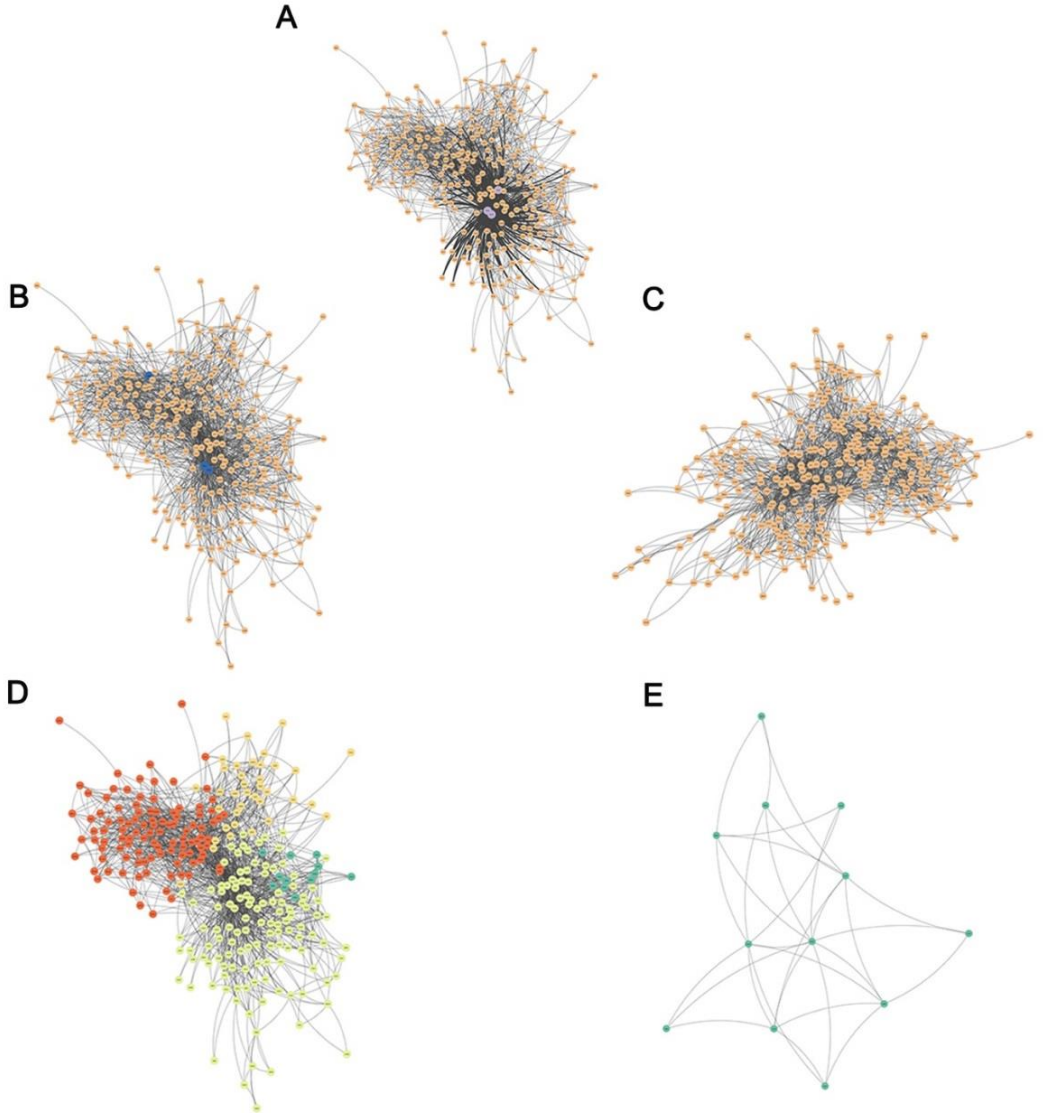
A
B
C
D
E

Figure 13: Examples of Pyntacle plots for the C. elegans connectome. A) optimal key-player set for *dF* (in pink), and its direct neighbours; B) Plot produced before and C) after the removal of the nodes marked in blue; D) communites identified with the *fastgreedy* algorithm; E) the induced subgraph of D) for the dark green community.

proficient in several independent studies (Xie et al., 2018). Hence, its universality allows Pyntacle to be used in different contexts and to be exploited maximally.

On our official website: http://pyntacle.css-mendel.it, we provide full documentation, installation guides, tutorials, case studies, benchmarks and other information about Pyntacle. Some of these are reported in the Appendix of this work of thesis.

3. Pyntacle benchmarks and performance comparisons

Pyntacle is not the only tool that can search set of key-player nodes. To date, two other network analysis tools exist that are able to perform this task using a *greedy optimization* strategy. The first one is a standalone application that runs on Windows and was designed by Borgatti in 2006 (http://www.analytictech.com/keyplayer/keyplayer.htm). This software package is part of the UCINET software ecosystem (Borgatti et al., 2002) and is accessed through a graphical user interface. Unfortunately, it crashes and stops working when importing networks of moderate size (N>500), regardless of the machine's memory and hardware architecture. These two hurdles made difficult to perform benchmarks of this tool. The other available tool is the *keyplayer* R package (An and Liu, 2016a), a collection of different R scripts that compute the key-player search over adjacency matrices imported in R as dataframes. The performances of the two packages were measured on single-core greedy optimization runs on a series of both real and *in-silico*

test networks of different sizes, setting the kp-set size to 2. We distinguished between small, medium and large size networks and measured the elapsed time in seconds (Figure 14). Extensive description of the test datasets and the benchmarks setup can be found in Materials and Methods, section 2.9 and 2.10. Each measurement was done in triplicate.

A notable difference in computing times was found between Pyntacle and the R library, as Pyntacle was generally faster for all metrics and with small and medium-sized networks (Figure 14). Besides, only Pyntacle was able to find optimal key-player sets for large-sized graphs in a reasonable amount of time (<1 week). The *dF* metrics is the most computationally complex since it requires to recompute the shortest path distance matrix for all nodes at each algorithm iteration. Despite this, Pyntacle is still faster than the *keyplayer* R package.

The *brute-force* search was run in parallel on 1, 4, 8, 16, and 32 CPU cores on small and mid-size networks. Speedups measurements revealed that the peak in performance was generally achieved with 8 CPU cores when calculating the *dF* index (Figure 15). Since the other indices were generally simpler than *dF*, we did not verify any improvement in performance resorting to parallel computing. This finding is expected, as the parallel brute-force execution is designed for large graphs.

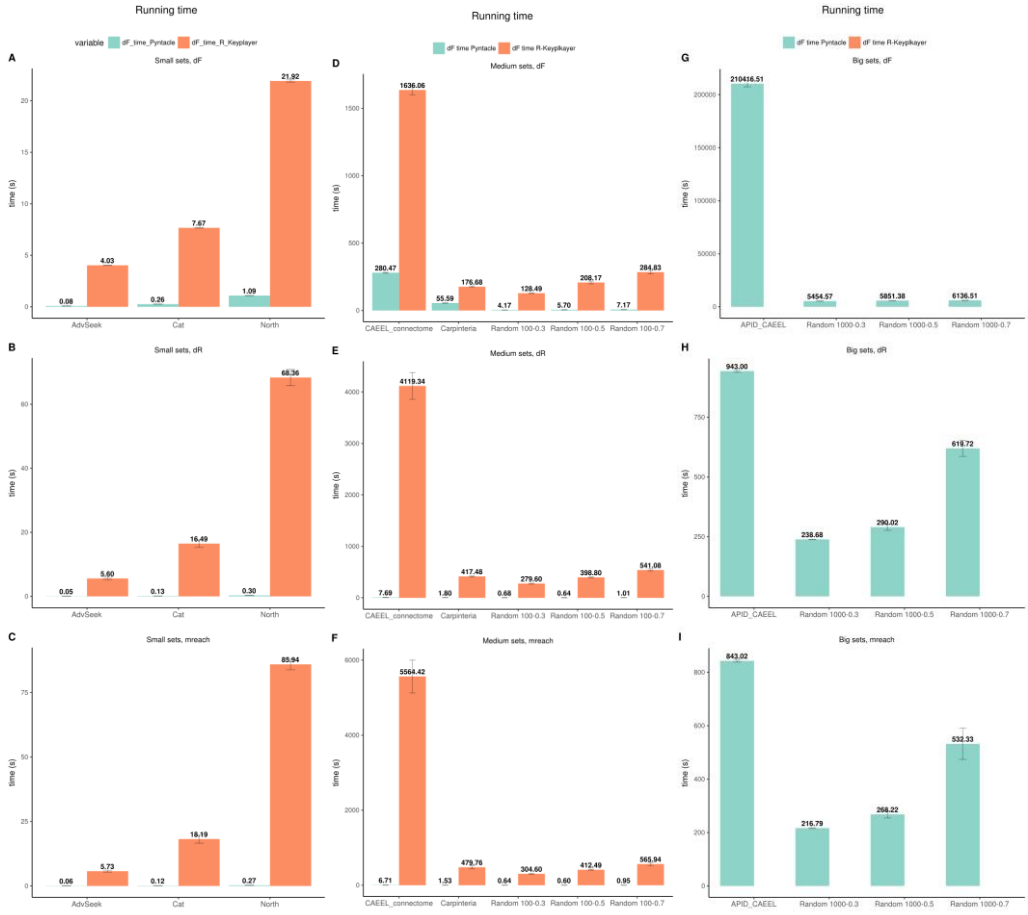

Figure 14: Computation times for the *greedy optimization* search performed with Pyntacle (green bars) and the *keyplayer* R package (orange bars). Times are measured in seconds and averaged over three replicates. For small networks (A-C), medium networks (D-F) and large networks (D-F). Each column represents a different comparable key player metric. For large networks, the R keyplayer package failed to make a single run after 1 week of execution, hence it's not shown.

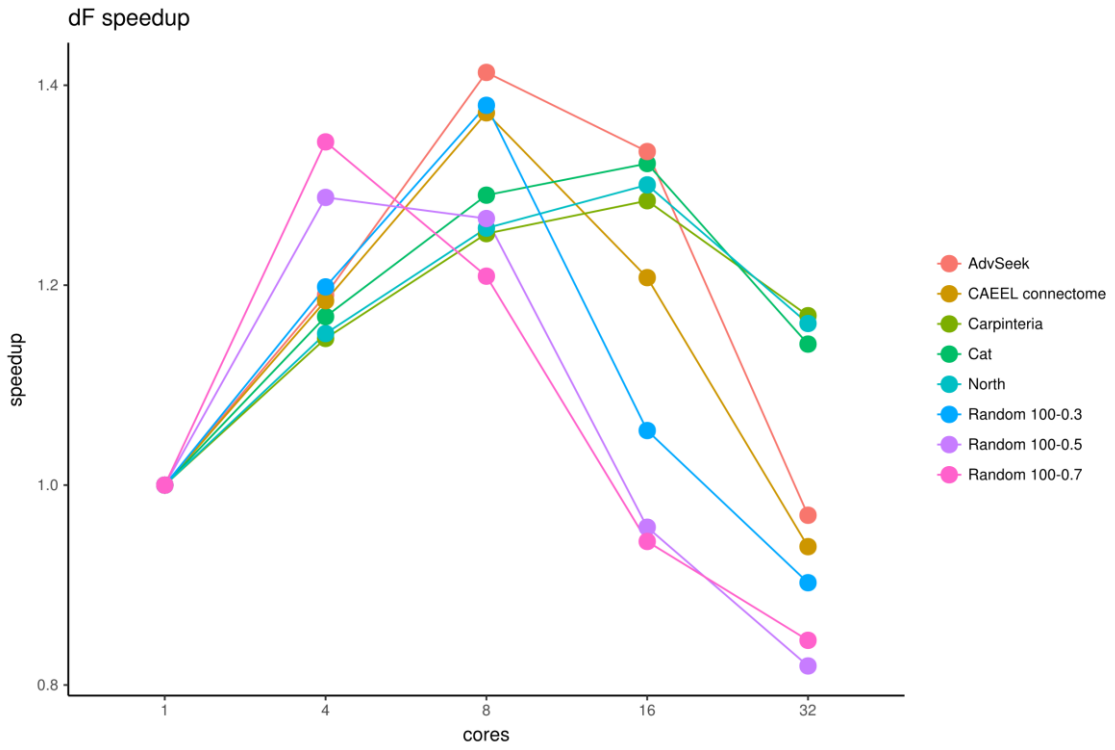

Figure 15: Speedup times for *dF* using Pyntacle key player search by means of the brute-force search algorithm. Times were computed for 4,8 16 and 32 CPU cores over the times at a single core.

4. The future of Pyntacle

Pyntacle is still in its primes and is actively implemented and extended. To present (Oct 2018), 12 versions of Pyntacle were released on our GitHub page (https://github.com/mazzalab/pyntacle). These releases added several new functionalities, corrected bugs, increased portability, usability and interoperability across operative systems and greatly enhanced the speed and the reliability of algorithms, as

well as providing insightful documentation on methods, classes and case examples. The ultimate goal is to make Pyntacle a swiss-knife for network analysis, encasing both known algorithms in molecular network biology, metrics and techniques for disentangling the complexity of biological systems. The focus remains on the understanding of the orchestrated role of key groups of nodes. Indeed, other measures of group centrality exist, other than the fragmentation and reachability, like for example the group centrality metrics (Everett and Borgatti, 2005), that we plan to implement in the next releases. These metrics were conceived in the context of social sciences and consist in the adaptation of classical topological metrics designed for individual nodes, like the degree, betweenness and closeness, to groups of nodes. Their main implications are in the assessment of network *redundancy*: in a social network, if the ties issuing from a node are redundant, then they can be removed without affecting the centrality of the group of nodes which it belongs to. Similarly, with PPI network, a protein with high degree may be thought to be very important. However, its removal may have no effect on the overall network connectivity because there might exist other nodes whose links might equally bridge the neighborhood of the removed node.

While Social Sciences contribute significantly in the development of Network Biology, Ecology was second to none. Ecological networks were used to represent trophic interactions among species in the same ecosystem (food webs), relationships between individuals of the same species (animal social networks) or the population flow between habitable patches (landscape ecology) (Pereira and Jordán, 2017). These systems are very different. The study of complex ecological systems is challenging, as the spectrum of problems is wide. Thus, ecologists need effective tools to get insights onto their systems of interest. These same tools could then be used with the molecular networks, even though

most of them are still unknown to the molecular biology community. This is an issue largely underrated, as these tools could bring novelty to the field and propose new strategies for determining key-molecules in a molecular network. For example, a known rule of thumb is that a protein exerts its function at-most within its two steps neighborhood, in a molecular network. After two steps, its effects are irrelevant. At present, no topological measures are used to quantify the indirect effects of molecules in a network, measures that are instead being theorized for decades in Ecology (Wootton, 1994), to assess how the dramatic changes in a population may affect the rest of the ecological niche. These indirect interactions can be weighted and measured, to a certain extent, with various topological measures. Among these, we put particular attention to the *Ti* and *Wi* indices (Jordán et al., 2014), which are used to measure the importance of keystone species (species that are important for the essential maintenance of a system) in a food web. With Pyntacle, we aim to implement these new features soon and test them on known biological networks, with the aim at analyzing the whole human interactome.
Currently, Pyntacle deals only with graphs. We plan to enable Pyntacle to also work with weighted and signed networks and to make it more accessible to the scientific community. Finally, while Pyntacle is already able to import and export networks in a variety of data formats, it will be compatible with all tools that *speak* the Systems Biology Markup Language (SBML)(Hucka et al., 2003) and the KEGGML (https://www.kegg.jp/kegg/xml/docs/) format. Parsers for these file formats will be designed and implemented in the next Pyntacle releases.

3. The *nestedness* of food-webs

1. Background

Our planet is currently facing the sixth mass extinction from the origin of life. Extinction rates of species rose dramatically, from one to three species per hour in the last decades (Lawton and May, 1996); anthropogenic contribution was essential to this acceleration (De Vos et al., 2015), and apparently no solution exists a to slow down this process in the short term. We know that biodiversity is important, but we do not yet clearly understand its functional aspects and the possible ways to maintain it (Terborgh, 1999). To understand the functional diversity, we would need to know more about the roles that species play in ecological communities (Jones et al., 1994; Timon McPhearson, 2003). For these reasons, food webs, complex ecological networks depicting the relationship among species and their hierarchies, became a proxy to understand the dynamics of ecosystems and to develop strategies for ecosystem management and upkeep. The ability of an ecosystem to function depends on its state and the processes that support it (Mumby et al., 2014). Because ecosystem state and processes are dynamic and influenced by many forms of stress (Hastings, 2010), a vast literature exists on the subject of food webs *resilience* (Gunderson). Resilience in ecology is the ability of ecosystems to shift the communities that composes them even in the absence of acute disturbance events (Scheffer and Carpenter, 2003), while maintaining their balance. Resilience is a proxy to study the evolutionary trajectories of endangered ecosystems such as coral reefs (Mumby et al., 2013) where it was used to prove that, in the Caribbean reefs, the ecosystem could resist by replacing corals with seaweed.

While resilience is a proxy for vulnerability studies and ecosystem maintenance, other indicators exist that can be used to assess ecosystem properties and their reaction to external changes, such as *vulnerability* (Füssel and Klein, 2006; Turner et al., 2003) and *robustness* (Carlson and Doyle, 2002). These features are widely studied not only in ecology, but in social network analysis as well. The first one attempts to measure the expected harm experienced by a system due to its exposure to a disturbance, and it is widely used in risk-hazard research when assessing the anthropogenic effect or major climate change disruption on endangered ecosyst2. ems.

The second one, robustness, was borrowed from engineering and control theory (Carlson and Doyle, 2002). Robustness is defined as the capacity of a system to maintain a desired state despite fluctuations in the behavior of its component parts or its environment. Robustness does not imply that the system must remain unchanged, but also describes the ability of the system to adapt and innovate in anticipation or in response to a disturbance. Hence, a robust system requires functional redundancy and feedback controls to compensate for changes in environment. A good analogy is an aircraft in flight. A robust flight does not deviate in altitude yet might adapt to changing environmental conditions by altering the angle of its wings while also having redundant systems so that a single engine failure does not prevent function. A large fluctuation in function is undesirable as it may be fatal for the passengers, and this is the main difference between robustness and vulnerability. Vulnerability can be kept low in a system that experiences large fluctuations in state (or, in our example, altitude) providing that it recovers quickly, but a robust system cannot tolerate a large fluctuation in state. Therefore, robustness is a key property that must be assessed when studying food webs in economical contexts, such as fisheries management, as the depletion of a series of

species within the ecosystem may have profound impact on the ecosystems populations and on the maintenance of the ecosystem itself. In food web ecology, robustness is used to quantify the change in network properties that result from a loss of individual or groups of species.

Understanding and predicting the robustness and vulnerability of complex ecological networks is a topic of increasing relevance. There is a general agreement among the network ecology community that nodes in certain critical network positions may have an area of effect that is greater than their neighborhood, thus having a much higher impact on network functioning. The loss of these key nodes may easily generate cascading effects in the network. This is particularly crucial in ecosystem management when assessing the importance of *keystone species*, species that has a disproportionately huge effect on the food web compared to their topological position and the direct neighbors in terms of consumptions (Mills and Doak, 1993). These species play a key role in maintaining the structure of an ecological community (Jordán, 2009). The removal of key species in a food web can compromise the whole system, breaking the balance between species consumption and creating irreversible damages (Cohn, 1998). The cascade of interactions among species are hard to predict since secondary effects depend on the architecture of the network. Thus, the issue is to relate the role of these groups of nodes to the overall architecture of the network, a question that remains open and has been widely addressed in the past few years (Gunderson; Jones et al., 1994; Jordán et al., 2005). Focusing research on these key nodes can be one way to tame and handle complexity (Jordán, 2009) and assess the relative importance of species in ecological communities (Mills and Doak, 1993; Paine, 1969; Power et al., 1996). Various network centrality measures at node levels were previously tested on food webs to quantify and identify

important network positions (Estrada, 2007; Jordán and Scheuring, 2004) and structural analyses (Allesina and Bodini, 2004; Jordán, 2009) are increasingly supported by dynamical studies (Jordán et al., 2008; Livi et al., 2011).

These latter suggest that key positions may not be identified only by local indices (like node degree). Other measures that considers the indirect neighborhood of nodes are needed to assess the importance of species in a food web. A number of experimental and modelling works (Brose et al., 2005; Menge, 1995) support the importance of indirect effects in biological systems. This justifies the search of other non-local mesoscale metrics that could explain the indirect effects better than the standard metrics and assess the overall role of groups of unconnected nodes within the network. Apart from expanding the neighborhood of focal nodes (increasing the distance for network effects), it has also been suggested that the number of local nodes may also be expanded from 1 to *n*. Group metric centralities such as key players and others (Borgatti, 2006; Borgatti et al., 2002), were applied in other fields of science, such as landscape ecology, to identify the importance of unconnected habitat patches spanning wide areas for bird migrations (Pereira and Jordán, 2017; Pereira et al., 2017). This approach suggests that the positional importance of network nodes may not be characterized independently, one by one, but rather simultaneously. The importance of mesoscale analyses to address ecosystem vulnerability was proven both empirically, with the discovery of keystone species complexes (Daily et al., 1993) and theoretically, by means of network modelling techniques in ecosystem management studies focusing on the consumption of fisheries (May et al., 1979). Recent attempts have been made to model and determine the identity of keystone species complexes in real ecosystems by network analysis (Ortiz et al., 2013, 2015, 2017). Although the predominant view on network robustness is focused on local

and single-node analyses (by modelling for example the degree distribution of food webs (Dunne et al., 2002)), little or no efforts were made to quantify group centrality effects that underlie the functioning of an ecosystem. Besides, key player sets of large size may perfectly or partly include the members of smaller ones, i.e., they may be nested to some extent. This property of key-player sets, called *nestedness*, has been already used to study the relationship between important species and network conservation (Benedek et al., 2007).

In this chapter we move from centrality metrics to the use of non-local, multi-node approach based on key players by means of Pyntacle. We have quantified the macroscopic (network-level) topological properties of 27 real food webs derived from marine ecology studies, calculated local centrality for each species and ranked species by importance accordingly, computed key-player centrality metrics using Pyntacle on increasing size and quantified the nestedness of these group of nodes, focusing on the correlation between nestedness and other topological network properties. We reasoned on the nestedness concept, and of its consequences on the efficiency and success of conservation efforts. We argue that large nestedness makes the network more predictable and manageable (Benedek et al., 2007), so our results may have implications to the efficiency of conservation efforts of terrestrial ecosystems.

2. Food Webs network analysis

The studied macroscopic network parameters are presented in Table 5. The smallest and the largest network, in terms of the number of nodes, were the *cat* (N = 48) and the *carpinteria* food web (N = 128), respectively. Depending on the various actual numbers

of links (*E*), density ranged from Δ = 0.06 (*aka a*, *cow17*, *martins*, *narr*, *troy*) to Δ = 0.16 (*demp su*). Average degree ranged from <*k*>= 4 (*aka b*, *cow17*, *narr*) to <*k*>= 18.72 (*carpinteria*). Diameter ranged from *D*= 4 (*black*, *cow17*, *german*, *healy*, *stony*) to D= 7 (*cow1*), and the average shortest path length ranged from <*SpL*>= 2.19 (*carpinteria*) to <*Sp*>= 2.9 (cow1). The average clustering coefficient ranged from *CC*= 0.02 (*cat*, *kyeb*, *sutton sp*, *sutton su*) to *CC* = 0.25 (*carpinteria*) and the weighted clustering coefficient ranged from CC_w= 0 (*broad*, *sutton sp*, *sutton su*) to CC_w= 0.25 (*carpinteria*).

Finally, to enrich the topological information, we measured the overall fragmentation status of each food web using the distance-based fragmentation (*dF*, see Materials and methods, section 2.5) (Table 5). The initial mean fragmentation value was 0,54, ranging from *dF* = 0.48 (*carpinteria*, *demp su*) to *dF* = 0.6 (*troy*). These findings show that food webs exhibit a high fragmentation (54%) and that, despite the short distances, the potential to stretch them is quite high.

Food web	*N*	*E*	*D*	*<k>*	*<SpL>*	Δ	*CC*	CC_w	*dF*
aka a	84	221	5	5.26	2.72	0.06	0.04	0.01	0.58
aka b	54	108	5	4.00	2.60	0.07	0.10	0.03	0.56
ber	77	232	5	6.03	2.63	0.08	0.03	0.01	0.57
black	85	366	4	8.61	2.45	0.10	0.04	0.03	0.53
broad	94	559	6	11.89	2.47	0.13	0.03	0.00	0.52
cat	48	107	5	4.46	2.42	0.09	0.02	0.01	0.53
cow1	58	118	7	4.07	2.90	0.07	0.11	0.06	0.59
cow17	71	142	4	4.00	2.73	0.06	0.15	0.04	0.59
demp au	83	410	6	9.88	2.47	0.12	0.03	0.01	0.53
demp sp	93	535	5	11.51	2.47	0.12	0.04	0.01	0.53
demp su	107	918	5	17.16	2.21	0.16	0.09	0.06	0.48
german	84	347	4	8.26	2.58	0.10	0.07	0.05	0.55
healy	95	603	4	12.69	2.30	0.13	0.07	0.03	0.50
kyeb	98	616	5	12.57	2.40	0.13	0.02	0.02	0.52
lilkye	78	372	5	9.54	2.49	0.12	0.07	0.02	0.53
martins	104	311	5	5.98	2.65	0.06	0.11	0.04	0.58
narr	71	142	5	4.00	2.55	0.06	0.07	0.02	0.57
north	78	228	5	5.85	2.54	0.07	0.12	0.04	0.55
powder	78	252	6	6.46	2.58	0.08	0.06	0.01	0.56
stony	112	824	4	14.71	2.35	0.13	0.07	0.02	0.51
sutton au	80	331	6	8.28	2.59	0.10	0.03	0.01	0.55
sutton sp	74	388	5	10.49	2.39	0.14	0.02	0.00	0.51
sutton su	86	417	5	9.70	2.34	0.11	0.02	0.00	0.51
troy	76	170	6	4.47	2.87	0.06	0.05	0.03	0.60
ven	65	184	5	5.66	2.57	0.09	0.06	0.03	0.56
carpinteria	128	1198	5	18.72	2.19	0.15	0.25	0.25	0.48
cant	108	693	5	12.83	2.37	0.12	0.04	0.01	0.52

Table 4: Overall properties of the 27 food webs: *N* = number of nodes; *E*=number of links, *D*=diameter, <*k*>= average degree, <*Sp*>=average shortest path, Δ=density, *CC*=average clustering coefficient, CC_w=weighted clustering coefficient, *dF*=distance-based fragmentation status.

3. Key player and nestedness analyses reveal common features in food webs

To understand whether key species were peculiar to specific food webs, and to reveal the underlying organization of food webs, we computed key-player sets of increasing sizes (1 to 4) for each key-player metric, both for fragmentation and reachability. Moreover, since the *m-reach* reachability metric requires the specification of a maximum distance length, we set m = 1 to 3. Results are shown in Figure 16A for all measures but reachability and Figure 16B for m-reach. The increase in size of the kp-set has dramatic consequences on most of the fragmentation metrics, showing a linear relationship between the increasing set size and the increase in fragmentation.

Moreover, two nodes resulted to be required to reach the majority of nodes in any of such networks with a maximum m-reach distance of 2 since a single node alone was not able to reach the whole network. This confirms that the study of groups of nodes are critical and more relevant than the study of single nodes in terms of reachability in heterogeneous food webs. Moreover, keystone species exert their functions in groups, reinforcing the idea that more than one keystone species is present in each ecosystem.

We then computed the nestedness between kp-set for each metric (Materials and Methods, section 2.3) and reported results in Table 5. We wondered whether food web topology has any significant effect on the nestedness of keystone species complexes in these 27 food webs. For this reason, we computed the Spearman correlation coefficient

(*P*) between 9 topological metrics that are strongly related to the topology and 6 measures of nestedness for each food web. Among the 6 topological indices, only 6 were significant (Figure 17), and in each of these, M2 was the nestedness index (*F*, *dF*, *dR*, M1 and M3 did not show any significant correlation). M2 correlated positively with *dF* and <*SpL*>, and negatively with **Λ** and <*k*> (*N*, *E*, d, *CC* and CC_w did not show any significant correlation). The four significant correlations are between M2 and *dF* (ρ = 0.681; p = 0.0009), M2 and **Λ** (ρ = -0.678; p = 0.001), M2 and <k> (ρ = -0.637; p = 0.00035) and M2 and <*SpL*> (ρ = 0.605; p = 0.00084). All of them are strongly significant. Only a few topological features can be used as a proxy for assessing the nestedness of central node sets, but most of these show quite strong correlations. Our results suggest that in networks where shortest paths are shorter, and density is higher, nestedness is lower, so systems-based conservation can be less predictive and efficient. One example is the Sutton tussock grassland in springtime (Figure 18A). Here, the single most central organism in the network is *Unidentifiable detritus* (#0, black in Figure 18A). The most central pair is the diatom *Cocconeis sp.* and the larvae of the riffle beetle *Hydora nitida* (#10 and #61, blue). The group of the three most central network positions are the red alga *Audouinella sp.*, the diatom *Navicula avenacea* and the caddisfly *Pycnocentrodes spp.* (#9, #30 and #70, red). The four most central organisms are the alga *Epithemia zebra*, the diatom *Eunotia spp.*, the fishfly *Archicauliodes diversus* and *Chironomid* type 'Diamesid Blond' (#18, #19, #49 and #52, orange). Hence, the increasing core of key organisms is perfectly unnested (M2 = 0, up to 4 groups). Accordingly, *dF* is low (0,51), **Λ** is high (0,14), <*k*> is high *F* (10,49) and <*SpL*> is small (2,39).

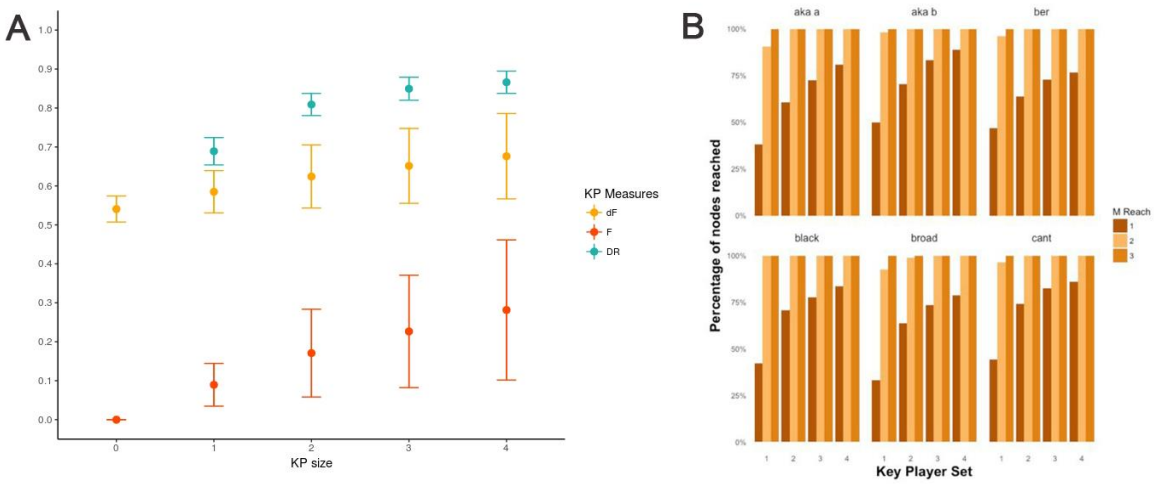

Figure 16: Fragmentation and reachability tendencies of food webs. A) Evolution of fragmentation metrics using *F* and *dF* and of *dR* reachability. B) m-reach tendencies for each m-reach distance value for node set of size 1 to 4 for a series of food webs. The majority of food webs (98%) are reached by 2 nodes in at most 2 hops.

Apart from the single-node core ($n = 1$), the larger cores ($n > 1$) are always composed of both plants (e.g. diatoms) and animals (e.g. caddisfly). On the contrary, in less connected and less compact networks, nestedness is higher, so a multi-species approaches fairly reinforce the results of single-species analyses. One example is the Dempsters tussock grassland in autumn (Figure 18B). Here, the single most central organism in the network is Unidentifiable *detritus* (#0, black). The most central pair is *Unidentifiable detritus* and *Terrestrial invertebrates* (#2, blue). The group of the three most central network positions are *Unidentifiable detritus*, and the caddisflies *Olinga feredayi* and *Tiphobiosis sp.* (#68

in orange and #76 in red). The four most central organisms are *Tiphobiosis sp.* as well as the alga *Epithemia zebra* (#18, yellow), another alga *Spirogyra sp.* (#37, yellow) and a mayfly *Nesameletus ornatus* (#66 yellow). Here, the composition of the core is a little bit more nested (M2 = 47,22) and, accordingly, dF is somewhat higher (0,53), **Λ** is lower (0,12), <*k*> is a little lower (9,88) and <*SpL*> is longer (2,47). The Supplementary material shows the nestedness patterns for each food web. The nestedness patterns for each kp-set iteration (data not shown) does not allow to compare the nestedness patterns for specific species in different food webs, limiting the search for keystone species. It must be noted, however, that node #0 is almost always *Unidentifiable detritus* (or some similarly large aggregated group, e.g. *Terrestrial invertebrate remains*), underpinning the importance of inorganic material for the development of ecosystems. In many networks, this is part of the key player complexes. Biologically speaking, this is an artefact: the detritus is clearly a well-connected component of food webs.

Food web	*F*	*dR*	*dF*	M1	M2	M3
aka a	100	100	80.56	100	77.78	0
aka b	100	100	94.44	91.67	77.78	0
ber	94.44	100	100	86.11	38.89	5.56
black	100	94.44	77.78	100	41.67	5.56
broad	100	100	94.44	61.11	5.56	0
cat	100	100	100	100	8.33	16.67
cow1	100	36.11	86.11	30.56	72.22	16.67
cow17	100	86.11	100	77.78	33.33	0
demp au	100	91.67	100	100	50	0
demp sp	100	100	55.56	100	72.22	0
demp su	50	100	27.78	100	47.22	0
german	100	69.44	72.22	63.89	8.33	0
healy	100	100	100	94.44	5.56	16.67
kyeb	100	100	100	94.44	27.78	0
lilkye	91.67	100	100	94.44	16.67	0
martins	100	47.22	83.33	66.67	22.22	0
narr	91.67	100	94.44	100	41.67	8.33
north	100	91.67	66.67	91.67	72.22	5.56
powder	100	100	94.44	100	77.78	0
stony	100	100	100	100	5.56	8.33
sutton au	100	61.11	91.67	77.78	38.89	0
sutton sp	100	100	86.11	100	16.67	8.33
sutton su	100	100	100	94.44	25	0
troy	100	100	100	100	0	8.33
ven	100	58.33	94.44	66.67	16.67	0
carpinteria	100	100	91.67	94.44	77.78	11.11
cant	94.44	100	100	100	41.67	0

Table 5: Nestedess computed for the kp-sets of sizes from 1 to 4 nodes for each of the key-player metrics. Kp-sets were found using the Pyntacle greedy optimization algorithm.

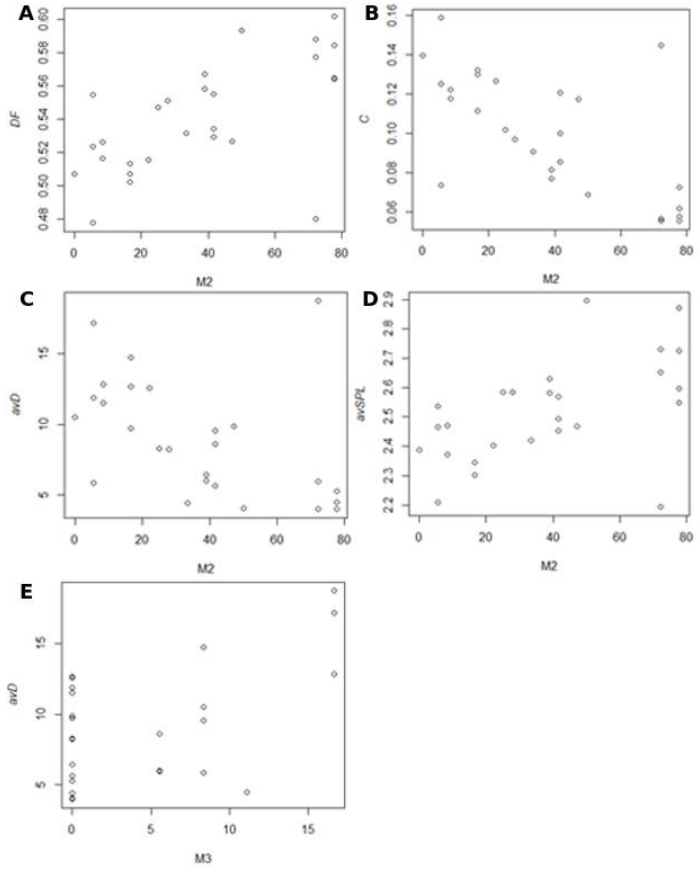

Figure 17: Correlations between nestedness values of m-reach metrics vs. topological features of the network. A-D: correlations between m-reach nestedness with a maximum distance length of 2 (M2) and distance-based fragmentation (A), density (B), average degree (C) and average shortest path length (D). E: correlation between nestedness computed for m-reach at a maximum distance of 3 (M3) and average degree.

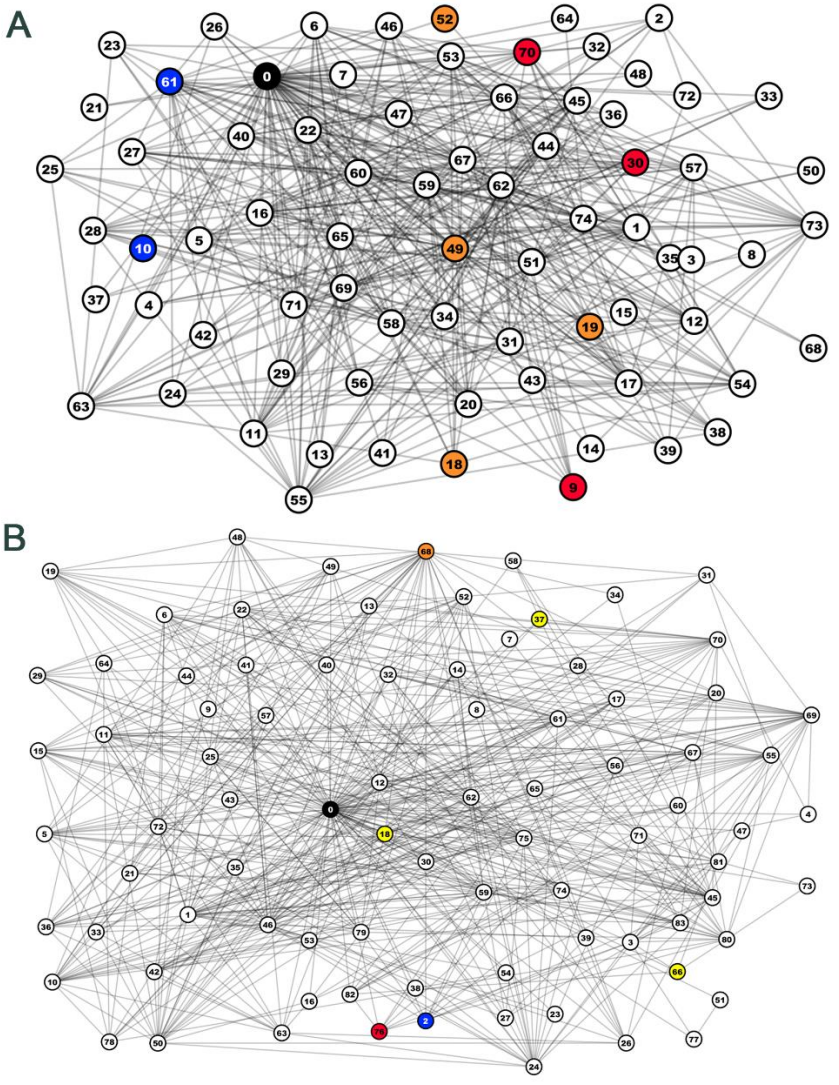
A
B

Figure 18: Network views of two food webs and the kp-sets found using the m-reach metrics. A) Sutton tussock grassland in spring (*sutton sp*) food web and the identified keystone species using m-reach group centrality metrics. In black the set of size 1, in blue the set with size 2, in red the set with size 3, in orange the set with size 4. B) Dempster tussock grassland in autumn (*demp au*) food web. In black the set made with size 1; the set with size 2 includes both the black and the blue sets; the set with size 3 includes the black set, the orange set and the red set. Finally, the set with size 4 *includes* the orange and the yellow sets.

It is worth noticing that *Unidentifiable detritus*, even if it is frequently the key-group with size 1, is frequently missing in larger key-player sets (e.g. for $n = 4$ in the *demp au* food web). So, even if it single-handedly dominates the network structure, its position is not significant anymore if we think in terms of a larger network core. Apart from the large aggregated groups typically being in the center of the network, the four organisms that can be in key position also in single-species cores ($n = 1$) are the diatom *Fragilaria vaucheriae* (#19 in the broad food web), the shore crab *Hemigrapsus oregonensis* (#45 in the *carpinteria* food web), the mayfly *Deleatidium spp.* (#34 in the *north* food web) and the diatom *Rhoicosphenia curvata* (#16 in the *powder* food web). *Hemigrapsus* appears in all of the four studied kp-sets in the *carpinteria* food web ($n = 1, 2, 3, 4$). Some communities are described by several versions of the food web (e.g. seasonal versions like *demp au*, *demp sp*, *demp su*). In some cases, these versions differ a lot in nestedness (*demp* and *sutton*), while in others there is only a small difference between the versions (*aka*, *cow*).

4. Conclusions

The dynamical behavior of complex ecological systems can be dominated by a few critically important components. Finding these could dramatically increase our understanding, the predictability of models and the efficiency of management efforts. We studied a comparable set of empirical food webs and identified the structurally most important *n* nodes in them. Whether or not these small sets were nested was correlated to some topological properties of these networks.

Network features influencing nestedness can be regarded as topological constraints on the predictability and efficiency of management and systems-based conservation. It remains unclear to us how can M2 and M3 be negatively and positively correlated with $<k>$, respectively. There is a need for a better understanding of the biology of the key-groups and the ecology of nested vs non-nested communities. If certain groups (e.g. zooplankton, diatoms) appear frequently in the core of food webs, these can be thought to be real keystone species. This is especially important if the core is nested: this means that the community is really dominated by a single species. We still know nothing about the kinds of communities (or the set of abiotic factors) that can be associated with nested patterns. Biologically speaking, this is the most promising future research line.

Our results are based on a set of 27 empirical food webs in the size range between 48 and 128 trophic groups. This is the typical size scale for food webs in the literature. All the webs were described by the same methodological standards, so they are comparable to each other. In order to see if these results are generalizable, research is needed in at least two directions. First, one wants to see if topological properties scale with network size.

For this, much larger networks should be studied – and the topological properties studied here can be more and more relevant and interesting for larger graphs. The limitation here is that empirical networks are not larger. Much larger networks (N>500) could be constructed by dramatically increasing the resolution of trophic groups (e.g. by adding bacteria and replacing trophic groups by biological species) but these networks would not be biologically comparable to the present ones (even if being mathematically more interesting). Second, toy networks of the same size ranges can be generated by various algorithms (i.e. by using the `pyntacle generate` command) and empirical topologies could be compared to the theoretical distributions. This kind of randomization analysis is fairly straightforward in community ecology; however, it is not easy to see which generative algorithms give the most realistic results as the nature of the current models available in the ecological community yield particular issues that must be addressed (W. Fox, 2006; Williams and Martinez, 2000). These studies could reveal if the reported relationships are universal properties of networks in general or they are specific to only food webs for some biological (ecological) reasons. If the results are food web-specific, we need to understand the biological reasons. If the results will be shown to be of general nature, conclusions can be drawn also in other fields of research. For example, terrorist networks have been shown to have large average shortest paths and low density (Krebs, 2002), properties suggesting that their efficient "management" is possible – in the context of homeland security. This work is of mostly conceptual and methodological nature. We suggest that the search for the cores of ecosystem networks opens several research lines that could massively contribute to systems-based conservation biology and management, with applications ranging from marine fisheries to pollination systems.

4. Characterization of sex-specific mechanisms of aging in correlation networks of adult Drosophila Melanogaster

1. Background

Aging is a natural process that occurs, continuously, through the entire individual's life. This process develops a progressive loss of physiological integrity, leading to impairment of vital functions, increased vulnerability and, finally, to death. This deterioration is the primary risk factor for major human pathologies, including diabetes, cardiovascular disorders, neurodegenerative diseases, and cancer. The identification of the markers of aging is one of the major challenges of biomedical research of the 21st century. One of the major hallmarks of aging was the discovery that the progress in aging is controlled, to some extent, by genetic pathways and biochemical processes that are evolutionarily conserved across complex multicellular organisms. The expansion of this field parallels that of cancer biology: the continuously increasing availability of molecular data in cancer research from the early 2000s onwards allowed to better understand the molecular mechanisms underlying cancer initiation and maintenance. This was possible by merging and studying together several kinds of data, from metabolomics to epigenetics (Fouad and Aanei, 2017; Hanahan and Weinberg, 2011). The current scientific consensus supports nine main hallmarks of physiological aging, which can be manipulated experimentally to accelerate aging or ameliorate the health span: genomic instability, telomere attrition, epigenetic alterations, loss of proteostasis, deregulated nutrient sensing, mitochondrial dysfunction, cellular senescence, stem cell exhaustion, and altered

intercellular communication (López-Otín et al., 2013). A major challenge is to dissect the interconnectedness between the candidate hallmarks and their relative contributions to aging, with the final goal of identifying pharmaceutical targets to improve human health during aging, with minimal side effects. Transcriptional changes are the core of these hallmarks since the reshaping of the transcriptome constantly models these processes. Changes in the expression levels and interactions of multiple gene networks occur in an aging multicellular organism. A major challenge is to understand which pathways and processes are altered and thus contribute to the manifestation of the hallmarks of aging. The overall balance of these events articulates at the organismal level into the integrative hallmarks to achieve the "aging phenotype" (Aunan et al., 2016).

A growing body of evidence (Frenk and Houseley, 2018; Kenyon, 2010; Seim et al., 2016) suggests that changes in the levels of expression of different genes reflect in changes in pathways which contribute to the manifestation of different hallmarks. These changes occur relatively early in life (Aunan et al., 2016; Bryois et al., 2017). In the past years, many studies have focused on describing the aging-related transcriptomic changes (da Costa et al., 2016; Doroszuk et al., 2012; Swindell, 2009). For technical and economic reasons, most studies on human (and vertebrate models) aging transcriptomics have focused on one or few cell types from single or few tissues (Boisvert et al., 2018; Haustead et al., 2016; Wood et al., 2013). Such conditions fail to underpin how each pathway contributes to the "aging phenotype" at the organism level. In order to overcome this difficulty, several studies in whole invertebrates have proven insightful. These

studies have mainly been conducted on *Drosophila melanogaster* in different times of development by means of the microarray technology (Girardot et al., 2006; McCarroll et al., 2004) (Zhan et al., 2007). Analysis of parts of the body of this organism as well as of the whole organism determined a large number of sex-specific transcripts downregulated during aging and a set of age-specific changes, correlating to a limited number of biological processes differentially expressed in the head or thorax of the fly (Carlson et al., 2015). Refinement of spatial-temporal expression of these results by Zhan et al. (Zhan et al., 2007), showed that gradual changes in different aging tissues have little overlap. However, these pioneering studies were performed using microarray platforms and did not explore sex-specificity that could have a reshaping effect on the aging phenotype. Currently, high-throughput RNA sequencing (RNA-Seq) allows for a higher sensitivity even for lowly expressed transcripts and a wide range of techniques that can be used to model the expression data according to the research aims. Among the landscape of possibilities, correlation networks have grown in popularity in the last few years as they enable the integration of large transcriptional datasets (Li et al., 2015; Liseron-Monfils and Ware, 2015). Co-expression network analysis allows the simultaneous identification, clustering, and exploration of thousands of genes with similar expression patterns across multiple conditions (co-expressed genes). Their use allowed for a better understanding of the functional dynamics of gene interplay, to the characterization of biological processes, and to the study of the expression dynamics of complex disease mechanisms (Emamjomeh et al., 2017). By means of gene correlation networks, it was possible to define modules of tightly knit of co-expressed genes and to identify peculiar gene

signatures related to clinical traits of the human prefrontal cortex of old human brains when compared to young ones (Hu et al., 2018). It was also possible to reveal aging-related gene/pathway and cross-tissue relationships that had been observed for a long time by physiologists without being validated at the molecular level (Huang et al., 2011). The human brain co-expression network, in particular, was the object of intense studies, as it was also possible to spot that schizophrenia and normal human aged brains show similar patterns of co-expression in the frontal cortex (Kim et al., 2018). These works, however, lack the characterization of the co-expression network communities that are embedded within aging tissues.

In the present study, we tried to extend the current knowledge of aging mechanisms in Drosophila and the techniques that are based on co-expression networks using the theory of graphs. Centrality indices and algorithms for the measurement of team-play effect of conserved genes in both sexes were used to assess their importance within the co-expression modules. We made use of publicly available RNA-Seq data (Graveley et al., 2011), to build co-expression networks for male and female flies using the Weighted Gene Clustering Network analysis (WGCNA) (Langfelder and Horvath, 2008) method. These networks were then compared. A list of genes that are important in the architecture of sex-specific modules was finally obtained. We studied the functional enrichment of sex-specific genes in female and male flies using the Gene Ontology. We then assessed the common genes between the paired overlap consensus and each sex-specific module. To assess their importance in the corresponding networks, we applied local and global

centrality indices on each sex-specific correlation network. This revealed several groups of genes that can be considered potential markers of the sex-specific aging process. This work is part of a broader analysis of sex and aging in fly and serves as a backbone to select candidate genes to be screened using other data wrangling techniques and *in vitro* assays.

2. Co-Expression analysis of sex-specific transcriptomes reveals different co-expression module hubs

In a first step, we sought to reconstruct stage-specific correlation modules of co-expression for male and female flies. Using the data from (Graveley et al., 2011), we run the Weighted Gene Co-expression Network Analysis (WGCNA) method on RNA-Seq data obtained on samples of of adult flies. The procedure for detecting these modules is described in Materials and Methods, section 5.2. This analysis allowed to retrieve 27 modules for male and 28 for female. The size and number of these showed a remarkable variance, both within the same sex and between genders. The majority of genes in males was clustered in 6 big modules, each containing more than 500 genes (*blue* cluster *N*=535, *brown N*=688, *brown2 N*=1264, *floral white N*=536, and *pale turquoise* N= 2280) (Figure 19, left panel). The network of co-expression in females was centered around two hub co-expression modules: *black* (*N*=2461) and *turquoise (N*=2280) (Figure 19, right panel). In both cases, half of the coding genes did not cluster together (56.6% for male and 50.6% for female). We then sought to analyze the interplay among these

modules. We summarized the overall expression values within modules using the module eigengenes (Materials and Methods, section 5.2). We assessed the relationships between the eigengenes by computing the correlation among summarized expression levels and by using hierarchical clustering to identify the groups of synchronized module eigengenes. This allowed calculating also the distance between modules. In males (Figure 20), we observed that the majority of hub module eigengenes exhibited positive correlations with other small hubs, except for *the brown2* and *pale turquoise* hubs that grouped together. In female (Figure 21), the *black* hub was separate from the other module eigengenes, while the *turquoise* module eigengenes aggregated with a series of smaller module eigengenes: *salmon4* (*N*=34), *darkorange2* (*N*=44) and *red* (*N*=215). This suggests that the *turquoise* hub may function as an aggregator of smaller functions, possibly leading to a hierarchical organization between *turquoise* and its neighbors.

To conclude the exploration of sex-specific modules, we performed gene set enrichment analysis (GSEA) on each module. The enriched functions were aggregated into macro functional categories by REVIGO (Supek et al., 2011). Treemaps for each module, depicting the most important biological processes (BPs) represented in each module, were created. Figure 22 shows the most notable example, which is the *bisque4* module (*N*=54) that has been characterized later in this chapters by means of network analysis: this module is represented by a plethora of BPs, which are summarized into two macro functional categories important for aging: the oxidative stress-related processes and the

metabolic functions. This reinforces the idea that the aging process is altogether sustained and fed by modules of co-expressing genes.

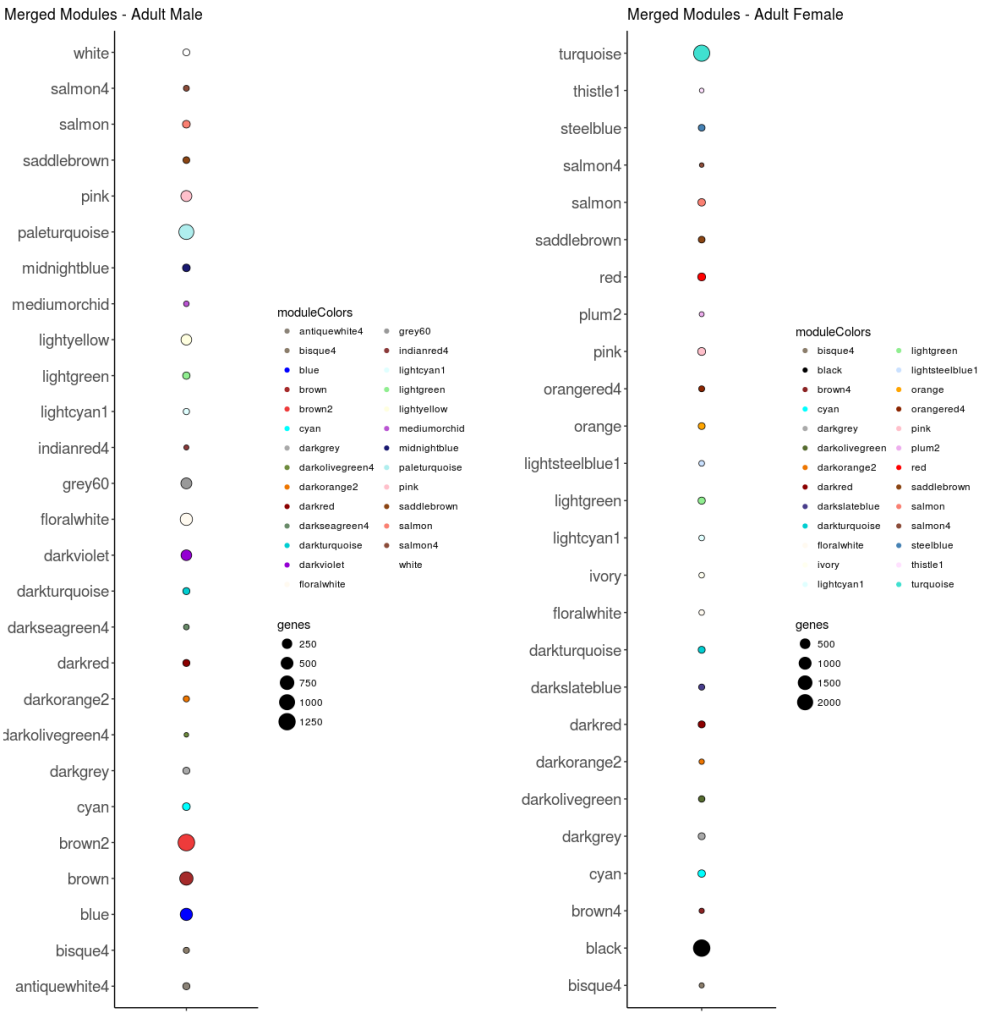

Figure 19: Bubble plots representing the modules and their sizes of co-expressing genes in the population of female (right) and male (left).

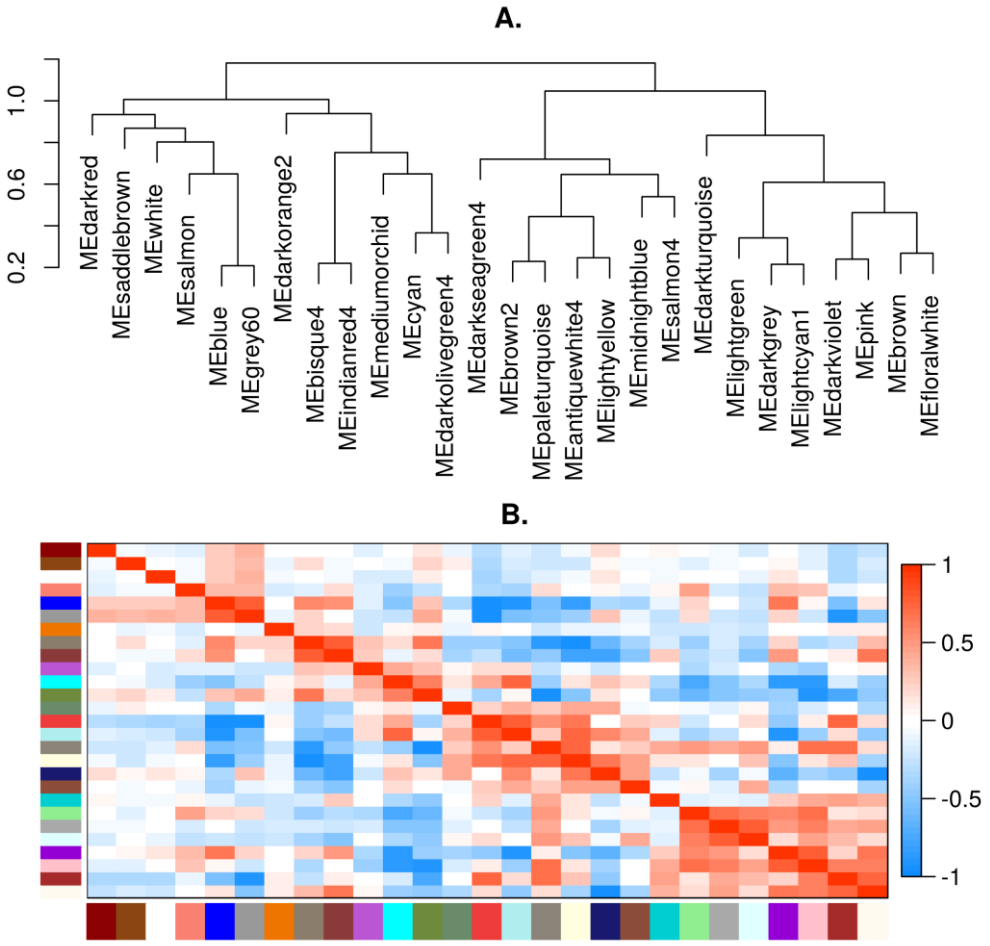

Figure 20: Clustering dendrogram (upper plot) that summarizes the eigengenes correlations (lower plot) in male co-expression networks.

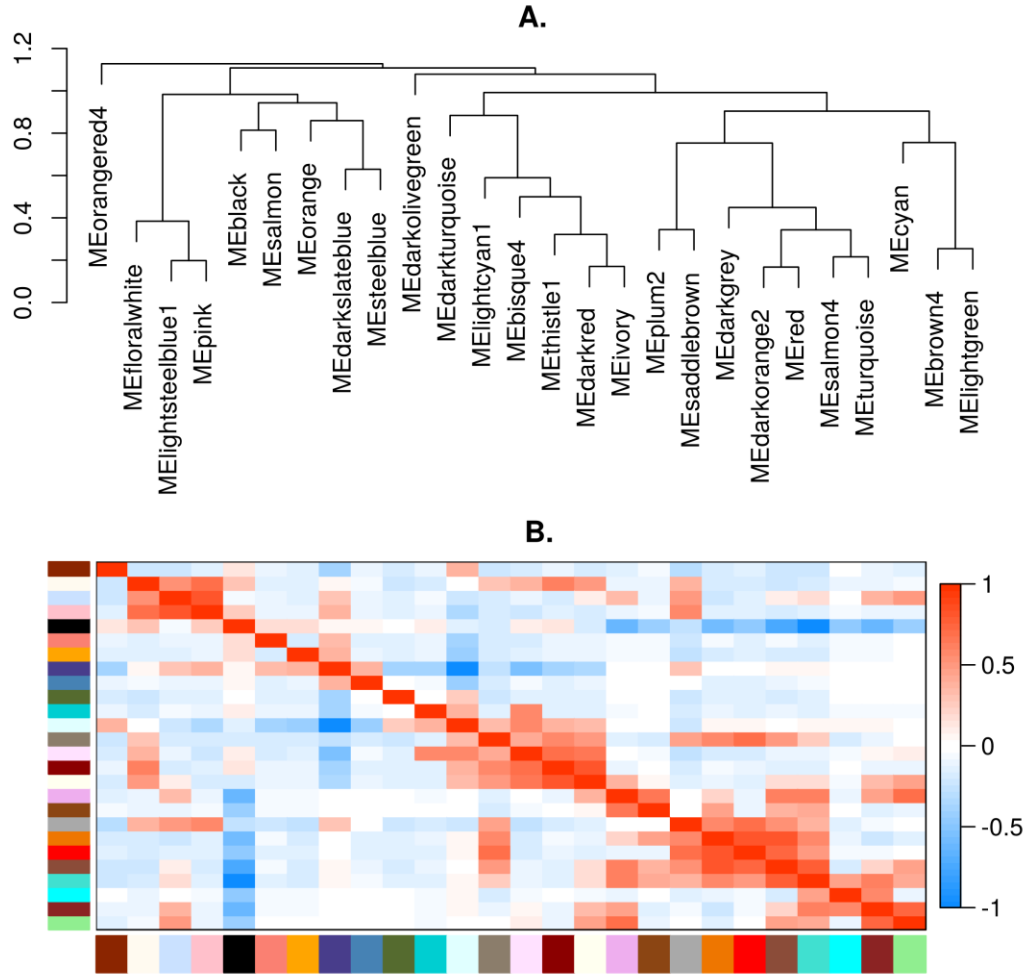

Figure 21: Clustering dendrogram (upper plot) that summarizes the eigengenes correlations (lower plot) in female co-expression networks.

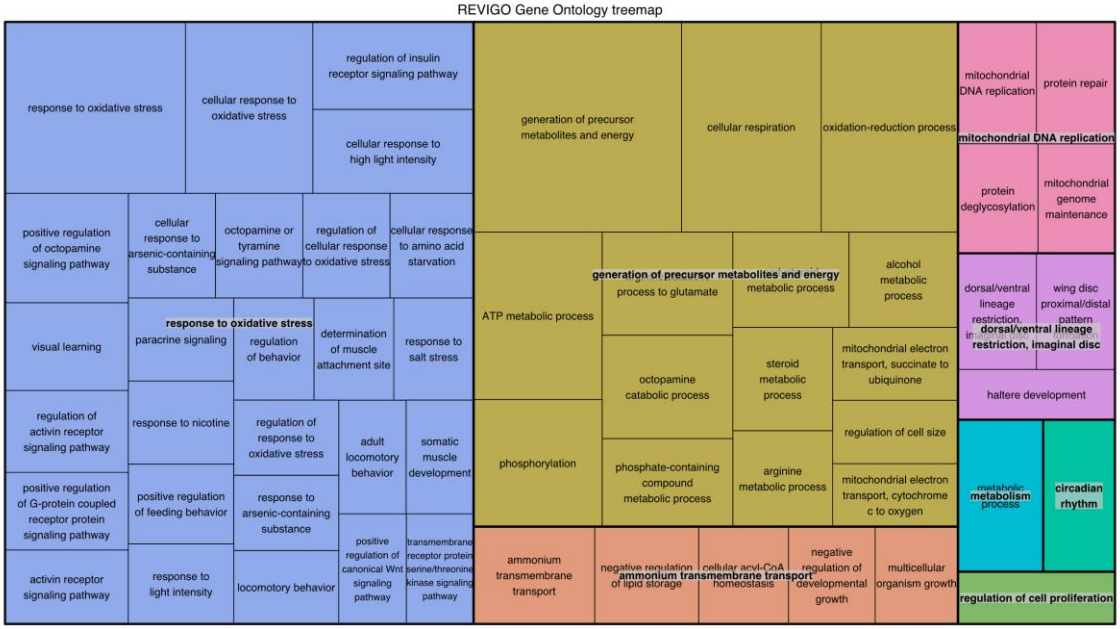

Figure 22: GO enrichment as summarized by REVIGO in a treemap showing the most important BPs for the *bisque4* co-expression module in the male flies. Aggregated processes have the same colors, and the aggregated GO processes are shown in bold in each group of tiles.

3. Network analysis of consensus overlap reveals common key-players in male and female co-expression modules in *Drosophila*

Gene co-expression networks constructed from *Drosophila* RNA-Seq data allowed to capture the relationships between genes. The built of the sex-specific functional modules bridged the gap between individual genes and emergent global properties of the interplay

among genes in the two genders. This variability may underlie a different contribution of genes in the establishment of different biological processes in aging. Some biological functions could be performed by the same genes, while others can be more associated to one sex than another. For this reason, we identified common mechanisms of co-expression by building a common co-expression network between both sexes in order to find consensus modules across the two genders (Langfelder and Horvath, 2007; Langfelder et al., 2013). A total of 18 co-expression consensus modules were found. These modules include genes that premusibly participate to common functional mechanisms among the two sexes. We measured the *preservation* index between the consensus network and the sex-specific networks, discovering that the sex-specific co-expression networks and the consensus network were moderately well-preserved (*preservation*=0.6), with a greater contribution on the consensus network of the male dataset than the female one (data not shown).

We then reasoned on the common features. First, we identified the common genes between each sex-specific module and selected only significant overlaps between each consensus/sex-specific module pair with a hypergeometric test (Figure 23, both matrices). Significant gene overlaps were then traced back to the original sex-specific modules and their orchestrated effects of each overlap were explored by measuring the *distance-based fragmentation* (*dF*) key-player measure before and after node removal. We found that, on overall, the removal of the overlaps had a double effect on the initial network fragmentation status. Removing some nodes resulted in an increase in

fragmentation, while removing other nodes resulted in a decreased fragmentation, suggesting that these last nodes might play peripheral roles in the network. We focused our attention on the *bisque4* male module, identified before. This small module, composed by 37 nodes and 358 edges, has a significant overlap with the magenta consensus module (n=16, $-log_{o\text{-}value}$=11), whose removal increased the overall module fragmentation by 10% (ΔdF=0.1), as shown in Figure 24, top panel. We then evaluated the overlap with the *turquoise* female module ($-log_p$=18) and found that its removal did not modify considerably the fragmentation status of the network, with a <0.2% increase ($\Delta dF<0.001$) (Figure 24, bottom panel). On overall, these findings suggest that consensus modules are able to spot key players selectively, pinpointing that sex-specific genes have different functional roles in aging according to the gender of flies.

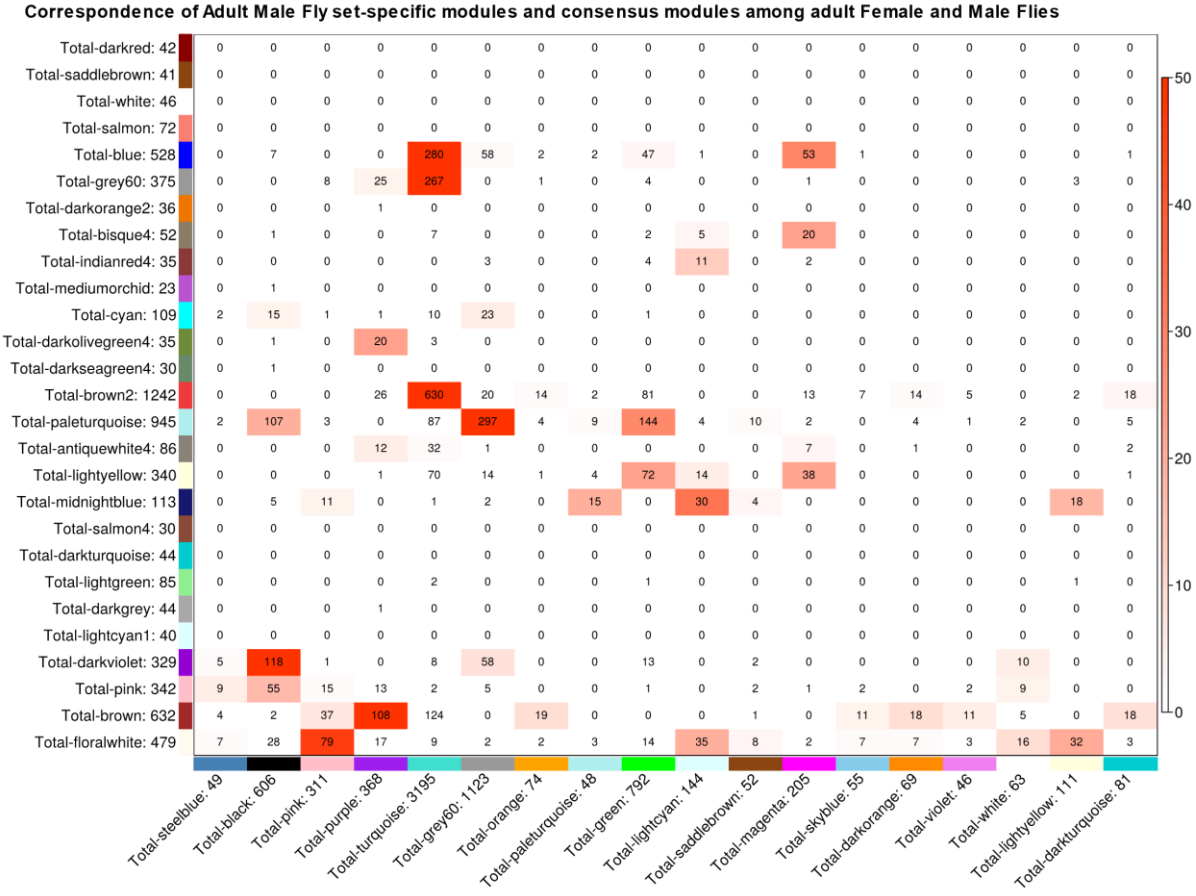
Correspondence of Adult Male Fly set-specific modules and consensus modules among adult Female and Male Flies
Total-darkred: 42
Total-saddlebrown: 41
Total-white: 46
Total-salmon: 72
Total-blue: 528
Total-grey60: 375
Total-darkorange2: 36
Total-bisque4: 52
Total-indianred4: 35
Total-mediumorchid: 23
Total-cyan: 109
Total-darkolivegreen4: 35
Total-darkseagreen4: 30
Total-brown2: 1242
Total-paleturquoise: 945
Total-antiquewhite4: 86
Total-lightyellow: 340
Total-midnightblue: 113
Total-salmon4: 30
Total-darkturquoise: 44
Total-lightgreen: 85
Total-darkgrey: 44
Total-lightcyan1: 40
Total-darkviolet: 329
Total-pink: 342
Total-brown: 632
Total-floralwhite: 479
Total-steelblue: 49
Total-black: 606
Total-pink: 311
Total-purple: 368
Total-turquoise: 3195
Total-grey60: 1123
Total-orange: 74
Total-paleturquoise: 48
Total-green: 792
Total-lightcyan: 144
Total-saddlebrown: 52
Total-magenta: 205
Total-skyblue: 55
Total-darkorange: 69
Total-violet: 46
Total-white: 63
Total-lightyellow: 111
Total-darkturquoise: 81
50
40
30
20
10
0

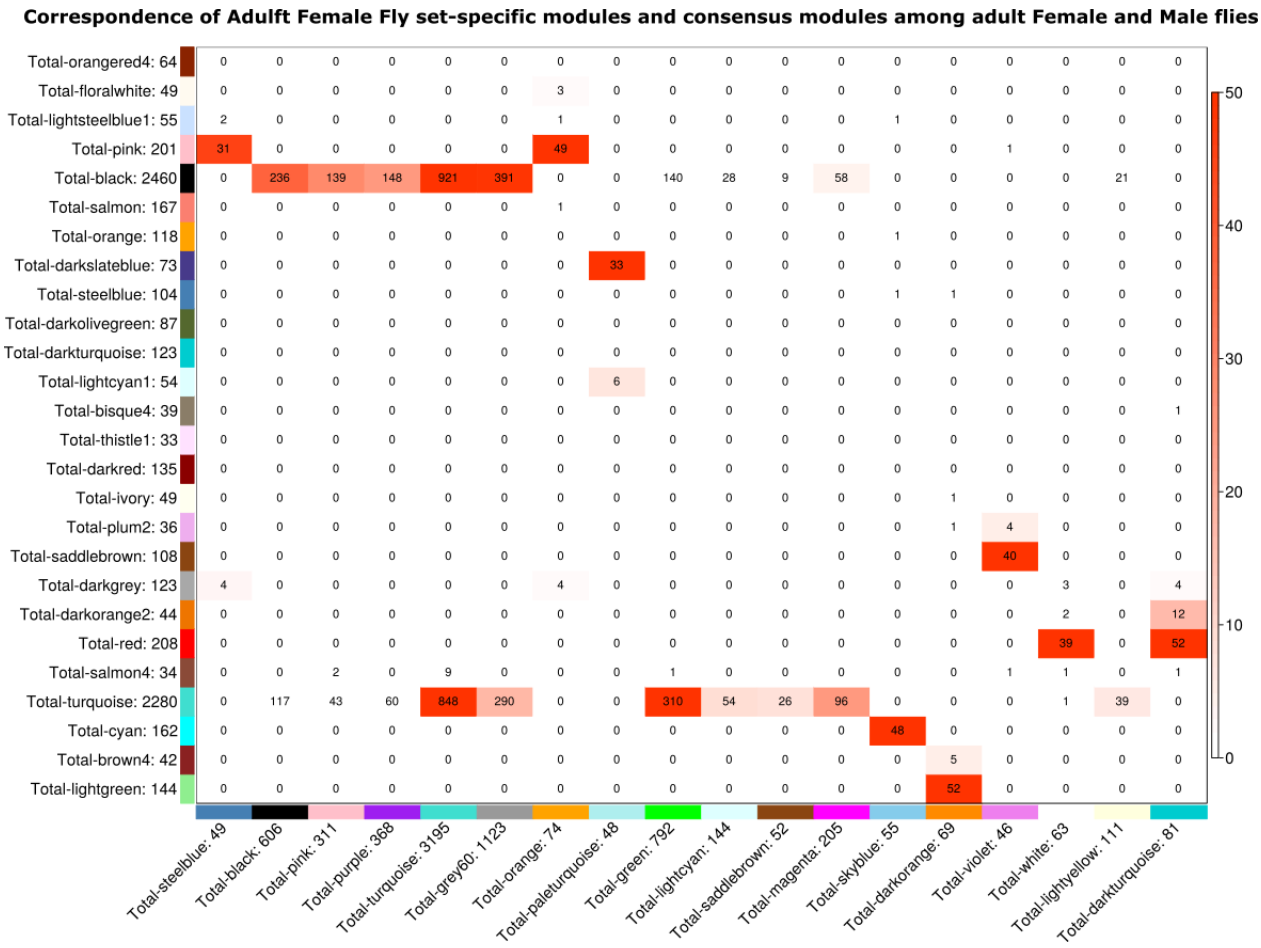

Figure 23: Number of overlapping genes between sex-specific (rows) and consensus co-expression modules (columns), for male (upper plot) and female (lower plot) flies. Numbers represent counts and the colors highlight the significance of the overlap between the two gender datasets.

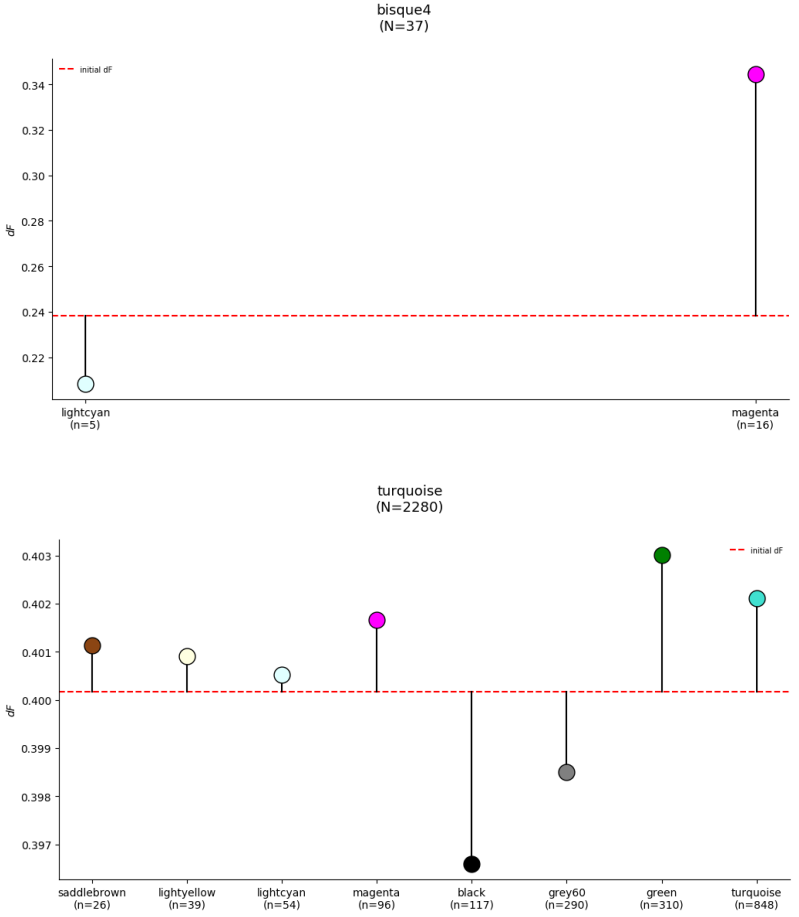

Figure 24: Distance-based fragmentation measured for the male bisque4 co-expression module (top) and the female turquoise co-expression module (bottom) before and after overlaps removal. Dotted red line shows the the initial fragmentation value. Point colors represent the consensus module from which the overlap has been derived.

4. Conclusions

The aging phenotype is not the consequence of a single gene malfunctioning, but of the constant, concerted, transcriptome-wide modification of gene abundances over the lifespan on an adult individual (Harris et al., 2017). The relationship between sex and aging has been object of intense researches over the past few years (Berghella et al., 2014; Harris et al., 2017; Kamei et al., 2018). Multicellular model organisms provide an ideal benchmark on which to study the dynamics of aging, and the small fly *Drosophila melanogaster* is a key organism to characterize aging processes due to its short lifespan and its low maintenance cost (Girardot et al., 2006); the search for molecular determinant of aging is already begun. In this study, we provided an analytic blueprint for the exploration of the relationships between sex and gender in the fly. We used publicly available adult fly RNA-Seq data and showed that modules of correlation networks strongly differ from adult and female flies in size and composition. A vast portion (over 50%) of the Drosophila correlation networks is scattered, and not connected enough to trace their origin to a single co-expression module. These preliminary data suggest that a consistent part of the transcriptome of female and male flies does not depend on tight mechanisms of co-expression for determining their regulation. Moreover, males exhibit a more homogeneous distribution of genes within modules, with a series of medium-sized hubs that are supported by small hubs, each devoted to its functional, cellular tasks. We hypothesize that the failure (or removal) of one of these hubs may not bring major perturbation to the overall co-expression network architecture, because of the distributed

load of biological processes that is compensated by other co-expression modules. Female co-expression modules, on the other hand, lack this homogeneity and are completely summarized by their two giant hubs. While this modular configuration makes the removal of one of them critical for the overall co-expression network, this should occur unlikely by simply removing sets of genes. Moreover, since the majority of biological processes are exerted by genes clustered in these modules, the female flies are more subjected than males to bear the consequences of the aging process. Then, to assess if part of each sex-specific network organization was shared across different modules, we built a consensus correlation network and used it to derive the consensus modules This analysis showed that the two genders contribute differently to all the correlation network modules. While a weak *preservation* value was found among the consensus module and its sex-specific counterpart, the consensus between the two transcriptomes was marginal, with genes of a sex-specific module spread over many other consensus modules in the opposite gender counterpart. The different gene distribution can have dramatic effects on the overall architecture of the two co-expression transcriptomes. This dissimilarity was found also at the module level. In fact, common genes among two different co-expression modules may have different topological importance, thus not contributing equally to their corresponding networks of origin. This concept pointed us to characterize the common genes in the consensus modules and their counterpart, to assess their topological importance. Group centrality metrics such as the key-players were ideal candidates to explore this contribution to the consensus network since they could measure the team-play effect that these genes exhibit in their network niche altogether. We focused on the

overlap between *bisque4*, a small module of the male fly found relevant in the oxidative stress and the metabolic processes and the *turquoise* female co-expression hub, a giant subcomponent of the female co-expression network. We found that the contribution to the overall fragmentation of the network is higher when removing the overlapped genes than its female counterpart, a clear index of how the organization of the communities within each co-expression network differs greatly, with a higher degree of conservation in the *turquoise* female network. All in all, these data point to different mechanisms of aging between genders in fly.

Discussion

With the increased availability of biological data, Biology is questioning its roots. *High-throughput techniques*, coupled with novel massive scale assays and computer science advancements are producing data faster than what researchers take to analyze them and yielding results. Data regard each layer of the *omics* world, from genomics to epigenomics. They make increasingly more sense if considered together, namely if shifting from the classical *reductionist* approach, that focus on the individual molecules, to the *holistic* view, which considers, instead, the whole system of molecules taken together. Besides its roots dates much earlier than these couple of decades, Systems Biology is the ideal framework to make this transition possible (Westerhoff and Palsson, 2004). The field takes from the reductionist approach to overlap a holistic approach, thus studying how a system is made and the relationships among its components.

The knowledge of how a system is shaped is crucial. Its particular *form* has direct consequences on the observed phenomena of interest. It has been proven, in fact, that the geometrical organization of a system, also known as topology, tightly characterizes the dynamical behaviors of the system itself. This is particularly important in the context of molecular biology, where changes between the patterns of interaction between genes or their protein products can have dramatic consequences on the system itself (Cho et al., 2016). Moreover, by predicting the functioning of a system, a systems biologist can

foresee which perturbations might lead to a new or altered phenotype (Cho et al., 2016). Networks, which are simple mathematical abstractions that model the interactions among components of a system, are at the core of Systems Biology. By means of Graph Theory, we are able to spot network features using a wide range of mathematical metrics, which study the centrality, namely the importance, of single entities with respect to the system's functional behavior.

This work aimed at exploring the potential of Network Biology in different biological areas of research. We first used widely known centrality indices to study the *regulome* of miRNAs, short non-coding sequences that modulate gene expression in colorectal cancer. By first identifying differentially expressed genes between CRC specimens and their matched normal tissues, we reconstructed the *interactome* of deregulated proteins in this disease. We then performed an integrative analysis of mRNA–miRNA and miRNA–miRNA interactions and identified two *cancer-protection* and nine *cancer-favorable* modules of genes, providing interesting evidence on mRNA–miRNA crosstalks in CRC. The analysis of the miRNA regulome also allowed to derive a series of miRNAs, chosen through a core-set of local topological centrality indices, that controlled important key genes in the process of CRC development. These resulted to be controlled, in turn, by the deregulated expression of miR-145, which we defined a master regulator of the small non-coding transcriptome and, hence, of some critical biological functions involved in the carcinogenesis.

The aforementioned node indices, e.g. *degree* and *betweenness*, are well-known in molecular network analysis and are widely used for tackling the most basic problems in network analysis. However, the landscape of centrality indices is large, as networks are used as a reasoning framework in several scientific disciplines, from Social Sciences to Ecology. These indices are not necessarily local or global in nature but can account for other levels of detail. For example, one could reason on the team-play effects of a group of nodes in a network, and their overall contributions to the topology and the information flow within it, rather than sticking to classical centrality indices. These classes of metrics, mostly unexplored by the molecular network community, can be crucial to pinpoint the role of groups of nodes in a network. For example, it is common knowledge that, even if a gene exhibit an extraordinary pleiotropic character, pathways and processes are rarely deregulated (activated or silenced) by a single gene perturbation (El-Brolosy and Stainier, 2017; Xu et al., 2009). The perturbation of a group of genes can instead have major effects on the same network, thereby deranging the cell's normal state.

Group centrality metrics enable to screen and evaluate for these types of dynamics. In line with these arguments, we introduced Pyntacle, a Python 3 library and a command line cross-platform tool for the exploration and search of groups of nodes, also known as *key-players*, that can potentially affect the fragmentation on the network, when removed, or that can be used as proxies to quickly reach the boundaries of a network. Pyntacle was equipped with the most disparate tools and algorithms for local and global topological studies, in order to make a swiss knife tool for network analysis.

We made huge efforts to make Pyntacle available through different channels. A website was provided (http://pyntacle.css-mendel.it) with extensive documentation and case studies. To boost Pyntacle performances, we equipped it with a series of algorithms that execute algorithms efficiently both on individual CPU processors, as well as in parallel on multicore processors and on CUDA cores of HPC graphics card, NVIDIA-enabled. To test the ability of Pyntacle to spot key-nodes, we compared Pyntacle performance versus those of a R library, *keyplayer*, which similarly performs group centrality analysis. Pyntacle outperforms this library by several orders of magnitude and is able to spot key-players even with large graphs, as well as with the interactome of small multicellular eukaryotic organisms, such as the one of the small nematode *C. elegans*. Pyntacle is actively maintained and reviewed and future plans include the extension of its functionalities with novel topological indices, which are used in Ecology and Social Sciences, and the improvement of its performance, allowing it to search and find key-players through the greatest biological network known to date: the human interactome (~20000 coding proteins).

We tested the usefulness of Pyntacle in two studies, presented in this work. The first one, to date in press, is a methodological study in the area of Network Ecology. In this work, we explored the role of key-players in a series of food webs, binary graphs that depict trophic relationships among species in an ecosystem. Key-players of different sizes were computed for each of the group centrality metrics available in Pyntacle, and a measure of *nestedness*, a probability that a smaller set of size *k* is included in a bigger one *j*, was

measured. Through nestedness linked to a reachability measure (i.e., m-reach of distance 2), we found a positive correlation between the average degree of $<k>$ of food webs and reachability, a feature more relevant in tightly connected networks than in sparse graphs. Network features correlated with nestedness can be regarded as topological constraints on the predictability and efficiency of management and systems-based conservation, hence providing a series of insights useful to decide which species to take into consideration, a task that is of increasing importance considering the current warnings on the climate changes and ecosystems deterioration.

The second study is instead a classic example of network analysis to infer structural properties of molecular networks. This work, currently ongoing, is part of a more general effort to identify the role of sex in the aging process in a model organism, the fly *Drosophila melanogaster*. In this work, we reconstructed the co-expression network architecture of adult female and male fly specimens using publicly available RNA-Seq data measured along the developmental stages of the male and female flies. These networks were built by means of the Weighted Gene Clustering Network Analysis, a computation tool that allows building a series of gene-to-gene relationships by means of fine-tuned measures of signed weighted correlations, other than raw correlation coefficients. It also allows the detection of modules of co-expression, communities of tightly linked nodes that exhibit strong inter-correlations. This first step of analysis concluded that half of the coding and non-coding transcriptome of the fly is located outside the identified communities, pointing to them as candidates for being object of

regulation by other means other than co-expression. The genes belonging to the communities, on the other hand, were differently distributed through the two stages, showing that the underlying architecture of the two genders is variable to some extent. This is expected, as during adulthood, female and male flies perform reproduction, hence their overall transcriptome abundance may exhibit different properties that require a reshaping of these connections. Sex-specific gene set enrichment analysis allowed us to identify a series of sex-specific co-expression modules that could be linked to the aging processes to assess similarities between co-expression modules. We reconstructed the consensus co-expression networks of the two genders and compared them with the two co-expression networks of the two stages. This analysis showed that common co-expression modules are weakly correlated to the sex-specific ones, reinforcing our idea according to which the transcriptomes vary based on the genders. We then computed the overlaps between each sex-specific modules of co-expression and their consensus counterparts and found that these genes had a different effect on the fragmentation of the sex-specific modules of origin. These findings would have not been possible without Pyntacle, that was also used to perform a series of ancillary operations (not reported here) to study the topology of these co-expression modules.

We showed the power of network models in biological studies. This opens new horizons for the analysis of complex molecular networks using non-trivial mathematics. This will help making new discoveries, thereby allowing to unravel the complexity of life, one index at a time.

1. Network analysis reveals RNA-RNA crosstalk and highlights the role of societies of microRNAs in human colorectal cancer

1. Data sources

The datasets analyzed in this study consists of the transcriptome and miRNAome (Piepoli et al., 2012) of a set of 14 matched pairs of tumor and adjacent non-tumorous mucosa samples obtained from colorectal cancer (CRC) patients and evaluated with the GeneChip Human Exon 1.0 ST array and GeneChip miRNA 2.0 array (Affymetrix, Santa Clara, CA, USA). Raw data are available in the ArrayExpress platform with ID: E-MTAB-829 and E-MTAB-752.

2. Statistical analyses

Expression data analyses were performed using GNU R ver. 3.0.2 (http://www.r-project.org) and the Partek Genomics Suite ver. 6.6 (Partek, St. Louis, MO, USA). Low-level analysis and normalization were performed using GCRMA (Wu et al., 2005) and Partek. We evaluated the probeset intensity values and kept only those significantly detected in at least six samples. To reduce noise, we also removed the probesets that do not map to an Entrez gene. Batch effects were removed by the Partek's batch effect removal algorithm. The resulting genes and miRs were tested for differential expression,

using the paired t-statistics. Under the assumption of equal variance between groups, allowing a number of false positives equals to 2% of the genome and setting the minimum log2 fold change (log2 FC) expression barriers to ±1.5, we achieved a statistical power of 0.8. Correlations between miRNA expression values were estimated using the Spearman's rank correlation coefficient (r_s) using Rcmdr (Fox, 2005). The relationships between miR-145 and its direct and indirect partners were ascertained by regression analysis. Time-to-event analysis was performed by the Mantel-Haenszel test and the 50% percentiles of miRNAs were used to dichotomize patients into low and high expression groups. Kaplan–Meier curves were drawn for CRC patients taken from The Cancer Genome Atlas (TCGA) dataset (https://tcga-data.nci.nih.gov/tcga/tcgaHome2.jsp). A p-value <0.05 was considered statistically significant. Equality of proportion was assessed by the Chi-squared test.

3. Gene selection strategy and *in silico* functional and pathway analyses

To make results more reliable, only differentially expressed genes deregulated in at least five CRC-related experiments retrieved from Gene Expression Atlas (Kapushesky et al., 2012) were selected. These underwent functional enrichment analysis against the Gene Ontology FAT subset and the set of genes with probe sets included in the used Affymetrix chips. Results obtained with DAVID (Huang et al., 2009) web services were cross-checked with Babelomics (Medina et al., 2010) and considered for inclusion if Bonferroni-corrected significance levels did not exceed 5%. General functional classes were refined by a mixture test between the *elim* and *weight* algorithms (Alexa et al., 2006). These determined the best enrichment in a bottom-up order, by progressively

removing genes from functional classes, which were enriched by more specific categories. This analytical procedure facilitated the identification of specific cancer-favorable and cancer-protection processes, with statistical confidence. Pathways were detected by ToppGene (Chen et al., 2009a), where the hypergeometric distribution with False Discovery Rate (FDR) correction was used as the standard method for determining statistical significance. The *P*-value cut-off was set to 0.05, while the *gene limits* ranged from 1 to 1500

4. MiRNA selection strategy

We obtained a list of miRs that were reliably associated with CRC by intersecting the set of miRs reported by miRSystem (Lu et al., 2012) to target the genes selected in the previous analytical steps with that of miRs associated to CRC, according to the Human microRNA disease Database (HMDD) (Li et al., 2014). MiRSystem is a database that integrates seven well-known target gene prediction programs: DIANA, miRanda, miRBridge, PicTar, PITA, rna22 and TargetScan. The observed identification probability (*O*) for a given gene is the proportion of the queried miRNAs predicted to target that gene, whereas the expected probability (*E*) is the proportion of all miRNAs in the miRSystem database predicted to target that gene, i.e. the number of target gene-miRNA pairs deposited in the miRSystem database. This expected probability represents the chance of one gene being randomly selected by miRNAs. We only considered experimentally validated targets, with an *O/E* ratio greater than 1.5.

5. Networks construction

We obtained multigraphs connecting genes by querying a number of heterogeneous data sources: (i) Interpro and PFAM, (ii) Gene Expression Omnibus, (iii) BIOGRID and IREF, (iv) PathwayCommons, IMID, NCI-NATURE, REACTOME, KEGG, BIOCARTA and (v) BIOGRID, BIND, HPRD, INTACT, MINT, MPPI, OPHID, through GeneMANIA (Mostafavi et al., 2008). We linked any two genes by an undirected edge, whenever an evidence of interaction was found, which we weighted with a value provided by GeneMANIA that indicates the predictive power of the selected dataset for that edge. Several pairs of genes could be connected by more than one edge. In such a case, we agglomerated the weights of multiple edges by the injective function:

$$W_{AB} = \sum_{i=1}^{n} W_{AB_i}$$

where n is the number of edges connecting any two nodes A and B, and i refers to the i_{th} edge. W_{ABi} stands for the weight of the i_{th} edge. The multiplicative factor $\frac{e^n}{n}$ is meant to give increasing importance to multiple links in respect to isolated links (Mazzoccoli et al., 2013). We then built weighted graphs with weights over the edges (carrying the reliability of the corresponding interactions).

MiRNAs were given in input to Ingenuity Pathway Analysis (IPA), which wired a network based on the Ingenuity Pathways Knowledge Base. This knowledge base has been abstracted into a large network, called the Global Molecular Network, composed of thousands of molecules that interact with each other. Two molecules (miRNAs and genes

here) are connected if there is a path in the network between them. Interactions can be physical and functional. We considered only physical interactions and cancer-related functions, to build a *literature-based* network. Dashed edges stand for indirect relationships between molecules, i.e. they summarize paths longer than one step.

The same set of miRNAs was filtered to contain only those that were differentially expressed between our CRC and control tissues as well as those that exhibited any significant correlation of expression with at least another miRNA (P-value < 0.05, $r_s > 0.4$ or $r_s < -0.4$). The resulting miRNAs were linked with non-oriented edges, since correlation is a symmetric measure, and weighted using the Spearman's rank correlation coefficient (r_s), to make an experimental network (Piepoli et al., 2012)

6. Topological network analysis

Genes and miRNAs were assigned a topological importance. All the considered metrics were based on the enumeration of links (or shortest paths). Considering a path from $s \in V$ to $t \in V$, with V the set of nodes, as an alternating sequence of nodes and edges beginning with s and ending with *t*, such that each edge connects its preceding with its succeeding node, we calculated the length of a path by summing the inverse weights of its edges. The idea is that highly correlated miRNAs or functionally closest genes minimize their distance. We calculated *degree*, *betweenness*, *closeness*, *radiality*, and *clustering coefficient* centrality indices, as described below, and ranked miRNAs and genes accordingly. The privileged topological position of miRs was inferred by a combination of the IPA's tools: BioProfiler and Upstream Regulatory Analysis. These

allowed inferring both which molecule might be considered causally relevant. Activation z-scores were conservatively kept to a minimum of ±2. Networks were drawn by Cytoscape 3.0 (Shannon et al., 2003).

7. Strongly connected components

Functional affinities of genes and miRNAs were sought among highly cohesive groups of genes and miRNAs. To this end, we used the ClusterONE algorithm (Nepusz et al., 2012). It handles weighted graphs and generates overlapping clusters. It starts from a single node and greedily adds or removes new nodes if they alter the cohesiveness of the group. Subgroups of less than five nodes or having a density less than a given threshold (set at 3) were discarded. Finally, redundant cohesive subgroups were merged to form larger subgroups to make the results easier to interpret.

8. MiRNAome and MAPK signaling pathway profiling after miR-145 transfection in CRC cell lines

To identify any functional synergistic pairs of miRNAs, the global miRNA expression profile was obtained in the transfected CRC cell lines, as previously reported (Piepoli et al., 2012) (ArrayExpress ID: E-MTAB-2704). Briefly, CaCo2, SW480, HCT116, and HT-29 cell lines were transiently transfected using HiPerfect Transfection Reagent (QIAGEN), with synthetic miR-145 mimic (MSY0000437, QIAGEN), following the manufacturer's instructions, as previously described (Panza et al., 2014). The total RNA

was purified using the RNeasy kit (QIAGEN) and labeled using the 3DNA Array Detection FlashTagTM RNA Labeling Kit (www.genisphere.com). Samples were hybridized on Gene-Chip miRNA Array (www.affymetrix.com), washed and scanned with an Affymetrix Scanner. MiRNA expression data were then processed and analyzed using the Robust Multi-array Average algorithm and deposited in the EMBL-EBI ArrayExpress.

To assess the effect exerted by miR-145 on the MAPK signaling pathway, gene expression levels of the transfected cell lines were quantified by using RT2 MAP Kinase Signaling Pathway PCR Arrays (SABiosciences). Briefly, mRNA and cDNA were prepared using reagents and equipment from QIAGEN (QIAGEN Hamburg, Germany) and assayed with the RT2 MAP Kinase Signaling Pathway PCR Arrays (SABiosciences) with SABiosciences RT2 qPCR Master Mix according to the manufacturer's instructions. Plates were read on 7900 TaqMan (Applied BioSystem, Life Technologies Corporation) with 1 cycle of 10 min at 95°C followed by 45 cycles of 15 s at 95°C and 1 min at 60°C. SYBR Green fluorescence was monitored at the annealing step of each cycle and analyzed with SDS v.2.4 software (Applied BioSystem, Life Technologies Corporation). The analysis of the gene expression was completed using the SA Biosciences PCR Array Data Analysis Web Portal, as recommended by the manufacturer, and verified using the ΔΔCt method.

2. Pyntacle

Pyntacle is a multifaceted library designed for Python 3.5 version onwards. The package has been tested for all the subsequent Python 3 versions including the latest Python release (3.7). Pyntacle is designed to be both a Python library and a command line tool. The command line interface is more straightforward. It is designed to run automatically the majority of Pyntacle functionalities and is addressed to the user with limited programming knowledge. On the other hand, the Python 3 code library is highly customizable and allows to fine-tune a variety of operations. It targets the experienced Python users that perform bioinformatic tasks on a daily basis and would like to add Pyntacle to their custom scripts or to their automated pipelines. For users with basic programming skills that would still like to use Pyntacle in conjunction with their scripts and code, we provided a utility, called `octopus`, that wraps many of the Pyntacle functionalities to finally make them easily approachable.

Other than providing a series of classical centrality metrics to topologically analyze a network, Pyntacle implements a few algorithms for the discovery of important groups of nodes, or *key players*. Moreover, Pyntacle is optimized to perform a series of ancillary operations, such as set operations between graphs, community finding, and file format conversion. We provide the hereafter a detailed overview of the most prominent functionalities, along with some supplementary materials (guides and network specifications) described in Appendix. The same material, along with a complete documentation, is available on our website (http://pyntacle.css-mendel.it) as a series of Jupyter Notebooks.

1. Technical specifications

All classes and methods in Pyntacle are arranged in a directory-tree like fashion (Figure 25). This organization helps to compartmentalize each functionality, to quickly debug and control the soundness of the code and to ensure that new functionalities can be added without the risk of breaking the whole package.

We built Pyntacle around the *igraph* package (Csárdi and Nepusz, 2006), a widely known cross-platform library for network analysis. The `igraph.Graph` object, is the very heart of Pyntacle, as it allows to store and manage huge graphs. Wùith igraph, we were able to store networks as big as the PPI network of *Homo sapiens*, stored in APID (Prieto and De Las Rivas, 2006), encompassing ~15000 nodes and ~175000 edges. Moreover, igraph allows enriching nodes, edges, and the whole graph with attributes, which are implemented as unordered collections of `keys:values`. Pyntacle reserves a set of private attributes, which are listed and described in Appendix 2 – Minimum Graph Requirements. While the `igraph.Graph` object allows to represent any type of network, the currecnt version of Pyntacle works with *simple graphs* only. Moreover, to avoid ambiguities, nodes are required to have a unique name (stored by default in the `name` attribute). For the same reason, multigraphs, namely networks with more than one edge connecting two nodes, are not supported, as edges are identified by the nodes they connect.

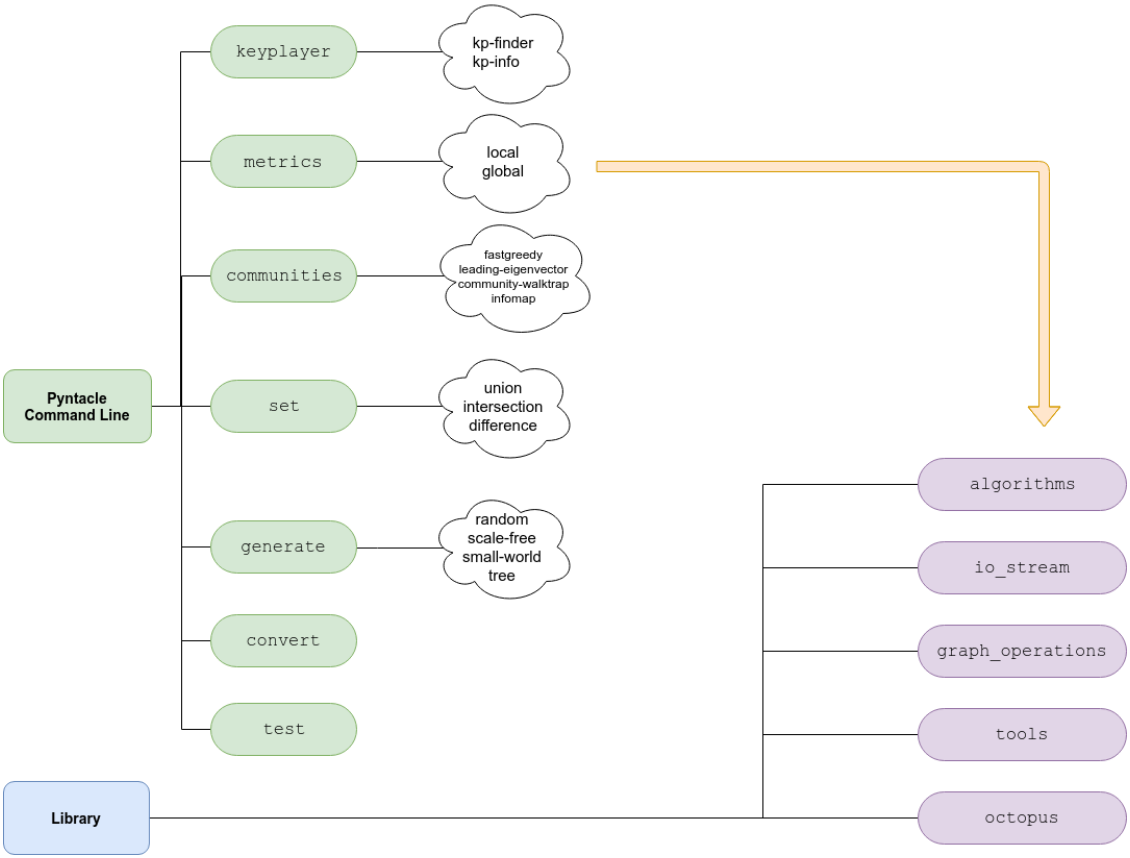

Figure 25: The directory tree of the command line interface and the Pyntacle library: green shapes enlist all the possible Pyntacle command line sub-commands. Violet boxes represent the most important Pyntacle modules upon which the command line is built.

2. Availability, installation, and testing

Pyntacle is cross-platform and can be installed on a wide range of operating systems (Table 6). The main distribution channel is the *Anaconda* package manager, which is an open-source repository and environment management system that runs on Windows, macOS, and Linux. Users can install Pyntacle through Miniconda, a mini version of Anaconda, which includes the most essential binaries for Python from the version 2.3 onwards. Miniconda allows to install automatically Pyntacle and to take care of its software dependencies. The source code is versioned and made available on the Pyntacle official GitHub page: https://github.com/mazzalab/pyntacle. Finally, to make the installation and usage of Pyntacle easier, we built a Docker image on Ubuntu 16.04 and have made it available on the Docker Hub website: https://hub.docker.com/r/mazzalab/pyntacle. The Docker machine contains all the necessary requirements to run Pyntacle in a virtualized system and is best suited for servers equipped with high-performance computing hardware. A second Docker machine was built for benchmarking Pyntacle and the *keyplayer* R package by (An and Liu, 2016a). Apart from Pyntacle itself, this Docker machine contains the binary files of the *keyplayer* R package, several sample networks and a Python program that automatizes the execution of the benchmarks. Finally, a series of unit tests to ensure that Pyntacle has been correctly installed are provided and executed through the `pyntacle test` command by the Pyntacle command line. Appendix 1 contains a Quick Startup Guide, available taken verbatim from Pyntacle website, that allows the user to familiarize with the core abilities of Pyntacle.

	Conda	*Docker*	*Binaries*
Windows	✓	✓	
Mac	✓	✓	✓
Debian/Ubuntu	✓	✓	✓
Centos	✓	✓	✓
Other Linux Distributions	✓	✓	

Table 6: Availability of Pyntacle for each supported operative system and all the distribution channels.

3. Shortest Path search strategies

The shortest path is the minimum least distance that occurs between a pair of vertices *{i,j}* in a network with the assumption that they are connected, meaning that at least one path exists that connects the two pairs. If the nodes are disconnected, the distance is infinite by definition. In simple graphs, this distance is measured in terms of *hop*, which is the minimum number of edges between the node pairs. This distance is computed differently according to the network type: in undirected weighted networks, for example, the shortest path is the one with the minimum sum of the weights over the edges that make the path between two nodes. Computing the shortest path is a computationally intensive task since its execution time increases with the size of the network. Solving the problem of finding the shortest path between two nodes in the least amount of time has been widely explored. For simple graphs, all shorting paths connecting a given node to

all other nodes of a network can be computed by the Dijkstra's algorithm (Dijkstra, 1959) with a temporal complexity of $O(|V|^2)$, where V is the number of nodes of a graph. Finding all the shortest paths between any pair of nodes is as challenging as propedeutical for the key-player algorithms implemented in Pyntacle. To this extent, we provided two parallel versions of the Floyd-Warshall algorithm (Floyd, 1962), one running on multicore computers and the other on CUDA-enabled graphic processors. This was made possible resorting to Numba, a Python library that translates Python functions into machine code optimized for high-performance computing (HPC) hardware and relieves the heavy computational requirements ($O(|V|^3)$). However, CPU and GPU accelerations are not required with small graphs, since the computing overheads are largely greater that the overall computing times on single CPU cores. For this reason, we implemented a decision-tree-based algorithm that drives the choice of the best *computing mode* (i.e., single CPU, multi-CPU in parallel or GPU) based on the topological features (i.e., number of nodes and density) of the network to be analyzed (Figure 26). As anticipated, one of the criteria used to choose the best computing mode is the graph *density* (**Δ**), which is defined as:

$$\mathbf{\Delta} = \frac{2E}{N(N-1)}$$

where *E* is the total number of edges over the total number of nodes *N*.

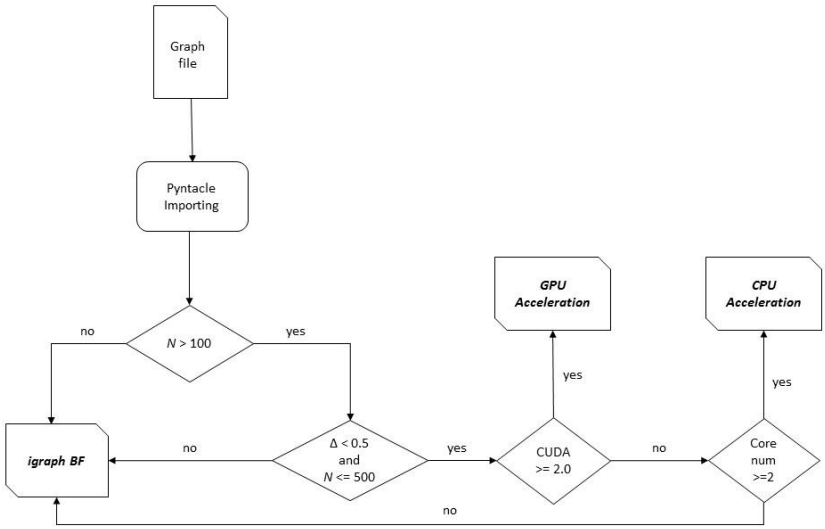

Figure 26: A decision tree driving the chosen of the best computing mode for the computation of the shortest paths. *N*=number of nodes in the graph; Δ=graph density; igraph BF: the igraph shortest path implementation through brute-force.

4. Canonical and non-canonical centrality indices

Pyntacle is equipped with a series of classical local and global centrality metrics. The complete list of these metrics is available in Table 6, where it is also specified whether the measure was borrowed from *igraph* or designed and implemented in Pyntacle. We distinguish between three groups of metrics.

- Local metrics for individual nodes;

- Global metrics for the whole graph;
- Key-Player metrics for groups of nodes.

All these metrics are implemented through Python static methods, which thus can be quickly used in Python shell environments and in interactive notebooks, as for example the popular Jupyter Notebook (Kluyver et al., 2016; Pérez and Granger, 2007).

Among these metrics, the most known is the *degree*, *k*. It is defined as:

$$k_i = \sum_j a_{ij}$$

where *a* is a link between the node *i* and *j*. For binary networks, *a*=1, as multigraphs are not currently supported. The degree distribution of all nodes is fundamental to define the overall topology of a graph as well as to calculate the *average degree* ($< k >$) of a network:

$$< k > = \frac{\sum_{1 \leq i \leq n} k_i}{n}$$

where *n* is the total number of vertices of a network.

Another core metrics universally considered to be a good evaluator of node centrality is the *betweenness* (*g*). It is defined, for a vertex *v*, as:

$$g(v) = \sum_{s \neq v \neq t} \frac{\sigma_{st}(v)}{\sigma_{st}}$$

where σ_{st} is the total number of shortest paths from node *s* to node *t* and where $\sigma_{st}(v)$ is the number of the paths that pass through the vertex *v*. It is then clear that the betweenness is important whenever searching for vertices that are essential in the information flow through a graph. Node *betweenness* (*b*) is based on the shortest path calculation, introduced in the previous section. The same holds for the *closeness* (*c*) centrality, which is another local metrics based on the reciprocal of the sum of the length of the shortest paths between the node of interest and all the other nodes, over the total number of nodes in the graph:

$$c(v) = \frac{V}{\sum_y d(y,x)}$$

where *d(y,x)* is the distance between vertices *x* and *y*. The distance between disconnected nodes, in this case, is defined as the reciprocal of infinity, hence 0. The closeness measures how easily other vertices can be reached from a node.

Another good evaluator of centrality is the *diameter (D)*, which is the longest shortest path in a network:

$$D = max(d(x,y))$$

Finally, it is important in real-world networks to measure the degree to which nodes in a group tend to cluster together. For this reason, we included in Pyntacle the well-known *clustering coefficient (CC)*, an index that can be computed both locally and globally. The global version is meant to quantify the overall clustering in the network, whereas the local gives an indication of the embeddedness of individual nodes. The local clustering coefficient for a vertex v_i is then calculated as the proportion of links between the vertices

within the neighborhood of v_i divided by the number of links that could possibly exist between them:

$$CC_i = \frac{number\ of\ closed\ triangles\ conected\ to\ v_i}{number\ of\ triples\ centered\ around\ v_i}$$

where a triple centered around v_i is a set of two edges connected to i. Hence, two measures of *CC* can be derived, both included in Pyntacle. The first one, the *average clustering coefficient* (*CC*) is defined as the average of all clustering coefficients of a network:

$$CC = \frac{1}{N}\sum_{i=1}^{n} CC_i$$

where *N* is the total number of nodes in the graph. High values of clustering coefficients of a network denote the tendency of the network to be highly clustered and connected, a property that is typical of *small-world* networks (Watts and Strogatz, 1998).

The second global clustering coefficient index is the *weighted clustering coefficient* (CC_w) (Scott et al., 1996), which is the average of each node's clustering coefficient weighted by their degree values:

$$CC_w = \frac{1}{N}\sum_{i=1}^{n}\frac{CC_i}{k}.$$

Furthermore, the PageRank algorithm (Page et al., 1998) was added to the Pyntacle's collection of algorithms. It was already used in biology to derive hierarchies among nodes (Li and Zhao, 2016). Similarly, the *radiality* (*R*) metrics, also known as *integration centrality*, was implemented to measure the closeness of a node in respect to the other nodes of a network. It is defined as:

$$R = \frac{\sum_{i \neq j} D - d_{ij} + 1}{D(n-1)}$$

where *n* is the total number of nodes in a graph, *d* is the distance between a vertex *i* and all other nodes *j* and *D* is the diameter. High values of radiality denote that a node is generally closer to the other nodes. Lower values, on the contrary, mean that a node is peripheral.

The second global clustering coefficient index is the *weighted clustering coefficient* (CC_w) (Scott et al., 1996), which is the average of each node's clustering coefficient weighted by their degree values:

$$CC_w = \frac{1}{N} \sum_{i=1}^{n} \frac{CC_i}{k}.$$

Metric	Property of	Implemented in
Degree	node	igraph
Shortest Path	node	igraph and Pyntacle
Betweenness	node	igraph
Closeness	node	igraph
Clustering Coefficient	node	igraph
Eccentricity	node	igraph
Pagerank	node	igraph
Eigenvector Centrality	node	igraph
Radiality	node	Pyntacle
Radiality Reach	node	Pyntacle
Diameter	graph	igraph
Radius	graph	igraph
Number of Components	graph	Pyntacle
Density	graph	igraph
Pi	graph	Pyntacle
Average Clustering Coefficient	graph	igraph
Weighted Clustering Coefficient	graph	igraph
Average Degree	graph	Pyntacle
Average Radiality	graph	Pyntacle
Average Radiality Reach	graph	Pyntacle
Average Closeness	graph	Pyntacle
Average Eccentricity	graph	Pyntacle
Completeness - naive	graph	Pyntacle
Completeness	graph	Pyntacle
Compactness	graph	Pyntacle
F	group of nodes	Pyntacle
dF	group of nodes	Pyntacle
m-reach	group of nodes	Pyntacle
dR	group of nodes	Pyntacle

Table 7: The topological indices implemented in Pyntacle, along with the nature of the metrics and their source (if ported from igraph or written from scratches in Pyntacle.

Furthermore, the PageRank algorithm (Page et al., 1998) was added to the Pyntacle's collection of algorithms. It was already used in biology to derive hierarchies among nodes (Li and Zhao, 2016). Similarly, the *radiality* (*R*) metrics, also known as *integration centrality*, was implemented to measure the closeness of a node in respect to the other nodes of a network. It is defined as:

$$R = \frac{\sum_{i \neq j} D - d_{ij} + 1}{D(n-1)}$$

where *n* is the total number of nodes in a graph, *d* is the distance between a vertex *i* and all other nodes *j* and *D* is the diameter. High values of radiality denote that a node is generally closer to the other nodes. Lower values, on the contrary, mean that a node is peripheral. The formulation of the radiality lacks precision when a network has more than one component, as the distance between disconnected nodes is infinite by definition. Considering that many biological networks, such as pathways or correlation networks, are often composed of several components, we reformulated the radiality equation. The modified version is called *radiality-reach (RR)* and, for any vertex *i* belonging to the component *k*, it can be formulated as:

$$RR_i = R_{i \epsilon k} \frac{s_k}{N}$$

where s_k is the size of the component *k* for the node *i* and where *N* is the overall size of the network. This ensures that the radiality is proportional to the size of the component

in a network and that nodes with high radiality and that belong to a bigger component counts more than nodes in other components. The radiality-reach has the same numerical boundaries than the radiality. It equals 0 when the node is an isolate, while it holds the same value of radiality if the network is composed by a single component only.

Finally, we addressed in Pyntacle the issue of providing the biological community clear metrics to measure the sparseness of a graph. The definition of the level of *denseness (*or *sparseness)* of a network was relegated to abstract concepts or rule-of-thumbs. Generally speaking, a dense graph is meant to have a number of edges (*E*) that is closest to the maximum number of possible edges. Conversely, a sparse graph has a number of edges that is close to the number of nodes (*N*). While these assumptions hold true for when the number of edges is higher or lower than the total possible number of nodes, this definition become weaker when *E*/*N* approximates to the 0.5 threshold, as this raises uncertainty in whether to classify the network as dense or sparse. Moreover, graphs with different sizes may have the same density, still exhibiting different numbers of zeros and non-zero elements in their adjacency matrices. For this reason, in the past few decades researchers struggled to propose clear and distinct definitions of network sparsity. Ràndic and De Alba proposed the *compactness* index (ρ) (Randic, 1997) as:

$$\rho = \left(\frac{N^2}{2E} - 1\right) * \left(1 - \frac{1}{N}\right)$$

where *E* and *N* are the total number of nodes and edges, respectively. This formula is asymptotical, as networks with $\rho > 1$ are classified as dense, while graphs with $\rho < 1$ are classified as sparse. Every graph exhibits either a greater or a smaller ρ number than the critical value since this last is not analytically obtainable by the formula. Inspire by this

index, other metrics were proposed such as the *completeness* index (κ) (Mazza et al., 2010), which is defined as:

$$\kappa = \frac{E}{Z} = \frac{\sum_{i \in V} \sum_{j \in V, j \neq i} a_{ij}}{\sum_{i \in V} \sum_{j \in V, j \neq i} 1 - a_{ij}}$$

Although the two indices look really close in most cases, their difference increases when the size and the density of the graphs increase. This is a direct consequence of the unbalanced formula of the *compactness* index which underestimates (and hence misclassifies) large and extremely dense graphs. Both these metrics, as well as other less notorious definition of sparseness are implemented in Pyntacle.

5. Group-centrality and key-player metrics

The negative key-player problem (KPP-NEG) aims at defining metrics that better represent the role of a group of nodes in terms of cohesiveness. Some local metrics exist that can be calculated to assess the overall network cohesion, as e.g., the node degree or betweenness centrality. However, there are cases where these may fail. Let us consider, for example, the toy network in Figure 27 and reported in the original Borgatti's paper. Degree and betweenness would agree to consider node 1 the best option to fragment the network. However, this choice has no effect on disconnecting the network, since a link between nodes 7 and 8 remains that keeps the total number of components to 1. In contrast, removing node 8 does create two components, although itself does not exhibit the highest centrality values.

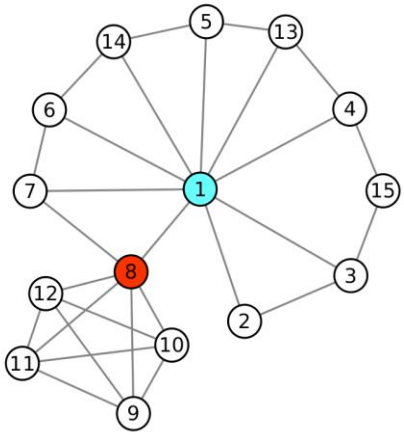

Figure 27: The toy network used by Borgatti to explain the KPP-NEG problem. Node 1 (in blue) is the node with the highest degree (*k*=9). However, its removal has no effects on the network cohesiveness compared to the removal of node 8 (in red), that creates, instead, two separate components even if its degree is lower than that of node 1 (*k*=6).

To solve this problem, two metrics were proposed: *F* and *dF*. These two metrics are both global metrics that represent the overall fragmentation status of the network. The first one stands for *fragmentation*. It counts the number of sub components and is defined as:

$$F = \frac{\sum_k s_k(s_k-1)}{n(n-1)}$$

where *n* is the number of nodes, and s_k is the size (number of nodes) of the k_{th} component. F ranges from 0 to 1. If a network has only one component, F = 0. If a network consists of only isolates, F = 1.

The other fundamental fragmentation metric is distance fragmentation, *dF* and is defined as:

$$dF = 1 - \frac{2\sum_{i>j}\frac{1}{d_{ij}}}{n(n-1)}$$

where d_{ij} is the distance between the i_{th} node and the j_{th} node and is 1 when the nodes are adjacent and 0 (the inverse of the distance) when the nodes are unconnected, as they belong to different network subcomponents. As for *F*, *dF* ranges from 0 to 1, with 0 representing a clique (every node is connected to each other) and 1 representing a network of isolates.

Biological networks are less susceptible to fragmentation than other kinds of networks. This might be due to their high redundancy that, in turn, works protecting from different types of perturbation (e.g., genetic mutations, environment). Perturbations are tackled by robust traits, like modularity, bow-tie architectures, degeneracy, and other topological features. Robustness is a topological property and is linked to the network density only marginally. Removal of only the edge connecting two groups of nodes in a dense network might, in fact, be critical and cause the fragmentation of the network.

The second concern relates to the shortest path calculation for the *dF* metrics. The calculation of the shortest paths for all nodes in a graph is a computationally intensive task, whose time of execution scales with the size and the sparsity of a network. The formulation of the *dF* includes the calculation of the shortest paths between any pair of nodes in a network. This might be computationally demanding and time-consuming when computing *dF* on a large network ($>10^3$ nodes), especially when searching for key-player.

Moreover, network density appears to heavily impact on running times, as shown in our benchmarks. Multicore/GPU computing techniques were exploited to alleviate the overall computational load and increase algorithmic performance.

The second problem is known as the positive key-player positive (KPP-POS). It concerns the accessibility and the information spreading from a group of nodes of a network through their direct and indirect partners. This problem can be formulated as follows:

*"*Given a graph *G*, with *n* nodes and *l* links, what is the subset of *n* of size *k* that can reach as many remaining nodes as possible via direct links or shortest paths?*"*

This problem introduces the concept of *reachability*. When dealing with reachability, one immediately thinks to the *closeness* metrics. Thus, the more central a node, the closer it is to all other nodes. However, even if node 4 of the graph in Figure 28 has the highest closeness measure, it is not the most central node in terms of reachability, since it reaches 6 nodes with 2 links or less, while node 3 can reach 8 nodes with 2 links or less.

The conclusion is that canonical metrics may provide sub-optimal solutions, that however might be improved by topological metrics designed for groups of nodes. We hence implemented two reachability metrics to cope with this issue: *m-reach* and *dR*.

m-reach (C_k) is a reachability measure that counts how many unique nodes can be reached from a node set in *m* steps, where *m* is the maximum distance (shortest path) between the set and the remaining nodes. The formulation is:

$$C_k = \sum_{j \epsilon V-K} \bigcup_{i \epsilon K}^{m} r_{ij}$$

where *m* is the minimum distance between any node *i* belonging to the set *K* and any node

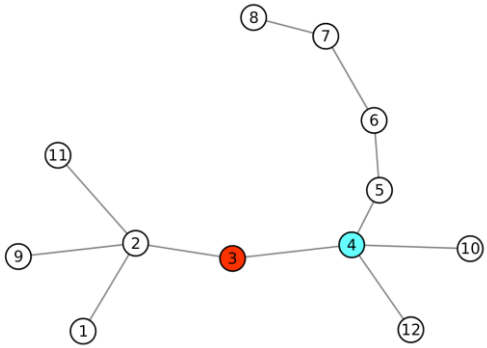

Figure 28: Toy network to explain the concept of reachability. Node 4 (in blue) has the highest closeness value (*C*=0.5). However, if we aim at finding the node that reaches the most of other nodes in two steps or less, node 3 (in red) is the best choice although having a closeness value of *C*=0.48.

j outside the set, while ${}^{m}r$ is a reachability matrix, where ${}^{m}r_{ij} = 1$ if *i* can reach *j* via a path of length *m* or less, and ${}^{m}r_{ij} = 0$ otherwise. The *m-reach* ranges from 0 to *n-k*, where *n* is the total number of nodes while *k* is the size of the set. The disadvantage of this measure is that it assumes that all paths of length *m* or less are equally important and that all paths longer than *m* are wholly irrelevant.

dR stands for *distance-weighted Reach* and, as *dF*, is a more sensitive measure of the distances (shortest path) between the node set and the remaining nodes in the graph. It is defined as:

$$dR = \frac{\sum_j \frac{1}{d_{Kj}}}{n}$$

where *n* is the total number of nodes in the graph and d_{Kj} is the minimum distance (shortest path) between any member *i* of the node set and the remaining nodes in the

graph. In the toy graph shown in Figure 29, the distances between the nodes {1,7}, which make the set of interest, are set to 1 by convention. Thus, $d_{K,1}$ = 1 and $d_{K,7}$ = 1. The distance from the set to node 5 is 1, since 1 is the length of the shortest path from either 1 or 7 to 5. Similarly, $d_{K,3}$ = 1, $d_{K,4}$ = 2, $d_{K,2}$ = 2, $d_{K,6}$ = 2. Hence, *dR* ranges from 0 and 1. It is 0 when the set is completely disconnected from the other nodes. It is 1 when the set is adjacent to all other nodes of the network.

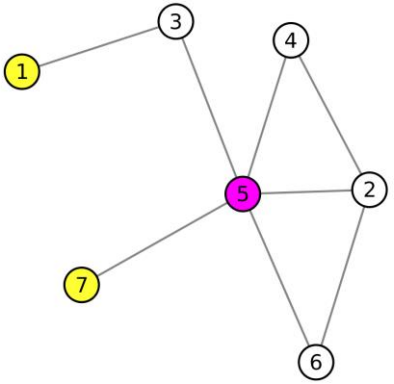

Figure 29: Toy network to explain the *dR* metrics. Node 5 (pink) is reach by node 1 in two hops, and by node 7 in 1 hops the latter is taken as the minimum distance between the set {1,7} and node 5.

6. Key player search optimizations

Pyntacle allows to search for the best key-player set (kp-set) that maximizes the fragmentation or the reachability of a given set of size *k*. Two methods currently exist to

do that. The first one is a *greedy optimization* search algorithm. It does not aim at finding the best kp-set, as this would require:

$$\frac{N!}{(N-k)! * k!}$$

iterations, where N is the size of the graph and k is the size of the group. While these operations can easily be performed on small networks (<= 1000 nodes), the increase of both the size of the network and of k may have dramatic consequences in terms of computating time. The optimization works by first selecting a group of nodes of size k, and then by swapping every member in the node set with each other nodes in the graph until there is no set with a better centrality value. The following pseudocode summarizes the operation performed during any iteration:

```
1. select k nodes at random to populate the set S
2. define an initial value for the kp metric of choice for S
3. for each node u in S and each node v not in S:
      a. compute DELTAkp = difference in the kp-metric if u and v
         were swapped
4. select the set with the highest DELTAkp
      a. if DELTAkp > max(all DELTAkp recorded), terminate, else:
      b. swap nodes with the greatest improvement in fit and store
         the DELTAkp value and the node set
5. Go to step 3
```

The *greedy optimization* is the default method in the `pyntacle kp-finder` command line tool, while it can be enabled using Pyntacle as a library by either importing and using the `GreedyOptimization` class in the `algorithms.greedy_optimization` module or through the `add_GO` method of `octopus`. For the moment, in the official release of Pyntacle the Greedy optimization cannot run in parallel. The pitfall of the greedy optimization method is that, only one kp-set is found for a given metric and it might not be the best solution, but only a suboptimal (local minimum) solution.

To address this issue, we implemented another strategy that implement a brute-force search algorithm. As previously stated, this is a computational intensive method and requires high computing times that will tend to infinity on a network of even moderate size using a modest computing hardware. Thus, we implemented a brute-force search that exploits parallel computing on multiple CPUs through the *multiprocess* python library (https://docs.python.org/3.4/library/multiprocessing.html). The brute-force search simply enumerates all possible sets of nodes and calculates the selected centrality for each of them. Finally, it ranks all sets and returns the best solutions. The following pseudocode generalizes the brute-force search for any key player metric:

```
1. let N be the number of available threads
2. define all combinations c of size k for all the vertices v in a graph
3. assign an equal number of combinations to each thread
4. for each thread in N:
 a. compute all the values for each subset of k
5. regroup all the combinations and
6. select the kp-sets that hold the maximum value for the given kp metric
```

Bruteforce search can be enabled in the `pyntacle kp-finder` command line tool by passing the `–implementation brute-force` argument, while the number of threads can be passed through the `--threads` argument. If not specified, Pyntacle uses all the threads available on the machine in which it is running minus one. In the Pyntacle library, brute-force can be invoked using the `BruteForce` class in the `algorithms.brute_force` module or through the `add_BF` method of `octopus`.

7. Ancillary operations

A plethora of ancillary functionalities was added to Pyntacle. We divided these graph operations in two classes:

- *Logical set operations* and
- *Community finding algorithms*

The first class of operations is used to perform the *union*, *intersection* and *difference* among two graphs as described in (Harary, 1994; Skiena, 1990). For intersection, we consider the intersection G_3 between two graphs G_1, formed by v_1 and e_1 vertices and edges, and G_2, with v_2 and e_2 edges, the common set of nodes and edges between the two, such as:

$$G_3[v_3, e_3] = \ G_1[v_1, e_1] \cap G_2[v_2, e_2]$$

The union of two graphs on the other hand, is the union of edges and vertices of G_1 and G_2:

$$G_3[v_3, e_3] = G_1[v_1, e_1] \cup G_2[v_2, e_2] = [v_1 \cup v_2 , e_1 \cup e_2]$$

Finally, the difference graph G_3 is the intersection among the set of edges minus the connecting edges in common between the two graphs G_1 and G_2, such as:

$$G_3[v_3, e_3] = G_1[v_1, e_1] \setminus G_2[v_2, e_2] = [v_1 \cup v_2, e_1 \setminus e_2]$$

Community finding algorithms on the other hand are means to divide a graph into several induced subgraphs of tightly associated nodes with respect to the rest of the graph. Community finding is an open field and different algorithms are used depending on the scientific context. In general, there is no correct solution when defining communities, because the definition of a community is itself questionable. Each partitioning algorithm relies on its definition of *modularity*, a measure to distinguish how tight is the group of nodes identified as a community, and on specific thresholds that are used to distinguish one community from another one. For this reason, we implemented some of the most famous algorithms in community finding for scale free, small-world and random graphs. Specifically, we focused on the *fastgreedy* algorithm (Clauset et al., 2004), the *infomap* algorithm (Rosvall and Bergstrom, 2007), the *leading eigenvector* algorithm (Newman, 2006) and the *walktrap* algorithm (Pons and Latapy, 2006). The explanation of each algorithm is beyond the scope of this work, but to generalize, we will focus on the *fastgreedy* algorithm by Clauset, that works best on large and sparse networks with an underlying hub-and-spoke configuration, such as many biological networks. This algorithm assigns at first a *modularity* score on each node of the network based on the interconnectedness with its neighbors. Through a series of iteration, adjacent nodes with similar modularity scores are merged until the difference between each group of nodes is such that they cannot be merged anymore. The threshold for defining the merge cut point

is found through a clustering based on Euclidean distances, that dynamically defines the modularity threshold according to the distance between branches. Dense networks or small networks may not show distant cut points; hence the algorithm could also fail at defining distinct communities. Therefore, it is suited for large graphs.

8. Supported network file formats

Pyntacle is compliant to a variety of network file formats. The first and most common is the network representation through *adjacency matrix*. An adjacency matrix is a squared *nxn* table.

Both row *i* and column *j* indices refer to nodes in a network. Non-zero values filling cells (a_{ij}) indicate the presence of connecting edges between the relative nodes, so that

$$a_{ij} = \begin{cases} \neq 0 \text{ if there is an edge from } j \text{ to } i \\ 0 \text{ otherwise} \end{cases}$$

The values stored in each cell of the matrix represent connection among nodes. Several types of matrices exist that can represent different network types, from unweighted and undirected to weighted and directed. In Pyntacle, we only support simple graphs. Their adjacency matrices will hold ones between two distinct nodes if these are connected by an edge, and zeroes otherwise.

$$a_{ij} = \begin{cases} 1 \text{ if there is an edge between } j \text{ and } i \neq j \\ 0 \text{ otherwise} \end{cases}$$

Self-loops are not allowed. Adjacency matrices usually have a header, but this is optional. In the first scenario (header is present), we assume that the header is in both the first row and the first column of the file and identical, like in the example in Figure 30A.

A

	A	B	C	D	E
A	0	1	1	0	0
B	1	0	1	1	0
C	0	1	0	0	0
D	0	1	0	0	1
E	0	0	0	1	0

B

V1	V2
A	B
B	A
B	C
C	B
A	C
C	A
B	D
D	B
D	E
E	B

C

ProteinA	Interaction_Type	ProteinB
protein_1	physical	protein_2
protein_1	activation	protein_2
protein_1	physical	protein_3

Figure 30: Toy examples of network text file formats supported by Pyntacle. A) Adjacency matrix B) Edge list C) Simple Interaction File (SIF).

In the case the matrix does not have a header, the vertices are enumerated from the first to the last row. Adjacency matrices can have any file extension. By default, the `.adjm` extension is used. Cells in an adjacency matrix file are supposed to be delimited by tabulation (\t, or tab) unless otherwise specified. If not explicitly specified, the separator character will be inferred, before resorting to the default choice.

Edge Lists files are another common way to store a graph. An edge-list is a list, or array, containing pairs of nodes. Thus, each element of the array represents a link directionally connecting the first (a) to the second (b) node of the pair. If a network is meant to be undirected, each pair a→b must be accompanied by a pair b→a, such as the example reported in Figure 30B. We support undirect, unweighted edge lists, separated by a uniform separator character. As for adjacency matrices, Pyntacle uses the `.egl file` extension by convention, but files can have any extension as long as they store text. Pyntacle was equipped with a parser for the Simple Interaction File (SIF) format. It is the most used format by standard application for biological networks analysis and visualization, like Cytoscape (Shannon et al., 2003). Its syntax is agile and simple. It allows Cytoscape to represent properties of both networks and edges. Usually, the file is made by 3 or more columns (see Figure 30C). The first and third column represent the source and target nodes with the type of their interaction specified in the 2nd column. The order of the columns is just conventional, and it is generally not relevant, as the user can choose what is the meaning of these columns in the process of importing a network in Cytoscape.

The last textual file format supported is the DOT file format. DOT is a widely known file format with an easy syntax that is well suited to graph plotting. It is widely used by graphical visualization tools such as Graphviz (Ellson et al., 2004). The power of DOT relies just on its syntax, that allows to interpret and store much graphical information (like edge thickness or node colors with gradients), thus representing networks used in several kinds of contexts. More information on the DOT file format can be found on the official Graphviz documentation. Many tools already support the importing and exporting of DOT files, such as the popular NetworkX library. igraph, on the other hand, supports only

the exporting of DOT files. We implemented a parser that addresses the specific problem of importing undirected networks.

Finally, networks can be given to Pyntacle as pickled binary files containing igraph objects, if these graphs are compliant with the *minimum requirements* described in Appendix 2.

9. Benchmarks data

We performed benchmarks on a dataset comprising 12 test networks, that are listed in Table 8. The dataset contains a variety of small (N<100), medium ($N \geq$100 and N<1000) and large ($N \geq$1000) sized graphs, stored in binary adjacency matrices. These networks come from two sources. Six of them are real networks. The three food webs (*carpinteria*, *north*, *cat*) were downloaded from the NCEAS ecological repository (www.nceas.ucsb.edu/interactionweb) and have the minimum, maximum and median number of nodes among all the food webs available in NCEAS. These case studies allow studying the interplay among species using the key-player algorithms, as described in the chapter 4 of Results. The *Caenorhabditis elegans* connectome (*CAEEL_connectome*), downloaded from wormbase database (http://www.wormatlas.org/neuronalwiring.html#Connectivitydata), represents a well-studied case of a small world network (Towlson et al., 2013). The PPI interactome of the small nematode is a well-known example of scale-free topology (Li et al., 2004). The advice-seeking ties among global consulting companies (*AdvSeek* network) is the smallest network (N=32, E=55, Δ=0.11089) taken from (Borgatti, 2006) (Figure 8 in the corresponding paper). The biggest is the interactome of *C. elegans* (N=3303, E=5561,

Δ=0.00102) downloaded from APID on February 2018. All the networks were converted into undirected networks while weights were neglected. Only the largest component of each network was considered.

The remaining six models are binary networks that follow random topologies. They were created according to the Erdős–Rényi model (Erdős and Rényi, 1959) by means of one of the Pyntacle's generators. The size of the networks ranges from n=100 to n=1000, while the wiring probability ranges from P = 0.3 to P = 0.7 at steps of 2, where P is the probability that a link is placed among a pair of nodes.

Network	Type	*N*	*E*	Δ
Carpinteria	NCEAS Food Web	128	1198	0.14739
North	NCEAS Food Web	78	228	0.07592
Cat	NCEAS Food Web	48	107	0.09486
AdvSeek	Borgatti Case Study	32	55	0.11089
CAEEL_connectome	Neuronal wiring of the nematode *C. elegans*	279	1960	0.05054
Random 100-0.3	Artifical network	100	1492	0.30141
Random - 100-0.5	Artificial network	100	2489	0.50283
Random - 100-0.7	Artificial network	100	3426	0.76582
Random 1000-0.3	Artificial network	1000	149998	0.3003
Random 1000-0.5	Artificial network	1000	249983	0.50047
Random 1000-0.7	Artificial network	1000	349370	0.69944
APID_CAEEL	Level 2 interactome of *C. elegans* downloaded from APID	3303	5561	0.00102

Table 8: Description of the test networks used for benchmarking Pyntacle. *N*=total number of nodes; *E*=total number of edges, Δ=graph density. Blue, orange and green colors mark big, medium and small sized graphs, respectively.

10. Benchmarks specifications

Benchmarks were performed on a custom Docker Image running Ubuntu 16.04, that can be downloaded at https://hub.docker.com/r/mazzalab/pyntacle_benchmarks/. This Docker machine was deployed into a local server equipped with 4 AMD Opteron® processor 6172 @2100MHz frequency, with 12 CPU cores each, 256 GB of RAM and connected by InfiniBand through Mellanox/Intel host bus adapters and network switches. CUDA acceleration was not available.

Pyntacle version 0.2.4 and the keyplayer R Package (An and Liu, 2016b) version 1.0.3 were installed in the Docker machine. Binaries for the two packages were retrieved from Conda and CRAN, respectively. The key-player search was performed by means of the *greedy optimization* algorithm, which was run for all the small and medium-size networks described in the previous section. For Pyntacle, we run the `keyplayer kp-finder` command, setting a seed of 100. For the R *keyplayer* package, we wrapped its greedy optimization method in a custom R script, and timing was measured using the default timing libraries provided by R version 3.4.

A *kp*-set size of 2 was sought with both software. The timing of the greedy optimization was calculated only for comparable key-player metrics. The R package lacks for the *F* fragmentation measure, while the *dR* formulation slightly differs from the one described by Borgatti (section 5 of this chapter).

The remaining key player metrics, *dF* fragmentation and m-reach reachability, were comparable in their formulations. For m-reach, its maximum distance was set to 1 for both tools. The maximum allowed execution time for each algorithmic iteration was set

to 1 week. For Pyntacle, the brute-force search for was performed for small size networks. Speedup plots for each key-player metric were obtained by dividing the execution times measured on single cores over their timings using 4,8,16 and 32 CPU cores. For all benchmarks, times were measured in triplicate, and the results were summarized by computing the mean of the times μ_T and their standard deviations σ_T.

3. The *nestedness* of food-webs

1. Food webs

We used 27 food webs freely available from the NCEAS database (www.nceas.ucsb.edu/interactionweb). These describe various, mostly terrestrial ecosystems. Before conducting any analyses on them, we deleted isolated nodes and small components from the networks and focused only on their giant component (this typically meant to delete only 0-5% of the original nodes).

- *aka an* (Akatore A, pine forest, Otago, New Zealand);
- *aka b* (Akatore B, pine forest, Otago, New Zealand);
- *ber* (Berwick, pine forest, Otago, New Zealand);
- *black* (Blackrock, pasture grassland, Otago, New Zealand);
- *broad* (Broad, pasture grassland, Otago, New Zealand);
- *cant* (Canton, pasture grassland, Otago, New Zealand);
- *carpinteria* (Carpinteria salt marsh, California, USA); *cat* (Catlins, pine forest, Otago, New Zealand); *cow1* (Coweeta1, pine forest, North Carolina, USA); *cow17* (Coweeta17, pine forest, North Carolina, USA);
- *demp au* (Dempsters tussock grassland in autumn, Otago, New Zealand);
- *demp sp* (Dempsters tussock grassland in spring, Otago, New Zealand);
- *demp su* (Dempsters tussock grassland in summer, Otago, New Zealand);
- *german* (German, tussock grassland, Otago, New Zealand);
- *healy* (Healy tussock grassland, Otago, New Zealand);
- *kyeb* (Kyeburn, tussock grassland, Otago, New Zealand);

- *lilkye* (LilKyeburn, tussock grassland, Otago, New Zealand);
- *martins* (Martins, pine forest, Maine, USA);
- *narr* (Narrowdale, pine forest, Otago, New Zealand);
- *north* (NorthCol, broadleaf forest, Otago, New Zealand);
- *powder* (Powder, broadleaf forest, Otago, New Zealand);
- *stony* (Stony, tussock grassland, Otago, New Zealand);
- *sutton au* (Sutton tussock grassland in autumn, Otago, New Zealand);
- *sutton sp* (Sutton tussock grassland in spring, Otago, New Zealand);
- *sutton su* (Sutton tussock grassland in summer, Otago, New Zealand);
- *troy* (Troy, pine forest, Maine, USA);
- *ven* (Venlaw, pine forest, Otago, New Zealand).

Geographic distribution is thus quite narrow, but this does not seem to have any known effect on the results.

2. Network analysis

We calculated nine global (macroscopic) topological properties for each network using Pyntacle. The number of nodes (N) and the number of interactions (E) are trivial properties of every network. We used this information to compute the density Δ of each food web (see the "Shortest Path search strategies" section above). For each species in each food web, we also computed the degree k, and used it to compute the average degree $<k>$ for all nodes in the network. Finally, we computed the clustering coefficient CC_i and

used it to derive for each network its average clustering coefficient *CC* and its weighted global clustering coefficient CC_w. This latter puts larger emphasis on clusters around more connected nodes. The whole networks were characterized by the average shortest path lengths (<*Sp*>) and their maximum values, the diameters, *D*. Finally, the distance weighted fragmentation (*dF*) was computed for each network before performing the final key-player analysis.

3. Multi-node centrality

Multi-node centrality analyses have already been performed on different types of ecological networks including food webs (González et al., 2016) and habitat networks (Rubio et al., 2015). The most central multi-node sets of $n = 1$ to $n = 4$ nodes were identified for the 27 food webs that solved the KPP-POS and KPP-NEG problems. For the latter problem, *F and dF* where calculated. For the former problem, the *m-reach* centrality (*M*) with m = 1, 2 and 3 steps (M1, M2, and M3, respectively) and *dR* where computed. Each of these metrics were computed for groups of 1 to 4 nodes.

4. Nestedness

The *nestedness* of presence-absence ecological data (Podani and Schmera, 2011) has a rich literature with well-developed methods (An and Liu, 2016a; Kelt, 1997; Podani et al., 2013). The nestedness approach has also been extended to ecological interactions in simple graphs (Fortuna et al., 2010). Here we study the nestedness of ecological

interaction networks in a very different way (Benedek et al., 2007; Ortiz et al., 2013), quantifying the set–subset relationships of central nodes in a network. We calculated the nestedness of central node sets (i.e. the overlap among the sets of size n = 1 to 4) using the *Nrow* metric (Boland and Goel, 2010b). Nrow is the average percentage of nodes of the smaller sets that are contained in the larger sets, taking all possible pairs of sets. For example, for the food web *demp au*, the key player sets for M2 (m-reach using a maximum distance of 2) n = 1 to 4 nodes were {0} for n = 1, {0 ,2} for n = 2, {0,68,76} for n = 3 and {76,18,37,66} for n = 4. For n =1 and n = 2, there is perfect overlap. For n =1 and n = 3, there is partial overlap, since the smaller set (n =1) is a subset of the larger one (n = 3). For n= 2 and n = 4, there is no overlap, since the two sets have no common elements. Averaging all the 6 overlaps, we have Nrow = 47.22, which is the nestedness value for M2 in the *demp au* food web (see the species identities for this food web in Discussion). The same was done for the remaining centrality measures (*F*, *dF*, *M2*, *M3*, and *dR*).

4. Characterization of sex-specific mechanisms of aging in correlation networks of adult *Drosophila Melanogaster*

1. RNA-Seq data availability and processing

We downloaded the publicly available data used by Graveley (Graveley et al., 2011) from the small read archive (SRA) available at NCBI (accession number ID:SRA009364). This dataset comprises 234 raw fastq files corresponding to *Drosophila* development and aging timepoints. Each timepoint encompassed 4 to 6 biological replicates per sampling. We assessed read quality using the FastQC (Andrews, 2010) software version 0.11.5 and used Trimmomatic (Bolger et al., 2014) version 0.36 to perform read trimming and filtering. Specifically, reads were trimmed using a sliding window of 4 base calls and a minimum window average PHRED quality of 30. Reads with less than 15 nucleotides after trimming were removed. Reads were mapped by means of Tophat2 (Trapnell et al., 2009) against the Drosophila genome version 6.10 downloaded from NCBI, following developer's recommendations. Raw counts for each gene were estimated by first piling-up aligned reads on the *Drosophila* GFF annotation version 6.13 provided by FlyBase (Gramates et al., 2017), encompassing 16,271 genes, by means of the HTSeq pipeline (Anders et al., 2014) using the intersection-nonempty criterion for counting features.

2. Sex-specific co-expression network analysis and module eigengenes detection

To search for modules of sex-specific gene correlation in female and male flies, we made use of the Weighted Gene Clustering Network Analysis (WGCNA) R package (Langfelder and Horvath, 2008) version 1.64.1. WGCNA includes a series of utilities to perform module detection of groups of tightly connected genes and to summarize these

modules into module eigengenes. Module eigengenes are used to study the relationships between groups of nodes using standard correlation techniques. To build co-expression networks, raw counts of adult male and female flies were converted to reads per kilobase per million (RPKM) with edgeR (Robinson et al., 2010) and then $\log_2$ transformed adding a pseudo-count of 1 to correct genes with no counts, following the guidelines described in the WGCNA documentation. Counts with no expression over each stage were removed by means of the `goodSampleGenes` function by WGCNA, thereby filtering 4277 and 759 genes for female and male, respectively. Sample outliers were removed by performing an explorative hierarchical clustering on each development stage, and by removing samples from male 5-days replicate #1 and #4, replicate #4 and #5 for female at 5 days and the replicate #3 for female 30 days.

Signed correlation networks were derived by computing a signed correlation adjacency matrix *A*. Each cell a_{ij} stores correlations measures that lie between 0 (unconnected) and 1 (fully connected) that are computed using the signed correlation formula:

$$a_{ij}^{signed} = \left[\frac{cor(x_i, x_j)}{2}\right]^{\beta}$$

where *cor* is the Pearson correlation coefficient *r* between any pair of summarized gene expression (by average) $x_{ij.}$ β is a soft power threshold that is determined by means of the `pickSoftPowerThreshold` WGCNA function. This soft power filters weak and negative correlations and allows to approximate the corresponding correlation network to a scale-free topology. The threshold for each dataset was set to β=20 for both female and male and was chosen by looking at the connectance (average degree, <*k*>) plotted

over each soft power value, from 2 to 20, for each dataset. The correlations were then used to derive an unsigned Topological Overlap Measure (TOM) (Yip and Horvath, 2007), an index of connectedness among gene pairs that kept into account the connectance of each pair and the contribution of the common neighbors of each gene pair using the following formula:

$$TOM_{ij} = \frac{\left|a_{ij} + \sum_{u \neq i,j} a_{iu} a_{uj}\right|}{\min\left(k_i, k_j\right) + 1 - \left|a_{ij}\right|}$$

where *k* is the degree and *u* is any common neighbor of the a_{ij} pair.

Each value of the TOM matrix was then subtracted to 1 for creating a dissimilarity TOM (dissTOM) matrix, on which a hierarchical clustering was applied to detect modules that were labeled using RGB colors. These modules were then merged if their distance in the clustering dendrogram was lower than a threshold (2 for male and 1.7 for female), allowing to detect 27 final co-expression modules for male and 25 for female. Finally, module eigengenes were derived by computing the principal components of each correlation module detected, and another network of module eigengenes was computed by means of the correlations among module eigengenes. This module eigengene network was then used to assess the similarity and commonality among module eigengenes.

The genes contained in both the unmerged and merged modules for sex-specific analyses were functionally enriched *in silico*, using the *Drosophila* Gene Ontology (GO) vocabulary downloaded from R on March 2017. The redundancy in the list of significantly enriched GO terms and their summarization in upper-tree GO processes was performed by iteratively querying all the modules to ReviGO (Supek et al., 2011), a Web

server that summarizes lists of GO terms by finding a representative subset of the terms using a simple clustering algorithm that relies on semantic similarity measures.

3. Paired consensus analysis of module eigengenes of male and female flies

We performed consensus module eigengene analysis, described in (Langfelder and Horvath, 2007), in order to assess commonalities in the architecture of the corresponding adult co-expression networks. We followed the standard procedure described in the WGCNA website documentation. In brief, $\log_2$ RPKMs for each gene were filtered using the `goodSampleGenes` for multi-leveled expression data available in WGCNA filtering a total of *xxx* genes. Then signed correlations and the corresponding TOM matrices for each sex were computed using the same rationale described in the previous paragraph. The soft power threshold was raised to 20 for both data sets after evaluating topological measures for approximating both networks to a scale-free topology. To correct for the statistical variance of the two datasets, we scaled the male TOM such that the 95th percentile equals the 95th percentile of the female TOM. A quantile-quantile (Q-Q) distribution was estimated to assess the impact of the scaling on the two TOMs before computing the consensus TOM and the relative dissTOM. The latter was used to create a dendrogram based on hierarchical clustering by means of Euclidean distance. Adjacent modules were merged using a dynamic-tree cut algorithm and allowing the algorithm to choose the appropriate threshold.

The correlation network of consensus module eigengenes was then compared to each sex-specific module eigengene network. Correlation among the sex-specific and the

consensus module eigengenes was computed along with the *preservation*, the absolute correlation among the two classes of module eigengenes over the total number of consensus eigengenes.

Finally, overlaps among each consensus modules and each sex-specific module were assessed by creating a matrix of overlaps containing the common genes between any consensus modules and the sex-specific ones. A hypergeometric test was performed on each overlap to assess the significance and to filter out overlaps due by chance ($-\log(p) > 3$).

4. Network analysis of overlapping genes among consensus and sex-specific modules

We used the overlaps resulting comparing the consensus and the stage-specific modules and analyzed their effect on the corresponding stage-specific networks by means of Pyntacle. We filtered out non-significant overlaps, the overlaps whose dimension was inferior to 10 (n=10) and considered only sex-specific modules of at least 50 nodes (N=50). Modules of co-expression were mined from the global correlation networks of each stage and correlations were filtered by dividing each correlation distribution into quartiles and taking only the upper quartile, to retain only the strongest co-expression measures in the module. These induced weighted subgraphs were later turned to undirected graphs.

We first measured the global topology indices for each consensus modules and assessed the local centrality measures of module overlap measuring the degree, clustering

coefficient, closeness, and the betweenness centrality metrics for each gene in each overlap. Moreover, we performed group-centrality analysis using the distance-based fragmentation (*dF*) measure in Pyntacle by means of the `pyntacle keyplayer kp-info` command line tool to weight the effect of the removal of overlapped genes in their corresponding sex-specific modules (see "Group-centrality and key-player metrics" section).

References

Akao, Y., Nakagawa, Y., and Naoe, T. (2006). MicroRNAs 143 and 145 are possible common onco-microRNAs in human cancers. Oncol. Rep. *16*, 845–850.

Akao, Y., Nakagawa, Y., and Naoe, T. (2007). MicroRNA-143 and -145 in Colon Cancer. DNA Cell Biol. *26*, 311–320.

Alexa, A., Rahnenführer, J., and Lengauer, T. (2006). Improved scoring of functional groups from gene expression data by decorrelating GO graph structure. Bioinformatics *22*, 1600–1607.

Allen, J.D., Xie, Y., Chen, M., Girard, L., and Xiao, G. (2012). Comparing statistical methods for constructing large scale gene networks. PLoS One *7*, e29348.

Allesina, S., and Bodini, A. (2004). Who dominates whom in the ecosystem? Energy flow bottlenecks and cascading extinctions. J. Theor. Biol. *230*, 351–358.

Alon, U., Surette, M.G., Barkai, N., and Leibler, S. (1999). Robustness in bacterial chemotaxis. Nature *397*, 168–171.

Amaral, L.A.N., Scala, A., Barthelemy, M., and Stanley, H.E. (2000). Classes of small-world networks. Proc. Natl. Acad. Sci. USA *97*, 11149–11152.

An, W., and Liu, Y.-H. (2016a). keyplayer: An R Package for Locating Key Players in Social Networks. R J. *8*, 257–268.

An, W., and Liu, Y.-H. (2016b). keyplayer: An R Package for Locating Key Players in Social Networks. R J. *8*, 257–268.

Anders, S., Pyl, P.T., and Huber, W. (2014). HTSeq A Python framework to work with high-throughput sequencing data. Bioinformatics *31*, 166–169.

Andrews, S. (2010). FastQC - A quality control tool for high throughput sequence data. http://www.bioinformatics.babraham.ac.uk/projects/fastqc/. Http://Www.Bioinformatics.Babraham.Ac.Uk/Projects/Fastqc/.

Aunan, J.R., Watson, M.M., Hagland, H.R., and Søreide, K. (2016). Molecular and biological hallmarks of ageing. Br. J. Surg. *103*, e29–e46.

Ballouz, S., Verleyen, W., and Gillis, J. (2015). Guidance for RNA-seq co-expression network construction and analysis: Safety in numbers. Bioinformatics *31*, 2123–2130.

Barabasi, A.-L., Gulbahce, N., and Loscalzo, J. (2011). Network medicine: a network-based approach to human disease. Nat. Rev. Genet. *12*, 56–68.

Barabási, A.L., and Albert, R. (1999). Emergence of scaling in random networks. Science (80-.). *286*, 509–512.

Bastian, M., Heymann, S., and Jacomy, M. (2009). Gephi: An Open Source Software for Exploring and Manipulating Networks. Third Int. AAAI Conf. Weblogs Soc. Media 361–362.

Bauer, K.M., and Hummon, A.B. (2012). Effects of the miR-143/-145 microRNA cluster on the colon cancer proteome and transcriptome. J. Proteome Res. *11*, 4744–4754.

Benedek, Z., Jordán, F., and Báldi, A. (2007). Topological keystone species complexes in ecological interaction networks. Community Ecol. *8*, 1–7.

Berghella, A., Contasta, I., Marulli, G., D'Innocenzo, C., Garofalo, F., Gizzi, F., Bartolomucci, M., Laglia, G., Valeri, M., Gizzi, M., et al. (2014). Ageing gender-specific "Biomarkers of Homeostasis", to protect ourselves against the diseases of the old age. Immun. Ageing *11*, 3.

Von Bertalanffy, L. (1950). The theory of open systems in physics and biology. Science (80-.). *111*, 23–29.

Blanchard, D.A., Mouhamad, S., Auffredou, M.-T., Pesty, A., Bertoglio, J., Leca, G., and Vazquez, A. (2000). Cdk2 associates with MAP Kinase in vivo and its nuclear translocation is dependent on MAP Kinase activation in IL-2-dependent Kit 225 T lymphocytes. Oncogene *19*, 4184–4189.

Boisvert, M.M., Erikson, G.A., Shokhirev, M.N., and Allen, N.J. (2018). The Aging

Astrocyte Transcriptome from Multiple Regions of the Mouse Brain. Cell Rep. *22*, 269–285.

Boland, R.C., and Goel, A. (2010a). Microsatellite instability in colorectal cancer. Gastroenterology *138*, 2073–2087.

Boland, R.C., and Goel, A. (2010b). A consistent metric for nestedness analysis in ecological systems: Reconciling concept and measurement. Gastroenterology *138*, 2073–2087.

Bolger, A.M., Lohse, M., and Usadel, B. (2014). Trimmomatic: A flexible trimmer for Illumina sequence data. Bioinformatics *30*, 2114–2120.

Boogerd, F., Bruggeman, F.J., Hofmeyr, J.-H.S., and Westerhoff, H. V (2007). Systems biology: philosophical foundations (Elsevier).

Borgatti, S.P. (2006). Identifying sets of key players in a social network. Comput. Math. Organ. Theory *12*, 21–34.

Borgatti, S.P., Everett, M., and Freeman, L.C. (2002). UCINET 6.0 for windows: Software for social network analysis, user´s guide. Anal. Technol. Inc. 47.

Bradley, R. (2001). Understanding computer science for advanced level : the study guide (Cheltenham: Nelson Thornes).

Breitling, R. (2010). What is systems biology? Front. Physiol. *1 MAY*.

Brose, U., Cushing, L., Berlow, E.L., Jonsson, T., Banasek-Richter, C., Bersier, L.-F., Blanchard, J.L., Brey, T., Carpenter, S.R., Blandenier, M.-F.C., et al. (2005). Body Sizes of Consumers and Their Resources. Ecology *86*, 2545–2545.

Bryois, J., Buil, A., Ferreira, P.G., Panousis, N.I., Brown, A.A., Viñuela, A., Planchon, A., Bielser, D., Small, K., Spector, T., et al. (2017). Time-dependent genetic effects on gene expression implicate aging processes. Genome Res. *27*, 545–552.

Caldas, C., and Brenton, J.D. (2005). Sizing up miRNAs as cancer genes. Nat. Med. *11*, 712–714.

Calin, G.A., Sevignani, C., Dumitru, C.D., Hyslop, T., Noch, E., Yendamuri, S., Shimizu, M., Rattan, S., Bullrich, F., Negrini, M., et al. (2004). Human microRNA genes are frequently located at fragile sites and genomic regions involved in cancers. Proc. Natl. Acad. Sci. *101*, 2999–3004.

Calore, F., Lovat, F., and Garofalo, M. (2013). Non-Coding RNAs and Cancer. Int. J. Mol. Sci. *14*, 17085–17110.

Carlson, J.M., and Doyle, J. (2002). Complexity and robustness. Proc. Natl. Acad. Sci. *99*, 2538–2545.

Carlson, K.A., Gardner, K., Pashaj, A., Carlson, D.J., Yu, F., Eudy, J.D., Zhang, C., and Harshman, L.G. (2015). Genome-wide gene expression in relation to age in large laboratory cohorts of drosophila melanogaster. Genet. Res. Int. *2015*, 1–19.

Chatr-aryamontri, A., Oughtred, R., Boucher, L., Rust, J., Chang, C., Kolas, N.K., O'Donnell, L., Oster, S., Theesfeld, C., Sellam, A., et al. (2017). The BioGRID interaction database: 2017 update. Nucleic Acids Res. *45*, D369–D379.

Chen, J., Bardes, E.E., Aronow, B.J., and Jegga, A.G. (2009a). ToppGene Suite for gene list enrichment analysis and candidate gene prioritization. Nucleic Acids Res. *37*, W305–W311.

Chen, X., Guo, X., Zhang, H., Xiang, Y., Chen, J., Yin, Y., Cai, X., Wang, K., Wang, G., Ba, Y., et al. (2009b). Role of miR-143 targeting KRAS in colorectal tumorigenesis. Oncogene *28*, 1385–1392.

Cho, C.R., Labow, M., Reinhardt, M., van Oostrum, J., and Peitsch, M.C. (2006). The application of systems biology to drug discovery. Curr. Opin. Chem. Biol. *10*, 294–302.

Cho, H., Berger, B., and Peng, J. (2016). Compact Integration of Multi-Network Topology for Functional Analysis of Genes. Cell Syst. *3*, 540–548.e5.

Clauset, A., Newman, M.E.J., and Moore, C. (2004). Finding community structure in very large networks. Phys. Rev. E - Stat. Nonlinear, Soft Matter Phys. *70*, 066111.

Clauset, A., Shalizi, C.R., and Newman, M.E.J. (2009). Power-Law Distributions in Empirical Data. SIAM Rev. *51*, 661–703.

Cohn, J.P. (1998). Understanding Sea Otters. Bioscience *48*, 151–155.

da Costa, J.P., Vitorino, R., Silva, G.M., Vogel, C., Duarte, A.C., and Rocha-Santos, T. (2016). A synopsis on aging—Theories, mechanisms and future prospects. Ageing Res. Rev. *29*, 90–112.

Cowley, M.J., Pinese, M., Kassahn, K.S., Waddell, N., Pearson, J. V., Grimmond, S.M., Biankin, A. V., Hautaniemi, S., and Wu, J. (2012). PINA v2.0: Mining interactome modules. Nucleic Acids Res. *40*.

Csárdi, G., and Nepusz, T. (2006). The igraph software package for complex network research. InterJournal Complex Syst. *1695*, 1–9.

Csete, M.E., and Doyle, J.C. (2002). Reverse engineering of biological complexity. Science (80-.). *295*, 1664–1669.

Cunningham, D., Atkin, W., Lenz, H.-J., Lynch, H.T., Minsky, B., Nordlinger, B., and Starling, N. (2010). Colorectal cancer. Lancet *375*, 1030–1047.

Dagogo-Jack, I., and Shaw, A.T. (2017). Tumour heterogeneity and resistance to cancer therapies. Nat. Rev. Clin. Oncol. *15*, 81–94.

Daily, G.C., Ehrlich, P.R., and Haddad, N.M. (1993). Double keystone bird in a keystone species complex. Proc. Natl. Acad. Sci. U. S. A. *90*, 592–594.

Daub, C.O., Steuer, R., Selbig, J., and Kloska, S. (2004). Estimating mutual information using B-spline functions--an improved similarity measure for analysing gene expression data. BMC Bioinformatics *5*, 118.

Dhillon, A.S., Hagan, S., Rath, O., and Kolch, W. (2007). MAP kinase signalling pathways in cancer. Oncogene *26*, 3279–3290.

Dijkstra, E.W. (1959). A note on two problems in connexion with graphs. Numer. Math. *1*, 269–271.

Doroszuk, A., Jonker, M.J., Pul, N., Breit, T.M., and Zwaan, B.J. (2012). Transcriptome analysis of a long-lived natural Drosophila variant: a prominent role of stress- and reproduction-genes in lifespan extension. BMC Genomics *13*, 167.

Drew, L. (2016). Pharmacogenetics: The right drug for you. Nature *537*, S60–S62.

Dunne, J.A., Williams, R.J., and Martinez, N.D. (2002). Network structure and biodiversity loss in food webs: robustness increases with connectance. Ecol. Lett. *5*, 558–567.

El-Brolosy, M.A., and Stainier, D.Y.R. (2017). Genetic compensation: A phenomenon in search of mechanisms. PLoS Genet. *13*, 1–17.

Ellson, J., Gansner, E.R., Koutsofios, E., North, S.C., and Woodhull, G. (2004). Graphviz and Dynagraph — Static and Dynamic Graph Drawing Tools. 127–148.

Emamjomeh, A., Saboori Robat, E., Zahiri, J., Solouki, M., and Khosravi, P. (2017). Gene co-expression network reconstruction: a review on computational methods for inferring functional information from plant-based expression data. Plant Biotechnol. Rep. *11*, 71–86.

Erdős, P., and Rényi, A. (1959). On Random Graphs I. Publ. Math. *6*, 290–297.

Espinoza, I., and Miele, L. (2013). Deadly crosstalk: Notch signaling at the intersection of EMT and cancer stem cells. Cancer Lett. *341*, 41–45.

Estrada, E. (2007). Topological structural classes of complex networks. Phys. Rev. E - Stat. Nonlinear, Soft Matter Phys. *75*, 1–12.

Everett, M.G., and Borgatti, S.P. (2005). Extending Centrality. In Models and Methods in Social Network Analysis, P.J. Carrington, J. Scott, and S. Wasserman, eds. (Cambridge: Cambridge University Press), pp. 57–76.

Fisher, R., Pusztai, L., and Swanton, C. (2014). Cancer heterogeneity: Implications for targeted therapeutics. Nature *509*, 479–485.

Floyd, R.W. (1962). Algorithm 97: Shortest path. Commun. ACM *5*, 345.

Fortuna, M.A., Stouffer, D.B., Olesen, J.M., Jordano, P., Mouillot, D., Krasnov, B.R., Poulin, R., and Bascompte, J. (2010). Nestedness versus modularity in ecological networks: two sides of the same coin? J. Anim. Ecol. *79*, 811–817.

Fouad, Y.A., and Aanei, C. (2017). Revisiting the hallmarks of cancer. Am. J. Cancer Res. *7*, 1016–1036.

Fox, J. (2005). The R Commander: A Basic-Statistics Graphical User Interface to R. J. Stat. Softw. *14*, 1–42.

Frenk, S., and Houseley, J. (2018). Gene expression hallmarks of cellular ageing. Biogerontology.

Fruchterman, T.M.J., and Reingold, E.M. (1991). Graph drawing by force-directed placement. Softw. Pract. Exp. *21*, 1129–1164.

Füssel, H.-M., and Klein, R.J.T. (2006). Climate Change Vulnerability Assessments: An Evolution of Conceptual Thinking. Clim. Change *75*, 301–329.

Gervaz, P., Cerottini, J.-P., Bouzourene, H., Hahnloser, D., Doan, C.L., Benhattar, J., Chaubert, P., Secic, M., Gillet, M., and Carethers, J.M. (2002). Comparison of microsatellite instability and chromosomal instability in predicting survival of patients with T3N0 colorectal cancer. Surgery *131*, 190–197.

Girardot, F., Lasbleiz, C., Monnier, V., and Tricoire, H. (2006). Specific age related signatures in Drosophila body parts transcriptome. BMC Genomics *7*, 69.

Goh, K.-I., Cusick, M.E., Valle, D., Childs, B., Vidal, M., and Barabási, A.-L. (2007). The human disease network. Proc. Natl. Acad. Sci. U. S. A. *104*, 8685–8690.

González, J., Ortiz, M., Rodríguez-Zaragoza, F., and Ulanowicz, R.E. (2016). Assessment of long-term changes of ecosystem indexes in Tongoy Bay (SE Pacific coast): Based on trophic network analysis. Ecol. Indic. *69*, 390–399.

Gramates, L.S., Marygold, S.J., Santos, G. dos, Urbano, J.-M., Antonazzo, G., Matthews, B.B., Rey, A.J., Tabone, C.J., Crosby, M.A., Emmert, D.B., et al. (2017). FlyBase at 25:

looking to the future. Nucleic Acids Res. *45*, D663–D671.

Graveley, B.R., Brooks, A.N., Carlson, J.W., Duff, M.O., Landolin, J.M., Yang, L., Artieri, C.G., van Baren, M.J., Boley, N., Booth, B.W., et al. (2011). The developmental transcriptome of Drosophila melanogaster. Nature *471*, 473–479.

Gunderson, L.H. Ecological Resilience--In Theory and Application. Annu. Rev. Ecol. Syst. *31*, 425–439.

Habib, M., and Paul, C. (2010). A survey of the algorithmic aspects of modular decomposition. Comput. Sci. Rev. *4*, 41–59.

Hanahan, D., and Weinberg, R.A. (2000). The Hallmarks of Cancer. Cell *100*, 57–70.

Hanahan, D., and Weinberg, R.A. (2011). Hallmarks of Cancer: The Next Generation. Cell *144*, 646–674.

Harary, F. (1994). Graph theory (Addison-Wesley Publishing Company).

Harris, S.E., Riggio, V., Evenden, L., Gilchrist, T., McCafferty, S., Murphy, L., Wrobel, N., Taylor, A.M., Corley, J., Pattie, A., et al. (2017). Age-related gene expression changes and transcriptome wide association study of physical and cognitive aging traits in the Lothian Birth Cohort 1936. Aging (Albany. NY). *9*, 2489–2503.

Hartwell, L.H., Hopfield, J.J., Leibler, S., and Murray, A.W. (1999). From molecular to modular cell biology. Nature *402*, C47–C52.

Hastings, A. (2010). Timescales, dynamics, and ecological understanding. Ecology *91*, 3471–3480.

Haustead, D.J., Stevenson, A., Saxena, V., Marriage, F., Firth, M., Silla, R., Martin, L., Adcroft, K.F., Rea, S., Day, P.J., et al. (2016). Transcriptome analysis of human ageing in male skin shows mid-life period of variability and central role of NF-κB. Sci. Rep. *6*, 26846.

Hecker, N., Stephan, C., Mollenkopf, H.-J., Jung, K., Preissner, R., and Meyer, H.-A. (2013). A New Algorithm for Integrated Analysis of miRNA-mRNA Interactions Based

on Individual Classification Reveals Insights into Bladder Cancer. PLoS One *8*, e64543.

Hipskind, R.A., Roa, V.N., Muller, C.G.F., Raddy, E.S.P., and Nordheim, A. (1991). Ets-related protein Elk-1 is homologous to the c-fos regulatory factor p62TCF. Nature *354*, 531–534.

Hoadley, K.A., Yau, C., Hinoue, T., Wolf, D.M., Lazar, A.J., Drill, E., Shen, R., Taylor, A.M., Cherniack, A.D., Thorsson, V., et al. (2018). Cell-of-Origin Patterns Dominate the Molecular Classification of 10,000 Tumors from 33 Types of Cancer. Cell *173*, 291–304.e6.

Hodson, R. (2016). Precision medicine. Nature *537*, S49.

Hu, Y., Pan, J., Xin, Y., Mi, X., Wang, J., Gao, Q., and Luo, H. (2018). Gene Expression Analysis Reveals Novel Gene Signatures Between Young and Old Adults in Human Prefrontal Cortex. Front. Aging Neurosci. *10*, 259.

Huang, D.W., Sherman, B.T., and Lempicki, R.A. (2009). Systematic and integrative analysis of large gene lists using DAVID bioinformatics resources. Nat. Protoc. *4*, 44–57.

Huang, K., Zhang, J.X., Han, L., You, Y.P., Jiang, T., Pu, P.Y., and Kang, C.S. (2010). MicroRNA roles in beta-catenin pathway. Mol. Cancer *9*, 252.

Huang, T., Zhang, J., Xie, L., Dong, X., Zhang, L., Cai, Y.-D., and Li, Y.-X. (2011). Crosstissue Coexpression Network of Aging. Omi. A J. Integr. Biol. *15*, 665–671.

Hucka, M., Finney, A., Sauro, H.M., Bolouri, H., Doyle, J.C., Kitano, H., and the rest of the SBML Forum:, A.P., Arkin, A.P., Bornstein, B.J., Bray, D., et al. (2003). The systems biology markup language (SBML): a medium for representation and exchange of biochemical network models. Bioinformatics *19*, 524–531.

Huntzinger, E., and Izaurralde, E. (2011). Gene silencing by microRNAs: Contributions of translational repression and mRNA decay. Nat. Rev. Genet. *12*, 99–110.

Javelaud, D., and Mauviel, A. (2005). Crosstalk mechanisms between the mitogen-

activated protein kinase pathways and Smad signaling downstream of TGF-β: Implications for carcinogenesis. Oncogene *24*, 5742–5750.

Jensen, S.A., Vainer, B., Kruhøffer, M., and Sørensen, J.B. (2009). Microsatellite instability in colorectal cancer and association with thymidylate synthase and dihydropyrimidine dehydrogenase expression. BMC Cancer *9*, 25.

Jeong, H., Mason, S.P., Barabási, A.L., and Oltvai, Z.N. (2001). Lethality and centrality in protein networks. Nature *411*, 41–42.

Jiang, W., Chen, X., Liao, M., Li, W., Lian, B., Wang, L., Meng, F., Liu, X., Chen, X., Jin, Y., et al. (2012). Identification of links between small molecules and miRNAs in human cancers based on transcriptional responses. Sci. Rep. *2*, 1–8.

Jones, C.G., Lawton, J.H., and Shachak, M. (1994). Organisms as Ecosystem Engineers. Oikos *69*, 373.

Jordán, F. (2009). Keystone species and food webs. Philos. Trans. R. Soc. Lond. B. Biol. Sci. *364*, 1733–1741.

Jordán, F., and Scheuring, I. (2004). Network ecology: Topological constraints on ecosystem dynamics. Phys. Life Rev. *1*, 139–172.

Jordán, F., Liu, W.-C., and van Veen, J.F. (2005). Quantifying the importance of species and their interactions in a host-parasitoid community. Community Ecol. *4*, 79–88.

Jordán, F., Okey, T.A., Bauer, B., and Libralato, S. (2008). Identifying important species: Linking structure and function in ecological networks. Ecol. Modell. *216*, 75–80.

Jordán, F., Liu, W., Davis, A.J., Memmott, J., Oikos, S., Mar, F., Jordan, F., Davis, W., and Topological, A.J. (2014). Topological Keystone Species : Measures of Positional Importance in Food Webs in of positional Topological keystone species : measures importance food webs. *112*, 535–546.

Kamei, J., Ito, H., Aizawa, N., Hotta, H., Kojima, T., Fujita, Y., Ito, M., Homma, Y., and Igawa, Y. (2018). Age-related changes in function and gene expression of the male and

female mouse bladder. Sci. Rep. *8*, 2089.

Kanehisa, M., and Goto, S. (2000). KEGG: Kyoto Encyclopedia of Genes and Genomes.

Kapushesky, M., Adamusiak, T., Burdett, T., Culhane, A., Farne, A., Filippov, A., Holloway, E., Klebanov, A., Kryvych, N., Kurbatova, N., et al. (2012). Gene Expression Atlas update - Value-added database of microarray and sequencing-based functional genomics experiments. Nucleic Acids Res. *40*, D1077–D1081.

Kelt, D.A. (1997). Review: Nestedness Temperature Calculator. Bull. Ecol. Soc. Am. *78*, 63–65.

Kent, O.A., Chivukula, R.R., Mullendore, M., Wentzel, E.A., Feldmann, G., Lee, K.H., Liu, S., Leach, S.D., Maitra, A., and Mendell, J.T. (2010). Repression of the miR-143/145 cluster by oncogenic Ras initiates a tumor-promoting feed-forward pathway. Genes Dev. *24*, 2754–2759.

Kenyon, C.J. (2010). The genetics of ageing. Nature *464*, 504–512.

Kim, V.N., and Nam, J.W. (2006). Genomics of microRNA. Trends Genet. *22*, 165–173.

Kim, S., Jo, Y., Webster, M.J., and Lee, D. (2018). Shared co-expression networks in frontal cortex of the normal aged brain and schizophrenia. Schizophr. Res.

Kin Chan, S.S. (2013). What is a Master Regulator? J. Stem Cell Res. Ther. *03*.

Kitano, H. (2002). Systems biology: A brief overview. Science (80-.). *295*, 1662–1664.

Kluyver, T., Ragan-kelley, B., Pérez, F., Granger, B., Bussonnier, M., Frederic, J., Kelley, K., Hamrick, J., Grout, J., Corlay, S., et al. (2016). Jupyter Notebooks—a publishing format for reproducible computational workflows. Position. Power Acad. Publ. Play. Agents Agendas 87–90.

Kobayashi, M., Honma, T., Matsuda, Y., Suzuki, Y., Narisawa, R., Ajioka, Y., and Asakura, H. (2000). Nuclear translocation of beta-catenin in colorectal cancer. Br. J. Cancer *82*, 1689–1693.

Krebs, V. (2002). Mapping Networks of Terrorist Cells. Connections *24*, 43–52.

Langfelder, P., and Horvath, S. (2007). Eigengene networks for studying the relationships between co-expression modules. BMC Syst. Biol. *1*, 54.

Langfelder, P., and Horvath, S. (2008). WGCNA : an R package for weighted correlation network analysis.

Langfelder, P., Mischel, P.S., and Horvath, S. (2013). When Is Hub Gene Selection Better than Standard Meta-Analysis? PLoS One *8*.

Lawton, J.H., and May, R.M. (1996). Extinction Rates. J. Evol. Biol. *9*, 124–126.

Levy, S.E., and Myers, R.M. (2016). Advancements in Next-Generation Sequencing. Annu. Rev. Genomics Hum. Genet. *17*, 95–115.

Li, J., and Zhao, P.X. (2016). Mining Functional Modules in Heterogeneous Biological Networks Using Multiplex PageRank Approach. Front. Plant Sci. *7*, 1–11.

Li, S., Armstrong, C.M., Bertin, N., Ge, H., Milstein, S., Boxem, M., Vidalain, P.O., Han, J.D.J., Chesneau, A., Hao, T., et al. (2004). A Map of the Interactome Network of the Metazoan C. elegans. Science (80-.). *303*, 540–543.

Li, Y., Qiu, C., Tu, J., Geng, B., Yang, J., Jiang, T., and Cui, Q. (2014). HMDD v2.0: a database for experimentally supported human microRNA and disease associations. Nucleic Acids Res. *42*, D1070–D1074.

Li, Y., Pearl, S.A., and Jackson, S.A. (2015). Gene Networks in Plant Biology: Approaches in Reconstruction and Analysis. Trends Plant Sci. *20*, 664–675.

Liang, H., and Li, W.-H. (2007). MicroRNA regulation of human protein protein interaction network. Rna *13*, 1402–1408.

Lindlöf, A., and Lubovac, Z. (2005). Simulations of simple artificial genetic networks reveal features in the use of Relevance Networks. In Silico Biol. *5*, 239–249.

Liseron-Monfils, C., and Ware, D. (2015). Revealing gene regulation and associations

through biological networks. Curr. Plant Biol. *3–4*, 30–39.

Livi, C.M., Jordán, F., Lecca, P., and Okey, T.A. (2011). Identifying key species in ecosystems with stochastic sensitivity analysis. Ecol. Modell. *222*, 2542–2551.

López-Otín, C., Blasco, M.A., Partridge, L., Serrano, M., and Kroemer, G. (2013). The hallmarks of aging. Cell *153*.

Lu, T.P., Lee, C.Y., Tsai, M.H., Chiu, Y.C., Hsiao, C.K., Lai, L.C., and Chuang, E.Y. (2012). MiRSystem: An integrated system for characterizing enriched functions and pathways of microRNA targets. PLoS One *7*, e42390.

Margolin, A.A., Nemenman, I., Basso, K., Wiggins, C., Stolovitzky, G., Favera, R., and Califano, A. (2006). ARACNE: An Algorithm for the Reconstruction of Gene Regulatory Networks in a Mammalian Cellular Context. BMC Bioinformatics *7*, S7.

Markowitz, S.D., and Bertagnolli, M.M. (2009). Molecular Basis of Colorectal Cancer. N. Engl. J. Med. *361*, 2449–2460.

May, R.M., Beddington, J.R., Clark, C.W., Holt, S.J., and Laws, R.M. (1979). Management of Multispecies Fisheries. Science (80-.). *205*, 267–277.

Mazza, T., Romanel, A., and Jordán, F. (2010). Estimating the divisibility of complex biological networks by sparseness indices. Brief. Bioinform. *11*, 364–374.

Mazzoccoli, G., Tomanin, R., Mazza, T., D'Avanzo, F., Salvalaio, M., Rigon, L., Zanetti, A., Pazienza, V., Francavilla, M., Giuliani, F., et al. (2013). Circadian transcriptome analysis in human fibroblasts from Hunter syndrome and impact of iduronate-2-sulfatase treatment. BMC Med. Genomics *6*, 37.

Mazzoccoli, G., Colangelo, T., Panza, A., Rubino, R., Tiberio, C., Palumbo, O., Carella, M., Trombetta, D., Gentile, A., Tavano, F., et al. (2014). Analysis of clock gene-miRNA correlation networks reveals candidate drivers in colorectal cancer. Oncotarget *7*.

McCarroll, S.A., Murphy, C.T., Zou, S., Pletcher, S.D., Chin, C.S., Jan, Y.N., Kenyon, C., Bargmann, C.I., and Li, H. (2004). Comparing genomic expression patterns across

species identifies shared transcriptional profile in aging. Nat. Genet. *36*, 197–204.

Medina, I., Carbonell, J., Pulido, L., Madeira, S.C., Goetz, S., Conesa, A., Tárraga, J., Pascual-Montano, A., Nogales-Cadenas, R., Santoyo, J., et al. (2010). Babelomics: An integrative platform for the analysis of transcriptomics, proteomics and genomic data with advanced functional profiling. Nucleic Acids Res. *38*, W210–W213.

Menge, B.A. (1995). Indirect effects in marine rocky intertidal interaction webs: Patterns and importance. Ecol. Monogr. *65*, 21–74.

Mezlini, A.M., Wang, B., Deshwar, A., Morris, Q., and Goldenberg, A. (2013). Identifying Cancer Specific Functionally Relevant miRNAs from Gene Expression and miRNA-to-Gene Networks Using Regularized Regression. PLoS One *8*, e73168.

Mills, L.S., and Doak, D.F. (1993). The Keystone-Species Concept in Ecology and Conservation. Bioscience *43*, 219–224.

Mogilyansky, E., and Rigoutsos, I. (2013). The miR-17/92 cluster: a comprehensive update on its genomics, genetics, functions and increasingly important and numerous roles in health and disease. Cell Death Differ. *20*, 1603–1614.

Mostafavi, S., Ray, D., Warde-Farley, D., Grouios, C., and Morris, Q. (2008). GeneMANIA: a real-time multiple association network integration algorithm for predicting gene function. Genome Biol. *9 Suppl 1*, S4.

Mumby, P.J., Steneck, R.S., and Hastings, A. (2013). Evidence for and against the existence of alternate attractors on coral reefs. Oikos *122*, 481–491.

Mumby, P.J., Chollett, I., Bozec, Y.-M., and Wolff, N.H. (2014). Ecological resilience, robustness and vulnerability: how do these concepts benefit ecosystem management? Curr. Opin. Environ. Sustain. *7*, 22–27.

Muzny, D., Bainbridge, M., Chang, K., Dinh, H., Drummond, J., Fowler, G., Kovar, C., Lewis, L., Morgan, M., Newsham, I., et al. (2012). Comprehensive molecular characterization of human colon and rectal cancer. Nature *487*, 330–337.

Nepusz, T., Yu, H., and Paccanaro, A. (2012). Detecting overlapping protein complexes in protein-protein interaction networks. Nat. Methods *9*, 471–472.

Newman, M.E.J. (2006). Finding community structure in networks using the eigenvectors of matrices. Phys. Rev. E - Stat. Nonlinear, Soft Matter Phys. *74*, 036104.

Olive, V., Jiang, I., and He, L. (2010). mir-17-92, a cluster of miRNAs in the midst of the cancer network. Int. J. Biochem. Cell Biol. *42*, 1348–1354.

Ortiz, M., Levins, R., Campos, L., Berrios, F., Campos, F., Jordán, F., Hermosillo, B., Gonzalez, J., and Rodriguez, F. (2013). Identifying keystone trophic groups in benthic ecosystems: Implications for fisheries management. Ecol. Indic. *25*, 133–140.

Ortiz, M., Rodriguez-Zaragoza, F., Hermosillo-Nuñez, B., and Jordán, F. (2015). Control strategy scenarios for the alien lionfish Pterois volitans in Chinchorro bank (Mexican Caribbean): Based on semi-quantitative loop analysis. PLoS One *10*, e0130261.

Ortiz, M., Hermosillo-Nuñez, B., González, J., Rodríguez-Zaragoza, F., Gómez, I., and Jordán, F. (2017). Quantifying keystone species complexes: Ecosystem-based conservation management in the King George Island (Antarctic Peninsula). Ecol. Indic. *81*, 453–460.

Page, L., Page, L., Brin, S., Motwani, R., and Winograd, T. (1998). The PageRank Citation Ranking: Bringing Order to the Web.

Pagliuca, A., Valvo, C., Fabrizi, E., Di Martino, S., Biffoni, M., Runci, D., Forte, S., De Maria, R., and Ricci-Vitiani, L. (2013). Analysis of the combined action of miR-143 and miR-145 on oncogenic pathways in colorectal cancer cells reveals a coordinate program of gene repression. Oncogene *32*, 4806–4813.

Paine, R.T. (1969). A Note on Trophic Complexity and Community Stability. Am. Nat. *103*, 91–93.

Pavlopoulos, G.A., Secrier, M., Moschopoulos, C.N., Soldatos, T.G., Kossida, S., Aerts, J., Schneider, R., and Bagos, P.G. (2011). Using graph theory to analyze biological networks. BioData Min. *4*.

Pereira, J., and Jordán, F. (2017). Multi-node selection of patches for protecting habitat connectivity: Fragmentation versus reachability. Ecol. Indic. *81*, 192–200.

Pereira, J., Saura, S., and Jordán, F. (2017). Single-node vs. multi-node centrality in landscape graph analysis: key habitat patches and their protection for 20 bird species in NE Spain. Methods Ecol. Evol. *8*, 1458–1467.

Pérez, F., and Granger, B.E. (2007). IPython: A System for Interactive Scientific Computing Python: An Open and General- Purpose Environment. Comput. Sci. Eng. *9*, 21–29.

Phipps, A.I., Buchanan, D.D., Makar, K.W., Win, A.K., Baron, J.A., Lindor, N.M., Potter, J.D., and Newcomb, P.A. (2013). KRAS-mutation status in relation to colorectal cancer survival: the joint impact of correlated tumour markers. Br. J. Cancer *108*, 1757–1764.

Piepoli, A., Tavano, F., Copetti, M., Mazza, T., Palumbo, O., Panza, A., di Mola, F.F., Pazienza, V., Mazzoccoli, G., Biscaglia, G., et al. (2012). Mirna Expression Profiles Identify Drivers in Colorectal and Pancreatic Cancers. PLoS One *7*, e33663.

Podani, J., and Schmera, D. (2011). A new conceptual and methodological framework for exploring and explaining pattern in presence - absence data. Oikos *120*, 1625–1638.

Podani, J., Ricotta, C., and Schmera, D. (2013). A general framework for analyzing beta diversity, nestedness and related community-level phenomena based on abundance data. Ecol. Complex. *15*, 52–61.

Polakis, P. (2000). Wnt signaling and cancer. Genes Dev. *14*, 1837–1851.

Pons, P., and Latapy, M. (2006). Computing Communities in Large Networks Using Random Walks. J. Graph Algorithms Appl. *10*, 191–218.

Potters, G. (2010). Systems Biology of the Cell.

Power, M.E., Tilman, D., Estes, J.A., Menge, B.A., Bond, W.J., Mills, L.S., Daily, G., Castilla, J.C., Lubchenco, J., and Paine, R.T. (1996). Challenges in the Quest for

Keystones. Bioscience *46*, 609–620.

Prieto, C., and De Las Rivas, J. (2006). APID: Agile Protein Interaction DataAnalyzer. Nucleic Acids Res. *34*, W298-302.

Priness, I., Maimon, O., and Ben-Gal, I. (2007). Evaluation of gene-expression clustering via mutual information distance measure. BMC Bioinformatics *8*, 111.

Pritchard, C.C., and Grady, W.M. (2011). Colorectal cancer molecular biology moves into clinical practice. Gut *60*, 116–129.

Purdy, K.J., Hurd, P.J., Moya-Laraño, J., Trimmer, M., Oakley, B.B., and Woodward, G. (2010). Systems Biology for Ecology. pp. 87–149.

Randic, M. (1997). Dense Graphs and Sparse Matrices. J. Chem. Inf. Model. *37*, 1078–1081.

Ravasz, E., Somera, A.L., Mongru, D.A., and Oltvai, Z.N. (2002). Hierarchical Organization of Modularity in Metabolic Networks. *297*, 1551–1555.

Reingold, E.M., and Tilford, J.S. (1981). Tidier Drawings of Trees. IEEE Trans. Softw. Eng. *SE-7*, 223–228.

Revell, L.J. APPLICATION phytools: an R package for phylogenetic comparative biology (and other things).

Roberts, P.J., and Der, C.J. (2007). Targeting the Raf-MEK-ERK mitogen-activated protein kinase cascade for the treatment of cancer. Oncogene *26*, 3291–3310.

Robinson, M.D., McCarthy, D.J., and Smyth, G.K. (2010). edgeR: a Bioconductor package for differential expression analysis of digital gene expression data. Bioinformatics *26*, 139–140.

Rosvall, M., and Bergstrom, C.T. (2007). Maps of random walks on complex networks reveal community structure. *105*.

Rubio, L., Bodin, Ö., Brotons, L., and Saura, S. (2015). Connectivity conservation

priorities for individual patches evaluated in the present landscape: How durable and effective are they in the long term? Ecography (Cop.). *38*, 782–791.

Santarpia, L., Lippman, S.M., and El-Naggar, A.K. (2012). Targeting the MAPK–RAS–RAF signaling pathway in cancer therapy. Expert Opin. Ther. Targets *16*, 103–119.

Saridaki, Z., Souglakos, J., and Georgoulias, V. (2014). Prognostic and predictive significance of MSI in stages II/III colon cancer. World J. Gastroenterol. *20*, 6809–6814.

Scheffer, M., and Carpenter, S.R. (2003). Catastrophic regime shifts in ecosystems: linking theory to observation. Trends Ecol. Evol. *18*, 648–656.

Scott, J., Wasserman, S., Faust, K., and Galaskiewicz, J. (1996). Social Network Analysis: Methods and Applications. Br. J. Sociol. *47*, 375.

Segal, E., Shapira, M., Regev, A., Pe'er, D., Botstein, D., Koller, D., and Friedman, N. (2003). Module networks: Identifying regulatory modules and their condition-specific regulators from gene expression data. Nat. Genet. *34*, 166–176.

Seim, I., Ma, S., and Gladyshev, V.N. (2016). Gene expression signatures of human cell and tissue longevity. Npj Aging Mech. Dis. *2*, 16014.

Shannon, P., Markiel, A., Ozier, O., Baliga, N.S., Wang, J.T., Ramage, D., Amin, N., Schwikowski, B., and Ideker, T. (2003). Cytoscape: A software Environment for integrated models of biomolecular interaction networks. Genome Res. *13*, 2498–2504.

da Silveira, W., Renaud, L., Simpson, J., Glen, W., Hazard, E., Chung, D., Hardiman, G., da Silveira, W.A., Renaud, L., Simpson, J., et al. (2018). miRmapper: A Tool for Interpretation of miRNA–mRNA Interaction Networks. Genes (Basel). *9*, 458.

Skiena, S. (1990). Implementing discrete mathematics combinatorics and graph theory with Mathematica (Cambridge University Press).

Smuts, J.C., and Holst, S. (1926). Holism and evolution : the original source of the holistic approach to life (Sierra Sunrise Books).

Song, L., Langfelder, P., and Horvath, S. (2012). Comparison of co-expression measures:

mutual information, correlation, and model based indices. BMC Bioinformatics *13*, 328.

Sottoriva, A., Kang, H., Ma, Z., Graham, T.A., Salomon, M.P., Zhao, J., Marjoram, P., Siegmund, K., Press, M.F., Shibata, D., et al. (2015). A Big Bang model of human colorectal tumor growth. Nat Genet *47*, 209–216.

Steuer, R., Kurths, J., Daub, C.O., Weise, J., and Selbig, J. (2002). The mutual information: detecting and evaluating dependencies between variables. Bioinformatics *18 Suppl 2*, S231-40.

Stewart, B.W., and Wild, C.P. (2014). World Cancer Report 2014.

Supek, F., Bošnjak, M., Škunca, N., and Šmuc, T. (2011). REVIGO Summarizes and Visualizes Long Lists of Gene Ontology Terms. PLoS One *6*, e21800.

Swindell, W.R. (2009). Accelerated failure time models provide a useful statistical framework for aging research. Exp. Gerontol. *44*, 190–200.

Sylvestre, Y., De Guire, V., Querido, E., Mukhopadhyay, U.K., Bourdeau, V., Major, F., Ferbeyre, G., and Chartrand, P. (2007). An E2F/miR-20a autoregulatory feedback loop. J. Biol. Chem. *282*, 2135–2143.

Szklarczyk, D., Franceschini, A., Wyder, S., Forslund, K., Heller, D., Huerta-Cepas, J., Simonovic, M., Roth, A., Santos, A., Tsafou, K.P., et al. (2015). STRING v10: Protein-protein interaction networks, integrated over the tree of life. Nucleic Acids Res. *43*, D447–D452.

Tarafa, G., Villanueva, A., Farré, L., Rodríguez, J., Musulén, E., Reyes, G., Seminago, R., Olmedo, E., Paules, A.B., Peinado, M.A., et al. (2000). DCC and SMAD4 alterations in human colorectal and pancreatic tumor dissemination. Oncogene *19*, 546–555.

Terborgh, J. (1999). Requiem for Nature. Isl. Press *31*, 55–57.

Thiagalingam, S. (2006). A cascade of modules of a network defines cancer progression. Cancer Res. *66*, 7379–7385.

Timon McPhearson, P. (2003). The Importance of Species: Perspectives on

Expendability and Triage.

Tomczak, K., Czerwińska, P., and Wiznerowicz, M. (2015). The Cancer Genome Atlas (TCGA): An immeasurable source of knowledge. Wspolczesna Onkol. *1A*, A68–A77.

Towlson, E.K., Vertes, P.E., Ahnert, S.E., Schafer, W.R., and Bullmore, E.T. (2013). The Rich Club of the C. elegans Neuronal Connectome. J. Neurosci. *33*, 6380–6387.

Trapnell, C., Pachter, L., and Salzberg, S.L. (2009). TopHat: discovering splice junctions with RNA-Seq. Bioinformatics *25*, 1105–1111.

Trewavas, A. (2006). A Brief History of Systems Biology: "Every object that biology studies is a system of systems." Francois Jacob (1974). Plant Cell Online *18*, 2420–2430.

Türei, D., Korcsmáros, T., and Saez-Rodriguez, J. (2016). OmniPath: Guidelines and gateway for literature-curated signaling pathway resources. Nat. Methods *13*, 966–967.

Turner, B.L., Kasperson, R.E., Matson, P.A., McCarthy, J.J., Corell, R.W., Christensen, L., Eckley, N., Kasperson, J.X., Luers, A., Martello, M.L., et al. (2003). A framework for sustainability science: A renovated IPAT identity. PNAS *99*, 7860–7865.

Venter, J.C., Adams, M.D., Myers, E.W., Li, P.W., Mural, R.J., Sutton, G.G., Smith, H.O., Yandell, M., Evans, C. a, Holt, R. a, et al. (2001). The sequence of the human genome. Science *291*, 1304–1351.

Del Vicario, M., Bessi, A., Zollo, F., Petroni, F., Scala, A., Caldarelli, G., Stanley, H.E., and Quattrociocchi, W. (2016). The spreading of misinformation online. Proc. Natl. Acad. Sci. 201517441.

Del Vicario, M., Scala, A., Caldarelli, G., Stanley, H.E., and Quattrociocchi, W. (2017). Modeling confirmation bias and polarization. Sci. Rep. *7*, 40391.

De Vos, J.M., Joppa, L.N., Gittleman, J.L., Stephens, P.R., and Pimm, S.L. (2015). Estimating the normal background rate of species extinction. Conserv. Biol. *29*, 452–462.

W. Fox, J. (2006). Current food web models cannot explain the overall topological structure of observed food webs. Oikos *115*, 97–109.

Watts, D.J., and Strogatz, S.H. (1998). Collective dynamics of “small-world” networks. Nature *393*, 440–442.

Westerhoff, H. V, and Palsson, B.O. (2004). The evolution of molecular biology into systems biology. Nat. Biotechnol. *22*, 1249–1252.

White, J.G., Southgate, E., Thomson, J.N., and Brenner, S. (1986). The structure of the nervous system of the nematode Caenorhabditis elegans. Philos. Trans. R. Soc. Lond. B. Biol. Sci. *314*, 1–340.

Williams, R.J., and Martinez, N.D. (2000). Simple rules yield complex food webs. Nature *404*, 180–183.

Wood, S.H., Craig, T., Li, Y., Merry, B., and De Magalhães, J.P. (2013). Whole transcriptome sequencing of the aging rat brain reveals dynamic RNA changes in the dark matter of the genome. Age (Omaha). *35*, 763–776.

Woods, K., Thomson, J.M., and Hammond, S.M. (2007). Direct Regulation of an Oncogenic Micro-RNA Cluster by E2F Transcription Factors. J. Biol. Chem. *282*, 2130–2134.

Wootton, J.T. (1994). The Nature and Consequences of Indirect Effects in Ecological Communities. Annu. Rev. Ecol. Syst. *25*, 443–466.

Wright, C.M., Dent, O.F., Newland, R.C., Barker, M., Chapuis, P.H., Bokey, E.L., Young, J.P., Leggett, B.A., Jass, J.R., and Macdonald, G.A. (2005). Low level microsatellite instability may be associated with reduced cancer specific survival in sporadic stage C colorectal carcinoma. Gut *54*, 103–108.

Wu, G., and Stein, L. (2012). A network module-based method for identifying cancer prognostic signatures. Genome Biol. *13*, R112.

Wu, J., Irizarry, R., Macdonald, J., and Gentry, J. (2005). Background adjustment using sequence information. R Packag. Version *2*.

Wysocki, K., and Ritter, L. (2011). Diseasome *An Approach to Understanding Gene–*

Disease Interactions. Annu. Rev. Nurs. Res. *29*, 55–72.

Xie, M., Chen, H., Huang, L., O'Neil, R.C., Shokhirev, M.N., and Ecker, J.R. (2018). Author Correction: A B-ARR-mediated cytokinin transcriptional network directs hormone cross-regulation and shoot development (Nature Communications I2018) DOI: 10.1038/s41467-018-03921-6). Nat. Commun. *9*, 1604.

Xu, D., Woodfield, S.E., Lee, T. V, Fan, Y., Antonio, C., and Bergmann, A. (2009). Genetic control of programmed cell death (apoptosis) in Drosophila. Fly (Austin). *3*, 78–90.

Yang, Q., Pan, W., and Qian, L. (2017). Identification of the miRNA–mRNA regulatory network in multiple sclerosis. Neurol. Res. *39*, 142–151.

Ye, Y., Li, S.-L., and Wang, S.-Y. (2018). Construction and analysis of mRNA, miRNA, lncRNA, and TF regulatory networks reveal the key genes associated with prostate cancer. PLoS One *13*, e0198055.

Yip, A.M., and Horvath, S. (2007). Gene network interconnectedness and the generalized topological overlap measure. BMC Bioinformatics *14*, 1–14.

Yu, K.R., and Kang, K.S. (2013). Aging-related genes in mesenchymal stem cells: A mini-review. Gerontology *59*, 557–563.

Zhan, M., Yamaza, H., Sun, Y., Sinclair, J., Li, H., and Zou, S. (2007). Temporal and spatial transcriptional profiles of aging in Drosophila melanogaster. Genome Res. *17*, 1236–1243.

Zhang, B., and Horvath, S. (2005). A General Framework for Weighted Gene Co-Expression Network Analysis. Stat. Appl. Genet. Mol. Biol. *4*, Article17.

Zhou, X., Kao, M.-C.J., and Wong, W.H. (2002). Transitive functional annotation by shortest-path analysis of gene expression data. Proc. Natl. Acad. Sci. *99*, 12783–12788.

Acknowledgements

We are grateful to Christoph Gohlke, from the Laboratory for Fluorescence Dynamics, University of California, for providing Windows unofficial binaries of the iGraph Python extension package;

We thank Prof. Ferenc Jordán of the Danube Research Institute for its thoughtful comments and critics that allowed to ameliorate Pyntacle;

Finally, thanks to IRCSS Ospedale Casa Sollievo della Sofferenza for supporting this work.

Appendix - Excerpt of Pyntacle site material

Quick startup guide

In this brief tutorial, we will show you how to use Pyntacle to find *key player* nodes (the *kp-set*) through a network using the *key-player* metrics of *fragmentation* and *reachability*. *Fragmentation* is the effect of removing nodes on the communication and structure of a network. *Reachability* is the property of nodes to reach their direct or indirect neighbors in a network. Although we will provide here a brief explanation of these concepts, we recommend reading the Material and Methods section for detailed description of the *key player* metrics.

This guide will help using Pyntacle both from your command shell and as a Python library. All data used in this tutorial are available for download at http://pyntacle.css-mendel.it/resources/tutorials/startup_guide/startup_guide_data.zip.

1. Setting Pyntacle for the first use

After installing Pyntacle as described in Installation Instructions available at https://github.com/mazzalab/pyntacle, you can find the binary files by typing in your shell:

```
which pyntacle
```

For example, this is the location of the Pyntacle's binaries on a **Linux** Mint 18 system where Pyntacle was installed through the Conda distribution on the user's home directory:

```
/home/d.capocefalo/miniconda3/bin/pyntacle
```

Alternatively, you may run Pyntacle through our Docker Image or build a custom Pyntacle Docker Image by editing the Dockerfile provided on our website at http://pyntacle.css-mendel.it/resources/docker/pyntacle.dockerfile.
It is suggested to create a new Python virtual environment using the `virtualenv` tool or a Conda environment and install Pyntacle there. This will avoid any conflict among libraries.

If using Pyntacle as a Python library, typing:

```
import pyntacle
```

on a Python 3 shell will end with no error if Pyntacle was successfully installed.

2. Dataset description

The toy dataset is the network of advice-seeking ties among global consulting companies (also called in this tutorial the **AdvSeek network**). This network was already used in the original paper by Stephen P. Borgatti, in which Key Player metrics are introduced, Identifying sets of key players in a social network.

The network can is the following:

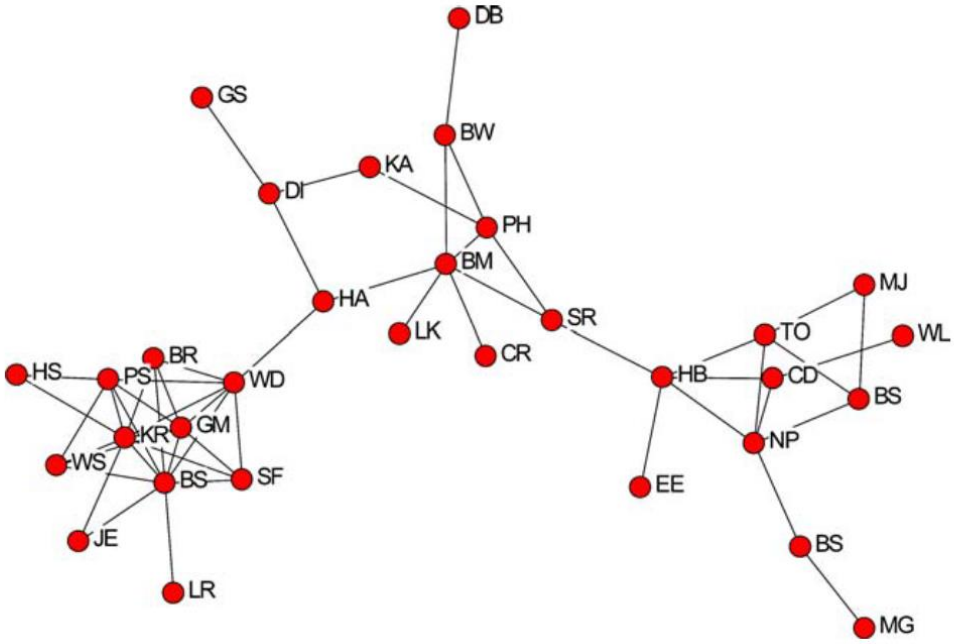

Figure 31: The AdvSeek Network used by Borgatti.

this network is available at the following link:

http://pyntacle.css-mendel.it/resources/tutorials/startup_guide/Figure_8.adjm as an adjacency matrix (see Materials and Methods, section 2.8). Nodes in the network are labeled with the initials of the consultants. Since some of the consultants share the same initials, we appended progressive numbers to their initials (e.g. *BS*, *BS2*, *BS3*, etc.) to be

compliant with the Pyntacle Minimum Requirements (see the Minimum Requirements section in Appendix 2). Edges represents relationships among consultants.

3. Command line Startup Guide

Testing the Pyntacle Command Line

To check that Pyntacle is properly installed and working, a set of unit tests can be run by typing in the command shell:

```
pyntacle test
```

Pyntacle will perform several operations that will end with a similar message no errors will be encountered.

```
Ran 23 tests in 1.002s

OK

<pyntacle.pyntacle.App object at 0x7f7c22f8be10>
```

Once verified the correct installation of Pyntacle, we replicated some of the results of Borgatti's original article (Borgatti, 2006) in two steps.

kp-info - Compute key-player metrics for a given set of nodes

As a first step, the Pyntacle `kp-info` module will be used to measure the *dF* metric (*fragmentation*) for a specific node set of the AdvSeek network. Borgatti measured the

dF value of the pair {HB, WD} and obtained a value of 0.817. We recall here that *dF* ranges from 0 to 1, when 0 means maximum connectedness (i.e., the network is a clique) and 1 means maximum disconnection (all nodes are isolates). This result can be replicated by typing:

```
pyntacle keyplayer kp-info -i Figure_8.adjm -t dF --nodes HB,WD
```

This command returns the following output on your shell:

```
Reading input file...

Adjacency Matrix from Figure_8.txt imported



Nodes given as input: ['HB', 'WD']

Computing dF for nodes HB,WD

Elapsed Time: 0.00 sec

Keyplayer metric(s) DF:

Starting value for dF is 0.64755. Removing nodes ['HB', 'WD'] gives a
dF value of 0.81506

Producing report in txt format.

Generating plots in pdf format.

pyntacle Keyplayer completed successfully. Ending
```

The resulting fragmentation can be better assessed comparing the *dF* of the original network (before removal) with that calculated after the removal of the set. For this reason, the `kp-info` module returns also the *dF* value of the original network.

Results of the `kp-info` module can be saved in several file formats (default is the tab-separated value file format), along with a graphical network representation, when the network is small enough to be clearly represented in a picture (generally in the order of hundreds of nodes). These plots will be stored in a sub-directory, “pyntacle-plots”, of the current working directory.

Note: you can redirect both the report and the plots to a custom directory, using the `--directory/-d` argument.

The representation of the AdvSeek network follows where the removed nodes were represented in purple.

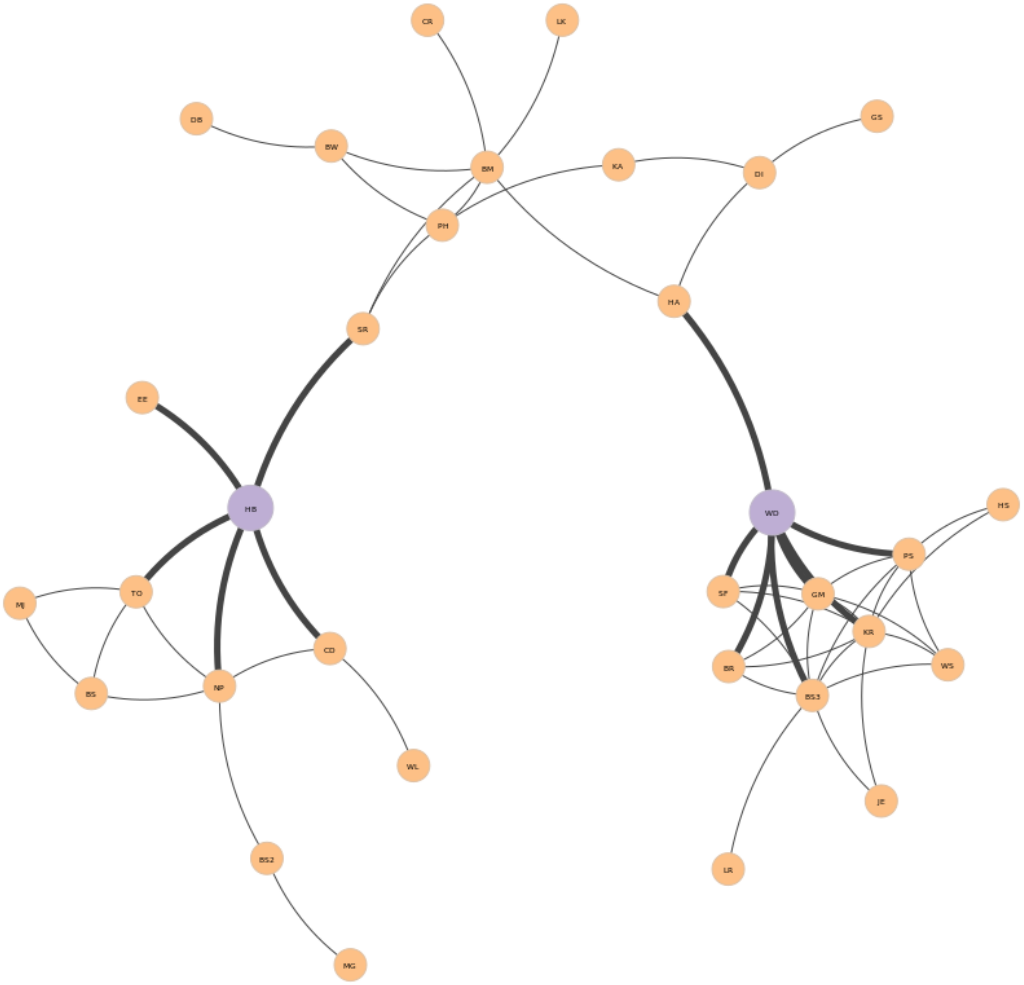

Figure 32: the AdvSeek Network reported by Pyntacle keyplayer kp-info command. Nodes in purple shows the input set used to compute their *dF* index. Thicker edges around the *kp-set* highlight the {HB, WD} neighborhood.

In case one wants to find the set of nodes of a particular size that maximally fragments the network or reaches the highest number of other nodes, a greedy optimization algorithm was implemented. It may not obtain the best unordered set of nodes of size k for the selected metrics, since this task would require:

$$\frac{N!}{(N-k)! * k!}$$

operations, where *N* is the size of the graph. Starting from a random set of nodes and then swapping nodes with others outside the set until the key-player metrics cannot be improved, one dramatically reduces the number of operations at the cost of suboptimal solutions. This algorithm is particularly useful when dealing with large networks, in the order of thousands or tenth of thousands of nodes, like a whole mammal PPI network.

The key-player metric chosen in this tutorial is the *m-reach*, which is a measure of *reachability*. It aims at counting the number of nodes reached by a key-player set of size *k* in *m* steps or less. In Borgatti's paper, the m-reach metrics is calculated on the AdvSeek network, with the number of steps set to 1, as shown in Table 9.

kp-set size	**Nodes reached**	**% of network reached**	**kp-set**
2	17	53	{BM, BS3}
3	23	72	{BM, BS3, NP}

Table 9: The best key player (kp) set of different sizes for the m-reach metric using a maximum distance (*m*) of 1, along with the number of nodes reached and the percentage of the network covered. Note: The node BS is here called BS3 as there are 3 synonymous nodes in the original graph)

To reproduce this result, type:

```
pyntacle keyplayer kp-finder -i Figure_8.adjm -k 2 -m 1 -t mreach --seed 100
```

The `kp-finder` enables the use of the greedy optimization search algorithm by default. This behavior can be changed using the `-I/--implementation` argument and setting the `brute-force` option (as you will read in the next paragraph). The `--seed` argument ensures results reproducibility, as the random initial set selection and node swapping will always be the same.

Pyntacle will output:

```
Reading input file...

Adjacency Matrix from Figure_8.txt imported

Using Greedy Optimization Algorithm for searching optimal KP-Set

Finding best set of kp-nodes of size 2 using an MREACH measure of 1 (kp pos measure)

An optimal kp-set of size 2 is (BS3, BM) with score 15

Elapsed Time: 0.02 sec

Search for the best kp set completed!
```

```
### RUN SUMMARY ###

kp set size: 2

With the given distance of 1, 15 nodes are reached by the kp-set (BS3,
BM).

The total percentage of nodes, which includes the kp-set, is 53.12%

### END OF SUMMARY ###

Producing report in txt format.

Generating plots in pdf format.

2018-08-06 10:54:41,569 - WARNING - A directory named "pyntacle-plots"
already exists, I may overwrite something in > there

pyntacle Keyplayer completed successfully. Ending
```

Note: We report the number of only the nodes reached by the kp-set (m-reach) and the percentage of reached nodes, which includes the kp-set (as from Borgatti's paper).

Results are stored in a text file in the current working directory, together with a visual plot that will highlight the nodes being part of the resulting kp-set. Thickness of edges will decrease as the distance from the kp-set (*m*) will increase.

Similarly, the optimal set of size 3 can be sought typing:

```
pyntacle keyplayer kp-finder -i Figure_8.adjm -k 3 -m 1 -t mreach --seed
1
```

This will produce the following output:

```
Reading input file...

Adjacency Matrix from Figure_8.txt imported

Using Greedy Optimization Algorithm for searching optimal KP-Set

Finding best set of kp-nodes of size 3 using an MREACH measure of 1 (kp
pos measure)

An optimal kpp-set of size 3 is (KR, BM, NP) with score 20

Elapsed Time: 0.05 sec

Search for the best kp set completed!


### RUN SUMMARY ###

kp set size: 3

With the given distance of 1, 20 nodes are reached by the kp-set (KR,
BM, NP).

The total percentage of nodes, which includes the kp-set, is 71.88%

### END OF SUMMARY ###


Producing report in txt format.

Generating plots in pdf format.

2018-08-06 11:00:19,952 - WARNING - A directory named "pyntacle-plots"
already exists, I may overwrite something in there
```

```
pyntacle Keyplayer completed successfully. Ending
```

The resulting kp-set ({KR, BM, NP}) is not the same reported by Borgatti ({BM, BS3, NP}), despite their scores being identical. This means that this network holds more kp-sets of size 3 with equal fragmentation scores.

A way of getting all these sets would be to run the greedy optimization search algorithm several times, setting different seeds. But this will not guarantee to capture all existing kp-sets. Another, exact, way would be to switch to the Brute-force search algorithm, as we will discuss in the next section.

KP-FINDER - BRUTE-FORCE SEARCH

Contrary to the greedy optimization search algorithm, the brute-force search algorithm seeks and finds the best solutions at the price of high demand of computing resources and running times. However, it was implemented to calculate the desired metrics for all combinations of size *k* of nodes in parallel on multiple CPUs, if available. The brute-force algorithm can be enabled by setting the `-I/--implementation` parameter with brute-force. By default, Pyntacle will use all available computing cores minus one (e.g. 7 cores out of 8 in an octacore processor). However, this can be tuned by the `-T/--threads` parameter.

Let's consider again the AdvSeek network and the case discussed in the previous section. The greedy optimization search did not replicate Borgatti's findings on the

AdvSeek network. Searching again the best kp-sets of size 3 with the brute-force search algorithm:

```
pyntacle keyplayer kp-finder -i figure_8.adjm -k 3 -m 1 -t mreach -I
brute-force
```

Note: The brute-force algorithm does not need to specify a seed, because it will always converge to the best solutions.

The command will result in:

```
Reading input file...

Adjacency                          Matrix                          from
/home/local/MENDEL/d.capocefalo/Desktop/benchmarks/test_networks/Real_
Borgatti_figure_8.adjm imported

Using Brute Force for searching optimal KP-Set

Finding best set of kp-nodes of size 3 using an MREACH measure of 1 (kp
pos measure)

The best kp-sets for metric mreach of size 3 are [('KR', 'BM', 'NP'),
('BS3', 'BM', 'NP')] with score 20

Elapsed Time: 0.97 sec

Search for the best kp set completed!



### RUN SUMMARY ###

kp set size: 3

With the given distance of 1, 20 nodes are reached by the kp-sets ((KR,
BM, NP), (BS3, BM, NP)).

The total percentage of nodes, which includes the kp-set, is 71.88%
```

```
### END OF SUMMARY ###


Producing report in txt format.

Generating plots in pdf format.
```

The two best solutions were finally found. This concludes the quick start guide of Pyntacle via command line. The same problems will be tackled using Pyntacle as a Python library.

4. Pyntacle library startup guide

The library is designed for intermediate-to-expert Python users with a basic knowledge of object-oriented programming and some experience with the igraph package (not necessarily for python, as igraph is available also for the C and R languages). If you are not familiar with igraph, we recommend reading its python tutorial, available at http://igraph.org/python/doc/tutorial/tutorial.html.

Pyntacle is built around igraph and perform its calculations on instances of `igraph.Graph` objects. Pyntacle provides several utilities for importing/exporting from/to `igraph.Graph` objects to/from several textual network file formats. We refer in this context to the file formats description depicted in Materials and Methods, section 2.8 for more details on regard. Moreover, we recommend reading the Appendix 2 on minimum network requirements to see whether your network can be parsed and used by Pyntacle. Finally, a complete description of each class and method is available from our API Documentation page.

IMPORT A NETWORK USING PYNTACLE

Networks can be imported from file via the PyntacleImporter class of the io_stream module. This class contains a series of handy methods that parse and store an input graph into an igraph.Graph object and initialize all the Pyntacle reserved attributes (described in Appendix 2).

Considering again the AdvSeek network, which is available as an adjacency matrix from file “figure_8.adjm”, it is imported with the following command:

```
>>> from pyntacle.io_stream.importer import PyntacleImporter

>>> adv = PyntacleImporter.AdjacencyMatrix("figure_8.adjm")

Adjacency matrix from figure_8.adjm imported
```

It is an `igraph.Graph` object, that can exploits all the built-in igraph functions:

```
>>> type(adv)

igraph.Graph
```

The `adv` object can be also inspected thoroughly to see its composition using igraph summarization functions to see the Advseek nodes, edges and attributes:

```
>>> adv.summary()

"IGRAPH UN-- 32 55 -- ['figure_8']\n+ attr: __implementation (g),
__sif_interaction_name (g), name (g), __parent (v), name (v),
__sif_interaction (e), adjacent_nodes (e)"
```

OCTOPUS: A CONVENIENT PYNTACLE WRAPPER

The classes and methods used to perform all the operations described in the command line guide are not encompassed into a single module, but they are rather divided in appropriate sub-methods, that can be recalled. A handy wrapper of all these methods is

the `Octopus` class. It is contained in the `tools` module. The list of all the `Octopus` methods can be inspected:

```
>>> from pyntacle.tools.octopus import Octopus

>>> dir(Octopus)

['__class__','__delattr__','__dict__','__dir__','__doc__','__eq__','__
format__','__ge__','__getattribute__','__gt__','__hash__','__init__','
__init_subclass__','__le__','__lt__','__module__','__ne__','__new__','
__reduce__','__reduce_ex__','__repr__','__setattr__','__sizeof__','__s
tr__','__subclasshook__','__weakref__','add_BF_F','add_BF_dF','add_BF_
dR','add_BF_mreach','add_F','add_GO_F','add_GO_dF','add_GO_dR','add_GO
_mreach','add_average_closeness','add_average_clustering_coefficient',
'add_average_degree','add_average_eccentricity','add_average_radiality
','add_average_radiality_reach','add_average_shortest_path_length','ad
d_betweenness','add_closeness','add_clustering_coefficient','add_compa
ctness','add_compactness_correct','add_completeness','add_completeness
_naive','add_components','add_dF','add_degree','add_density','add_diam
eter','add_eccentricity','add_eigenvector_centrality','add_kp_F','add_
kp_dF','add_kp_dR','add_kp_mreach','add_median_shortest_path_length','
add_pagerank','add_pi','add_radiality','add_radiality_reach','add_radi
us','add_shortest_path','add_shortest_path_igraph','add_weighted_clust
ering_coefficient']
```

When calling an Octopus function on an igraph object, `Octopus` will execute the corresponding Pyntacle function and will assign a new attribute to the graph with the result of the function as a value. For example, let's suppose one wants to compute the average degree of the AdvSeek network. Typing:

```
>>> Octopus.add_average_degree(adv)
```

will trigger the computation of the average degree, will create an `average_degree` attribute for the graph and will set the result (3.4375) to it. We can check it by recalling all the attributes of the `adv` object:

```
>>> adv.attributes()

['name', '__sif_interaction_name', '__implementation',
'average_degree']
```

And then inspecting the value stored in the `average_degree` attribute:

```
>>> adv["average_degree"]

3.4375
```

OCTOPUS - COMPUTE KEY-PLAYER METRICS FOR A GIVEN SET OF NODES

Let's say we want to reproduce Borgatti's results for network fragmentation on the AdvSeek network we already discussed in the previous command line tutorial. We can do this using Octopus like in the following example:

```
>>> Octopus.add_kp_dF(adv, nodes=["HB", "WD"])
Computing dF for nodes (HB, WD)

Elapsed Time: 0.00 sec
```

Where `nodes` is a list of names of the nodes belonging to the kp-set.

Octopus will add a new attribute, `dF_kpinfo`, to the graph `adv`. This attribute is a dictionary, where each item is a key:value pair made by a (sorted) tuple of nodes (the kp-

set) and the corresponding dF value. This is valid for each of the key player metrics we implemented.

```
>>> adv.attributes()

['name', '__sif_interaction_name', '__implementation',
'average_degree', 'dF_kpinfo']
```

and

```
>>> adv["dF_kpinfo"]

{('HB', 'WD'): 0.81716}
```

dF is a relative metric, in the sense that the effect of removing a set can be appreciated if compared with the fragmentation level of the original network. The initial dF value of a network we can be computed by using the `add_dF` method:

```
>>> Octopus.add_dF(adv)
```

The initial dF is stored in the corresponding `dF` attribute:

```
>>> adv["dF"]

0.64939
```

Now, we can conclude that removing HB and WD will result in an increase in fragmentation of (roughly) 17%.

The previous greedy optimization, which was performed by the command line kp-finder command, can be replicated with the add_GO_mreach method.

```
>>> Octopus.add_GO_mreach(adv,kp_size=2, m=1, seed=100)
An optimal kp-set of size 2 is (BS3, BM) with score 15
Elapsed Time: 0.02 sec
```

Like in the previous section, `Octopus` adds an attribute to the graph that stores a dictionary of node names (kp-set) and centrality measures. In this example, the attribute will be called `mreach_1_greedy`, since the centrality metrics is the m-reach with `m=1` argument and obtained with a run of the greedy optimization search algorithm

```
>>> adv.attributes()
['name', '__sif_interaction_name', '__implementation',
'average_degree', 'dF_kpinfo', 'dF', 'mreach_1_greedy']
```

The name is as much informative as possible. It shows that the m-reach metric with an *m* distance of 1 was searched with the greedy optimization criteria. This ensures that all the greedy optimization key player search for m-reach of distance 1 will be stored here.

As before, we can see the corresponding dictionary keys and their values associated to them:

```
>>> adv["mreach_1_greedy"]
{('BM', 'BS3'): 15}
```

Finally, the brute-force search performed before using Pyntacle Command line can be replicated with `Octopus` using the maximum number of available computing cores minus one.

```
>>> Octopus.add_BF_mreach(adv, kp_size=3, m=1)

The best kpp-sets for metric mreach of size 3 are [('KR', 'BM', 'NP'),
('BS3', 'BM', 'NP')] with score 20

Elapsed Time: 1.07 sec
```

Again, we can see that a new attribute storing the BruteForce search is stored into the `adv` object. This attribute is stored in the `mreach_1_bruteforce` attribute. This attribute will contain a tuple of 3 storing the node names as key and the corresponding m-reach result as value. This attribute does not overlap with the other key player searches we performed, to ensure a different layer of information for each search.

```
>>> adv["mreach_1_bruteforce"]

{(('BM', 'KR', 'NP'), ('BM', 'BS3', 'NP')): 20}
```

EXPORT THE IGRAPH.GRAPH OBJECT

Any igraph.Graph can then be saved to a text or binary file. Additionally, graphs stored in binary files retain all their attributes. The export utilities are implemented in the `PyntacleExporter` class of the `io_stream` module. Let's export the `adv` network into a binary format:

```
>>> from pyntacle.io_stream.exporter import PyntacleExporter
>>> PyntacleExporter.Binary(adv, "advseek.graph")

Graph successfully exported to Binary at path:
/home/d.capocefalo/Quick_Startup_Guide/advseek.graph
```

this will return a file named ‘advseek.graph’ in our current directory (we print the absolute path by default).

KEY PLAYER SEARCH WITHOUT OCTOPUS - BRUTE - FORCE SEARCH (CASE EXAMPLE)

The same operations performed with `Octopus` can also be performed by resorting to the Pyntacle APIs (algorithms and tools modules). These methods rely on an array of enumerators by which specifying:

the key-player metrics to be calculated;

the computing modes for some of the Pyntacle’s methods (i.e., serial, parallel CPU, parallel GPU).

These enumerators are implemented in the `tools` module and can be imported as:

```
#this enumerator stores all the reachability metrics
>>> from tools.enums import KpposEnum
#this one handles all the implementations
>>>from tools.enums import CmodeEnum
```

`KpposEnum` currently includes two reachability metrics: m-reach and *dR*:

```
>>> dir(KpposEnum)
```

```
['__class__', '__doc__', '__members__', '__module__', 'dR', 'mreach']
```

`CmodeEnum` contains four values: `auto`, `igraph`, `cpu` and `gpu`; `auto` is the default choice and commands Pyntacle to choose the best computing mode, according to the specific features of the graph is working on. The `igraph` value is chosen if one relies on the single-core implementations of igraph of some algorithms underlying the Pyntacle methods, while `cpu` is used when one relies only on Pyntacle functions, the computationally heavy ones being just-in-time compiled by Numba and run in parallel on multicore processors. Finally, `gpu` is used to defer computationally heavy functions to be executed on GPU-enabled NVIDIA graphics cards, if available. The value of this enumerator can be passed to the implementation parameter of any key-player methods.

```
>>> dir(CmodeEnum)

['__class__', '__doc__', '__members__', '__module__', 'auto', 'cpu',
'gpu', 'igraph']
```

For example, the brute-force search executed before with `Octopus` can be replicated using the `BruteForceSearch` method this way:

```
>>> from pyntacle.algorithms.bruteforce_search import BruteforceSearch  as bfs

>>> bfs.reachability(graph=adv, implementation=CmodeEnum.igraph,
kp_type=KpposEnum.mreach,m=1,kp_size=3)

The best kp-sets for metric mreach of size 3 are [('KR', 'BM', 'NP'),
('BS3', 'BM', 'NP')] with score 20

([('KR', 'BM', 'NP'), ('BS3', 'BM', 'NP')], 20)
```

Minimum Graph requirements

Currently, Pyntacle works with unweighted and undirected graphs, which meet the following criteria:

- A graph must contain at least two nodes and one edge;
- A unique identifier must be set for each node as a node `name` attribute. This attribute is added by default by the Pyntacle `import` methods;
- Two nodes must be linked by one edge only, as multigraphs are not supported;
- Any instance *g* of the `igraph.Graph` object must have a `name` attribute that must be set with a list of strings (e.g., `g["name"] = ["Graph1"]`). When importing a graph from file, the `name` attribute will be filled with the name of the file.
- The `name` attribute will be used by some Pyntacle utilities, like the `set` operations between networks, to keep track of the original graphs which this graph is resulting from

Pyntacle exchanges information with a graph through attributes. Some attributes are reserved but their values can be edited manually. Others (the ones in bold) can only be read. Table 10 lists all the reserved attributes and specifies the graph's elements (e.g., the graph itself, nodes or edges) which they can be applied to, the data types that they can hold and a general description of the attributes.

Attribute name	Attribute Level	Stored Data	Description
`name`	graph	list of strings	If obtained by a set operation, a graph can have multiple names, one for each originating graph.
`__sif_interaction_name`	graph	string	The name of the interaction, as specified in the header of the imported SIF file, **`None`** if the graph was not imported from a SIF file.
`__implementation`	graph	string	Allowed values: `cpu`, `gpu`, `igraph`. These are automatically set by Pyntacle according to topological properties and to the complexity of the graph. They drive Pyntacle to compute complex chunks of code in parallel on multi-core processors or on GPU, if available, through Numba, or on single core relying on the iGraph Python library.
`name`	node	string	Unique node name
`__parent`	node	list of strings	Useful when performing set operations between two graphs to keep track the source network of each node. Initialized to **`None`** by default.
`__module_number`	node	string	Used when searching for communities within a graph. It indicates the community which a node was assigned to. Communities are identified with integer numbers.
`__sif_interaction`	edge	list of strings	The value stored in the *interaction* column of a SIF file for a given link between two nodes.

			`None` if the graph was not imported from a SIF file.
`adjacent_nodes`	edge	tuple of strings	A tuple containing the attribute **name** of two adjacent nodes by this edge.
`weights`	edge	float or int	Weight assigned to an edge by algorithms that work with or make weighted graphs, such as the *pagerank* algorithm.

Table 10: Pyntacle reserved attribute for the `igraph.Graph` object, at each level. Attribute Names in bold are read-only and cannot be overwritten.

Publications

Mazzoccoli, G., Colangelo, T., Panza, A., Rubino, R., Tiberio, C., Palumbo, O., Carella, M., Trombetta, D., Gentile, A., Tavano, F., et al. (2016). Analysis of clock gene-miRNA correlation networks reveals candidate drivers in colorectal cancer. *Oncotarget 7*.

Mazza, T., Mazzoccoli, G., Fusilli, C., Capocefalo, D., Panza, A., Biagini, T., Castellana, S., Gentile, A., De Cata, A., Palumbo, O., et al. (2016). Multifaceted enrichment analysis of RNA-RNA crosstalk reveals cooperating micro-societies in human colorectal cancer. *Nucleic Acids Res.* 44.

Castellana, S., Fusilli, C., Mazzoccoli, G., Biagini, T., Capocefalo, D., Carella, M., Vescovi, A.L., and Mazza, T. (2017). High-confidence assessment of functional impact of human mitochondrial non-synonymous genome variations by APOGEE. *PLoS Comput. Biol.* 13.

Mazza, T., Copetti, M., Capocefalo, D., Fusilli, C., Biagini, T., Carella, M., De Bonis, A., Mastrodonato, N., Piepoli, A., Pazienza, V., et al. (2017). MicroRNA co-expression networks exhibit increased complexity in pancreatic ductal compared to Vater's papilla adenocarcinoma. *Oncotarget* 8.

Mazzoccoli, G., Castellana, S., Carella, M., Palumbo, O., Tiberio, C., Fusilli, C., Capocefalo, D., Biagini, T., Mazza, T., and Lo Muzio, L. (2017). A primary tumor gene expression signature identifies a crucial role played by tumor stroma myofibroblasts in lymph node involvement in oral squamous cell carcinoma. *Oncotarget* 8.

Pezzilli, S., Ludovico, O., Biagini, T., Mercuri, L., Alberico, F., Lauricella, E., Dallali, H., Capocefalo, D., Carella, M., Miccinilli, E., et al. (2017). Insights from molecular characterization of adult patients of families with multigenerational diabetes. *Diabetes 67.*

Castellana, S., Mazza, T., Capocefalo, D., Genov, N., Biagini, T., Fusilli, C., Scholkmann, F., Relógio, A., Hogenesch, J.B., and Mazzoccoli, G. (2018). Systematic Analysis of Mouse Genome Reveals Distinct Evolutionary and Functional Properties Among Circadian and Ultradian Genes. *Front. Physiol.* 9, 1178.

Capocefalo, D., Pereira, J., Mazza, T., Jordán, F. (2018) Food web topology and nested keystone species complexes. *Complexity*, 1979214, 8.

Capocefalo D., Truglio M., Biagini T., Castellana S., Mazzoccoli G., Carella M., Vescovi A.L., Jordán F., Mazza T., Computing group-centrality topological parameters of networks with Pytnacle *Bioinformatics,* submitted.

Caris-Maldonado. J.C., Capocefalo D. (as co-author), Lopez-Quilodran N., Molina-Fernandez C., Arias-Carrasco R., Sepúlveda-Hermosilla G., Slater A., Martinez P., van Zundert B., Vargas R., Mazza T., Maracaja-Coutinho V., Tevy, M.F. The dynamic aging transcriptome of Drosophila Melanogaster, manuscript in preparation.